SpringerBriefs in Applied Sciences and Technology
Nanoscience and Nanotechnology

Zhenglong Zhang

Plasmonic Photocatalysis
Principles and Applications

清華大學出版社
TSINGHUA UNIVERSITY PRESS

Springer

SpringerBriefs in Applied Sciences and Technology

Nanoscience and Nanotechnology

Series Editors

Hilmi Volkan Demir, Nanyang Technological University, Singapore, Singapore

Alexander O. Govorov, Clippinger Laboratories 251B, Department of Physics and Astronomy, Ohio University, Athens, OH, USA

Indexed by SCOPUS Nanoscience and nanotechnology offer means to assemble and study superstructures, composed of nanocomponents such as nanocrystals and biomolecules, exhibiting interesting unique properties. Also, nanoscience and nanotechnology enable ways to make and explore design-based artificial structures that do not exist in nature such as metamaterials and metasurfaces. Furthermore, nanoscience and nanotechnology allow us to make and understand tightly confined quasi-zero-dimensional to two-dimensional quantum structures such as nanopalettes and graphene with unique electronic structures. For example, today by using a biomolecular linker, one can assemble crystalline nanoparticles and nanowires into complex surfaces or composite structures with new electronic and optical properties. The unique properties of these superstructures result from the chemical composition and physical arrangement of such nanocomponents (e.g., semiconductor nanocrystals, metal nanoparticles, and biomolecules). Interactions between these elements (donor and acceptor) may further enhance such properties of the resulting hybrid superstructures. One of the important mechanisms is excitonics (enabled through energy transfer of exciton-exciton coupling) and another one is plasmonics (enabled by plasmon-exciton coupling). Also, in such nanoengineered structures, the light-material interactions at the nanoscale can be modified and enhanced, giving rise to nanophotonic effects.

These emerging topics of energy transfer, plasmonics, metastructuring and the like have now reached a level of wide-scale use and popularity that they are no longer the topics of a specialist, but now span the interests of all "end-users" of the new findings in these topics including those parties in biology, medicine, materials science and engineerings. Many technical books and reports have been published on individual topics in the specialized fields, and the existing literature have been typically written in a specialized manner for those in the field of interest (e.g., for only the physicists, only the chemists, etc.). However, currently there is no brief series available, which covers these topics in a way uniting all fields of interest including physics, chemistry, material science, biology, medicine, engineering, and the others.

The proposed new series in "Nanoscience and Nanotechnology" uniquely supports this cross-sectional platform spanning all of these fields. The proposed briefs series is intended to target a diverse readership and to serve as an important reference for both the specialized and general audience. This is not possible to achieve under the series of an engineering field (for example, electrical engineering) or under the series of a technical field (for example, physics and applied physics), which would have been very intimidating for biologists, medical doctors, materials scientists, etc.

The Briefs in NANOSCIENCE AND NANOTECHNOLOGY thus offers a great potential by itself, which will be interesting both for the specialists and the non-specialists.

Zhenglong Zhang

Plasmonic Photocatalysis

Principles and Applications

清華大學出版社
TSINGHUA UNIVERSITY PRESS

Springer

Zhenglong Zhang
Shaanxi Normal University
Xi'an, China

ISSN 2191-530X ISSN 2191-5318 (electronic)
SpringerBriefs in Applied Sciences and Technology
ISSN 2196-1670 ISSN 2196-1689 (electronic)
Nanoscience and Nanotechnology
ISBN 978-981-19-5187-9 ISBN 978-981-19-5188-6 (eBook)
https://doi.org/10.1007/978-981-19-5188-6

Jointly published with Tsinghua University Press
The print edition is not for sale in China (Mainland). Customers from China (Mainland) please order the print book from: Tsinghua University Press.

© Tsinghua University Press 2022
This work is subject to copyright. All rights are solely and exclusively licensed by the Publisher, whether the whole or part of the material is concerned, specifically the rights of reprinting, reuse of illustrations, recitation, broadcasting, reproduction on microfilms or in any other physical way, and transmission or information storage and retrieval, electronic adaptation, computer software, or by similar or dissimilar methodology now known or hereafter developed.
The use of general descriptive names, registered names, trademarks, service marks, etc. in this publication does not imply, even in the absence of a specific statement, that such names are exempt from the relevant protective laws and regulations and therefore free for general use.
The publishers, the authors, and the editors are safe to assume that the advice and information in this book are believed to be true and accurate at the date of publication. Neither the publishers nor the authors or the editors give a warranty, expressed or implied, with respect to the material contained herein or for any errors or omissions that may have been made. The publishers remain neutral with regard to jurisdictional claims in published maps and institutional affiliations.

This Springer imprint is published by the registered company Springer Nature Singapore Pte Ltd.
The registered company address is: 152 Beach Road, #21-01/04 Gateway East, Singapore 189721, Singapore

Acknowledgments

The author thanks heartily Ting Kong, Tingting Zhang, Zhengkun Fu and Hairong Zheng for their valuable contributions to this book. This work was supported by the Projects of Postgraduate Education Reform Foundation Shaanxi Province (YJSZG2020039), the Postgraduate Textbook Foundation (GERP2017) and the Excellent Books Publishing Foundation of Shaanxi Normal University.

Contents

1 Introduction 1
References 2

2 Electromagnetic Properties of Materials 5
2.1 Electromagnetic Properties of the Materials 6
2.2 Electromagnetic Wave Propagation 9
2.3 Dielectric Function of Drude Model 10
2.4 Dielectric Function of Drude-Lorentz Model 11
Reference 13

3 Fundamentals of Surface Plasmons 15
3.1 Surface-Plasmon Polaritons 15
3.1.1 Properties of Surface-Plasmon Polaritons 16
3.1.2 Excitation of Surface-Plasmon Polaritons 19
3.2 Localized Surface Plasmons 20
References 23

4 Surface-Plasmon Relaxation Effects 25
4.1 Energy Distribution of Free Electrons 25
4.1.1 Sommerfeld Free-Electron Model 25
4.1.2 The Momentum and Energy of Free Electrons in Metal Materials 27
4.1.3 The Statistical Distribution of Free Electrons in Metallic Materials 29
4.2 Plasmon-Induced Hot Electrons 30
4.3 Thermal Effect of Surface Plasmons 32
References 34

5 Principles of Plasmon-Driven Photocatalysis 35
5.1 Local Field-Effect-Driven Photocatalysis 35
5.2 Hot-Electron-Driven Photocatalysis 37
5.2.1 Indirect Electron Transfer 37
5.2.2 Direct Electron Transfer 39

5.3 Plasmon-Exciton Co-driven Photocatalysis 40
5.4 Thermal-Effect-Driven Photocatalysis 42
References 44

6 Measurement and Analysis of Plasmon-Driven Photocatalysis 47
6.1 Design of Surface-Plasmon Structures 47
6.2 Measurement by Chromatography and Electron Microscopy 50
6.3 Analytical Methods for Raman Spectra 53
6.4 Analytical Methods of Surface-Plasmon-Enhanced Spectra 57
References 59

7 Plasmon-Driven Catalysis of Molecular Reactions 63
7.1 Gas Dissociation Catalytic Reactions 63
7.2 Surface Molecular Catalytic Reactions 64
7.3 Single-Molecule Catalytic Reactions 66
References 69

8 Plasmon-Driven Photocatalysis of Water Decomposition and Phase Transition 71
8.1 Water Splitting 71
8.2 Seawater Desalination 74
8.3 Steam Sterilization 77
References 79

9 Plasmon-Driven Catalysis of Nanomaterials Growth 81
9.1 Growth of Metal Structures 81
9.2 Growth of Polymers 83
9.3 Growth of Crystals 85
References 89

Chapter 1
Introduction

In recent years, such fundamental issues as high-energy utilization, fossil-fuel consumption, and environmental pollution have become major challenges being faced globally [1, 2]. The production of sustainable fuels and chemicals using clean and renewable energy is therefore becoming increasingly urgent. Solar energy is considered to be an ideal option in the field of catalysis [3]. Semiconductor photocatalysts under the electrons interband excitation have received extensive attention in the fields of photothermal conversion and environmental governance [4–6]. However, due to the wide band gap and the faster charge carrier recombination of semiconductor materials with an ultraviolet band gap, a weakened ultraviolet-conversion efficiency is observed [7, 8]. Moreover, semiconductor photocatalysts have low-energy utilization and low quantum efficiency for visible-light and near-infrared photons, hindering the development and application of photocatalysts. Therefore, a promising catalyst is significant to break the limitations of semiconductors and realize large-scale applications employed in the catalytic field.

Since the early twentieth century, noble-metal nanostructures have emerged as promising photocatalysts in the field of plasmonic nano-optics, as they are capable of collecting solar energy and promoting efficient energy conversion [9]. Owing to the unique features of the localized surface-plasmon resonance (LSPR) of noble-metal nanostructures, an enhanced electromagnetic (EM) field is formed because its energy is effectively transformed into the collective vibrational energy of free electrons on the metal surface, simultaneously, hot carriers can be induced by the energy stored in the plasmonic field for the metal nanostructures [10]. The hot carriers eventually dissipate through phonon mode coupling, leading to a higher lattice temperature of the metal nanostructures. The field-effect enhancement, hot electrons, and thermal effects in plasmonic nanostructures have been successfully applied to enhance the catalysis of chemical reactions and material growth [11–13]. In particular, plasmonic nanostructures exhibit advantageous properties such as tunable size and shape, crystalline properties, and a unique composition; thus they offer enhanced reaction rates,

© Tsinghua University Press 2022

Z. Zhang, *Plasmonic Photocatalysis*, Nanoscience and Nanotechnology,
https://doi.org/10.1007/978-981-19-5188-6_1

higher selectivity, and milder reaction conditions [14]. At present, highly efficient water decomposition, hydrogen dissociation, molecular-photochemical synthesis, material growth, and many other issues are attracting widespread attention [14–17].

This book systematically outlines the principles and applications of plasmonic photocatalysis, including the basic EM properties of materials, surface-plasmon theory, and the principles behind the field-effect enhancements, hot electrons, and thermal effects in plasmon-driven photocatalytic activities. In addition, measurement methods, technological means, and the structural design and extended applications of nanocatalysts are all discussed in detail. We believe that this book will help researchers, doctoral candidates, and undergraduate students deepen their understanding of the principles of plasmon-driven photocatalysis and provide support for accelerating the development and application of plasmonic catalysis in numerous fields.

References

1. Lv ML, Xie YH, Wang YW, Sun XQ, Wu FF, Chen HM, Wang SW, Shen C, Chen ZF, Ni S, Liu G, Xu XX (2015) Bismuth and chromium co-doped strontium titanates and their photocatalytic properties under visible light irradiation. Phys Chem Chem Phys 17:26320–26329
2. Khan AA, Tahir M (2019) Recent advancements in engineering approach towards design of photo-reactors for selective photocatalytic CO_2 reduction to renewable fuels. J CO_2 Utilization 29:205–239
3. Umar A, Rao VG, Steven C, Suljo L (2018) Catalytic conversion of solar to chemical energy on plasmonic metal nanostructures. Nat Catal 1:656–665
4. Fujishima A, Honda K (1972) Electrochemical photolysis of water at a semiconductor electrode. Nature 238:37–38
5. Mills A, Hunte SL (1997) An overview of semiconductor photocatalysis. J Photochem Photobiol A Chem 108:1–35
6. Zheng Z, Xie W, Huang B, Dai Y (2018) Plasmon-enhanced solar water splitting on metal-semiconductor photocatalysts. Chem A Eur J 24:18322–18333
7. Xu DF, Cheng B, Zhang JF, Wang WK, Yu JG, Ho WK (2015) Photocatalytic activity of Ag_2Mo_4 (M = Cr, Mo, W) photocatalysts. J Mater Chem A 3:20153–20166
8. Kong T, Wei XM, Zhu GQ, Huang YH (2017) The photocatalytic mechanism of BiOI with oxygen vacancy and iodine self-doping. Chin J Phys 55:331–341
9. Zhou L, Tan Y, Wang J, Xu W, Yuan Y, Cai W, Zhu S, Zhu J (2016) 3D self-assembly of aluminium nanoparticles for plasmon-enhanced solar desalination. Nat Photonics 10:393–398
10. Brongersma ML, Halas NJ, Nordlander P (2015) Plasmon-induced hot carrier science and technology. Nat Nanotechnol 10:25–34
11. Yu Y, Sundaresan V, Willets KA (2018) Hot carriers versus thermal effects: resolving the enhancement mechanisms for plasmon-mediated photoelectrochemical reactions. J Phys Chem C 122:5040–5048
12. Golubev AA, Khlebtsov BN, Rodriguez RD, Chen Y, Zahn DRT (2018) Plasmonic heating plays a dominant role in the plasmon-induced photocatalytic reduction of 4-nitrobenzenethiol. J Phys Chem C 122:5657–5663
13. Mascaretti L, Naldoni A (2020) Hot electron and thermal effects in plasmonic photocatalysis. J Appl Phys 128:041101
14. Kong T, Zhang C, Gan X, Xiao F, Li J, Fu Z, Zhang Z, Zheng H (2020) Fast transformation of a rare-earth doped luminescent sub-microcrystal via plasmonic nanoislands. J Mater Chem C 8:4338–4342

15. Zhang C, Lu J, Jin N, Dong L, Fu Z, Zhang Z, Zheng H (2019) Plasmon-driven rapid in situ formation of luminescence single crystal nanoparticle. Small 15:e1901286
16. Fang Y, Li Y, Xu H, Sun M (2010) Ascertaining p, p′-dimercaptoazobenzene produced from p-aminothiophenol by selective catalytic coupling reaction on silver nanoparticles. Langmuir 26:7737–7746
17. Watanabe K, Menzel D, Nilius N, Freund HJ (2006) Photochemistry on metal nanoparticles. Chem Rev 106:4301–4320

Chapter 2
Electromagnetic Properties of Materials

Metallic materials well afford different optical properties under different frequencies of light. In general, for example, in the low-frequency regime of the spectrum, metals exhibit good conductive characteristics with few EM waves penetrating into them. In the visible range of the spectrum, metals are highly refractive and EM waves can hardly propagate through them. In the UV regime, alkali metals, such as sodium, show dielectric characteristics that allow EM waves to propagate through. However, noble-metal nanomaterials (e.g., Au and Ag) exhibit strong absorption abilities in the UV regime due to the interband transitions. Thus, the dielectric constants of metals can easily be seen to be frequency-dependent, which can be described through the dielectric function.

Furthermore, when the size of a metal structure is reduced to nanometers, its optical properties can still be described via classical Maxwell equations. In Sect. 2.1, we start with the classical Maxwell equation to obtain the dielectric functionality of metals. In Sect. 2.2, we discuss the dispersion relation of EM waves in metallic materials. Then, we use the Drude (free-electron) model to derive the dielectric functionality under different frequency regimes in Sect. 2.3. Finally, in Sect. 2.4, we compare the complex dielectric constants derived from the Drude model with the experimental data and accordingly modify this model. We hope this chapter will provide the reader with a fundamental understanding of the optical properties of plasmonic metallic materials.

© Tsinghua University Press 2022

Z. Zhang, *Plasmonic Photocatalysis*, Nanoscience and Nanotechnology,
https://doi.org/10.1007/978-981-19-5188-6_2

2.1 Electromagnetic Properties of the Materials

Maxwell equations in abridged differential form can be presented as follows:

$$\nabla \cdot \boldsymbol{D} = \rho_{\text{ext}}, \tag{2.1}$$

$$\nabla \cdot \boldsymbol{B} = 0, \tag{2.2}$$

$$\nabla \times \boldsymbol{E} = -\frac{\partial \boldsymbol{B}}{\partial t}, \tag{2.3}$$

$$\nabla \times \boldsymbol{H} = \boldsymbol{J}_{\text{ext}} + \frac{\partial \boldsymbol{D}}{\partial t}, \tag{2.4}$$

where $\boldsymbol{D}$ is the dielectric displacement, $\boldsymbol{B}$ is the magnetic induction, $\boldsymbol{E}$ is the electric field, and $\boldsymbol{H}$ is the magnetic field. These four macroscopic fields can be linked via

$$\boldsymbol{D} = \varepsilon_0 \boldsymbol{E} + \boldsymbol{P}, \tag{2.5}$$

$$\boldsymbol{H} = \frac{1}{u_0}\boldsymbol{B} - \boldsymbol{M}, \tag{2.6}$$

where $\boldsymbol{P}$ is the dipole moment inside the material, and $\boldsymbol{M}$ is the intensity of magnetization.

Here, we divide the electric-charge density and displacement current into external and internal parts resulting from distinctions between the external-driving system and the metals' internal-response system. The total electric-charge density and displacement current can be written as

$$\rho_{\text{total}} = \rho_{\text{ext}} + \rho_{\text{int}} \tag{2.7}$$

$$\boldsymbol{J}_{\text{total}} = \boldsymbol{J}_{\text{ext}} + \boldsymbol{J}_{\text{int}} \tag{2.8}$$

The relation of the internal charge density ρ_{int} with the dipole moment per unit inside the metal $\boldsymbol{P}$ and internal displacement current $\boldsymbol{J}_{\text{int}}$ can be described as

$$\nabla \cdot \boldsymbol{P} = -\rho_{\text{int}}, \tag{2.9}$$

$$\nabla \cdot \boldsymbol{J}_{\text{int}} = -\frac{\partial \rho_{\text{int}}}{\partial t}. \tag{2.10}$$

By combining Eqs. (2.9) and (2.10), we find the relation between the dipole moment $\boldsymbol{P}$ and the internal displacement current $\boldsymbol{J}_{\text{int}}$

$$\boldsymbol{J}_{\text{int}} = \frac{\partial \boldsymbol{P}}{\partial t}. \tag{2.11}$$

Substituting Eq. (2.5) into Eq. (2.1), and combing it with Eq. (2.11), we obtain

$$\nabla \cdot \boldsymbol{E} = \frac{\rho_{\text{ext}} + \rho_{\text{int}}}{\varepsilon_0}. \tag{2.12}$$

Equation (2.12) indicates that the macroscopic electric field includes both the external and induced internal fields, which is the great advantage of this approach.

In this chapter, we will only discuss the EM response in linear, isotropic, and nonmagnetic media, meaning that the intensity of magnetization $\boldsymbol{M}$ is 0. Thus, we can rewrite Eqs. (2.5) and (2.6) in the simple linear relation forms:

$$\boldsymbol{D} = \varepsilon_0 \varepsilon \boldsymbol{E}, \tag{2.13}$$

$$\boldsymbol{B} = u_0 u \boldsymbol{H}. \tag{2.14}$$

Combining Eqs. (2.13) and (2.5), we can obtain the third linear relation between the dipole moment $\boldsymbol{P}$ and electric field $\boldsymbol{E}$:

$$\boldsymbol{P} = \varepsilon_0 \chi \boldsymbol{E}, \tag{2.15}$$

where χ is the polarizability of the metal and equals $\varepsilon - 1$. The last linear relation is between the internal displacement current $\boldsymbol{J}_{\text{int}}$ and the electric field $\boldsymbol{E}$, which could be described by Ohm's law

$$\boldsymbol{J} = \sigma \boldsymbol{E}, \tag{2.16}$$

where σ is the electric conductivity. These four linear relations represent the macroscopic EM properties of isotropic linear materials.

At the beginning of this chapter, we showed that the optical responses of a metal are frequency-dependent. Thus, considering nonlocality in time and space, we can adapt Eqs. (2.13) and (2.16) into

$$\boldsymbol{D}(\boldsymbol{r}, t) = \varepsilon_0 \int \mathrm{d}t' \mathrm{d}r' \varepsilon\left(\boldsymbol{r} - \boldsymbol{r'}, t - t'\right) \boldsymbol{E}(\boldsymbol{r}, t) \tag{2.17}$$

$$\boldsymbol{J}(\boldsymbol{r}, t) = \varepsilon_0 \int \mathrm{d}t' \mathrm{d}r' \sigma\left(\boldsymbol{r} - \boldsymbol{r'}, t - t'\right) \boldsymbol{E}(\boldsymbol{r}, t) \tag{2.18}$$

Then, we use Fourier transformation to change the convolution into product form as follows:

$$\boldsymbol{D}(\boldsymbol{k},\omega) = \varepsilon_0 \varepsilon(\boldsymbol{k},\omega)\boldsymbol{E}(\boldsymbol{k},\omega), \tag{2.19}$$

$$\boldsymbol{J}(\boldsymbol{k},\omega) = \sigma(\boldsymbol{k},\omega)\boldsymbol{E}(\boldsymbol{k},\omega). \tag{2.20}$$

From Eqs. (2.19) and (2.20), we obtain the relation between the macroscopic fields and frequency-dependent constants. However, to illustrate the intrinsic optical properties of the material, we should remove the macroscopic field stimuli and determine the relation between the frequency and frequency-dependent constant, called the dielectric function.

To get this function, we first combine Eqs. (2.11) and (2.20), getting:

$$-i\omega\boldsymbol{P} = \sigma(\boldsymbol{k},\omega)\boldsymbol{E}(\boldsymbol{k},\omega), \tag{2.21}$$

Then, combining Eqs. (2.5) with (2.19), we obtain

$$\boldsymbol{P} = \varepsilon_0[\varepsilon(\boldsymbol{k},\omega) - 1]\boldsymbol{E}(\boldsymbol{k},\omega). \tag{2.22}$$

Finally, from Eqs. (2.21) and (2.22), we obtain the dielectric function of the form:

$$\varepsilon(\boldsymbol{k},\omega) = \frac{i\sigma(\boldsymbol{k},\omega)}{\omega\varepsilon_0} + 1. \tag{2.23}$$

Furthermore, we can obtain the complex refractive index $n(\omega)$ from the dielectric function shown in Eq. (2.23) as $n(\omega) = \sqrt{\varepsilon(\omega)}$. The complex dielectric constant and refractive index can be written as:

$$\varepsilon(\omega) = \varepsilon_1(\omega) + i\varepsilon_2(\omega), \tag{2.24}$$

$$n(\omega) = n_1(\omega) + i\kappa, \tag{2.25}$$

where κ represents the extinction coefficient determining the optical absorption ability of EM waves in a material. Once we square both sides of Eq. (2.25) and combine it with Eq. (2.24), we could easily obtain

$$\varepsilon_1 = n_1^2 + \kappa^2, \tag{2.26}$$

$$\varepsilon_2 = 2n_1\kappa, \tag{2.27}$$

$$n_1^2 = \frac{\varepsilon_1}{2} + \frac{1}{2}\sqrt{\varepsilon_1^2 + \varepsilon_2^2}, \tag{2.28}$$

$$\kappa = \frac{\varepsilon_2}{2n_1}. \tag{2.29}$$

The extinction coefficient κ is also linked with the absorption coefficient α through the following equation:

$$\alpha(\omega) = \frac{2\omega\kappa(\omega)}{c}. \tag{2.30}$$

The absorption coefficient is often used in Beer's law:

$$I(x) = I_0 \mathrm{e}^{-\alpha x}, \tag{2.31}$$

which describes the attenuation of the EM waves propagating through a medium.

2.2 Electromagnetic Wave Propagation

After determining the intrinsic properties of the metals, we can determine the EM wave transmission equation within the metals in free space ($\boldsymbol{J}_{\text{ext}} = 0$, $\rho_{\text{ext}} = 0$). Taking the curl on both sides of Eq. (2.3) and combining it with Eq. (2.4). Finally, we could get the wave equation of

$$\nabla \times \nabla \times \boldsymbol{E} = -u_0 \frac{\partial^2 D}{\partial t^2}. \tag{2.32}$$

Upon rewriting the electric field in the complex form $\boldsymbol{E} = \boldsymbol{E}_0 \mathrm{e}^{i\boldsymbol{k}\boldsymbol{r}-\omega t}$, we can change the left side of Eq. (2.32) to $\boldsymbol{k}(\boldsymbol{k}\cdot\boldsymbol{E}) - \boldsymbol{k}^2\boldsymbol{E}$. After realizing its right side in the Fourier domain $\frac{\partial}{\partial t} \rightarrow -\mathrm{i}\omega$, we obtain another form of the wave equation

$$\boldsymbol{k}(\boldsymbol{k}\cdot\boldsymbol{E}) - \boldsymbol{k}^2\boldsymbol{E} = -\frac{\omega^2\varepsilon(\boldsymbol{k},\omega)}{c^2}\boldsymbol{E}. \tag{2.33}$$

For transverse EM waves in the media, $\boldsymbol{k}\cdot\boldsymbol{E} = 0$. Thus, we can find the dispersion relation from Eq. (2.33):

$$\boldsymbol{k}^2 = \frac{\omega^2}{c^2}\varepsilon(\boldsymbol{k},\omega). \tag{2.34}$$

The longitudinal EM waves require $\boldsymbol{k}\ (\boldsymbol{k}\cdot\boldsymbol{E}) = \boldsymbol{k}^2\boldsymbol{E}$, meaning that the longitudinal collective oscillations occur only at $\varepsilon(\omega) = 0$. This situation corresponds to the volume plasmon excitation.

2.3 Dielectric Function of Drude Model

To elucidate the transport properties of electrons in metals, Paul Drude provided a free-electron gas model in 1900. It assumes that the motion of free electrons in solid materials (especially in metals) can be treated classically as a pinball model. The positive ions are regarded as a fixed and immobile array of nuclei existing in a "sea" of free electrons. Note that the lattice potential and electron–electron interactions are not considered in it. We can use following kinematic equation to describe the motion of the free electrons stimulated via the external electric field:

$$m\frac{\partial^2 \boldsymbol{r}(t)}{\partial t^2} + m\Gamma\frac{\partial \boldsymbol{r}(t)}{\partial t} = -e\boldsymbol{E}, \tag{2.35}$$

where $\Gamma = \frac{1}{\tau}$ represents the characteristic collision frequency, the reciprocal of the free-electron gas relaxation time τ. If we assume that the electric field is a harmonic time-dependent one, Eq. (2.35) could give

$$\boldsymbol{r}(t) = \frac{e}{\left(\omega^2 + \mathrm{i}\omega\Gamma\right)m}\boldsymbol{E}(t). \tag{2.36}$$

The relation between the free-electron displacement $\boldsymbol{r}(t)$ and macroscopic polarization $\boldsymbol{P}$ is

$$\boldsymbol{P} = -ne\boldsymbol{r}(t). \tag{2.37}$$

Then, substituting Eq. (2.36) into Eq. (2.37), we obtain

$$\boldsymbol{P}(t) = -\frac{ne^2}{\left(\omega^2 + \mathrm{i}\omega\Gamma\right)m}\boldsymbol{E}(t). \tag{2.38}$$

Combining Eq. (2.5) with Eq. (2.38) and comparing with (2.13), we obtain the dielectric function of the free-electron gas model:

$$\varepsilon(\omega) = 1 - \frac{\omega_\mathrm{P}^2}{\omega^2 + \mathrm{i}\Gamma\omega}, \tag{2.39}$$

where ω_p is the plasma frequency, which equals to $\frac{ne^2}{m\varepsilon_0}$. The plasma frequency is resulted from the restoring Coulomb interaction between positive and negative particles.

To better understand the intrinsic properties of the dielectric function. Equation (2.39) can be divided into real (ε_1) and imaginary (ε_2) parts:

$$\varepsilon_1(\omega) = 1 - \frac{\omega_\mathrm{P}^2\tau^2}{1 + \omega^2\tau^2}, \tag{2.40a}$$

$$\varepsilon_2(\omega) = \frac{\omega_p^2 \tau}{\omega\left(1 + \omega^2 \tau^2\right)}. \tag{2.40b}$$

From Eqs. (2.40a, 2.40b), it is obvious that the optical properties of the metal highly depend on the frequency of incident light. In the frequency region of $\omega < \omega_p$, metals exhibit their characteristic that barely allows any EM waves to propagate in them. For ω values close to or equal to ω_p ($\omega \approx \omega_p$) and $\omega \gg \frac{1}{\tau}$, the dielectric function can be simplified as

$$\varepsilon(\omega) = 1 - \frac{\omega_{textP}^2}{\omega^2}, \tag{2.41}$$

where $\varepsilon(\omega)$ is predominantly real, leading to the negligible damping of the EM energy. Note that this equation is only suitable for some regular metals like alkali ones. For noble metals like gold and silver in this frequency region, the dielectric constants are greatly influenced by interband transitions, leading to large imaginary parts of $\varepsilon(\omega)$. In the limit of $\omega \gg \omega_p$, $\varepsilon(\omega)$ is close to 1, equal to the dielectric constant in vacuum.

For a very low frequency ($\omega \ll \Gamma$), from Eqs. (2.40a, 2.40b), the imaginary part of the dielectric function $\varepsilon_2(\omega)$ is significantly higher than the real part $\varepsilon_1(\omega)$. Within this frequency regime, the complex refractive index is shown in Eqs. (2.28) and (2.29) can be approximated as:

$$n_1 \approx \kappa \approx \sqrt{\frac{\varepsilon_2}{2}} = \sqrt{\frac{\tau \omega_p^2}{2\omega}}, \tag{2.42}$$

where the magnitude of the real part of the refractive index is comparable to the extinction coefficient κ. Using the result from Eq. (2.42) to calculate the reflectivity R of the metal (normal incidence), we obtain

$$R = \frac{(n_1 - 1)^2 + \kappa^2}{(n_1 + 1)^2 + \kappa^2} \approx 1. \tag{2.43}$$

Equation (2.43) shows that a low incidence frequency will afford high reflectance by the metal.

2.4 Dielectric Function of Drude-Lorentz Model

In the previous section, we obtained the dielectric function of the free-electron model. As shown in Fig. 2.1a, b, we have calculated the real and imaginary parts of gold's relative permittivity through the dielectric function shown in Eqs. (2.40a) and (2.40b). The relative permittivity calculated for the Drude free-electron metal with

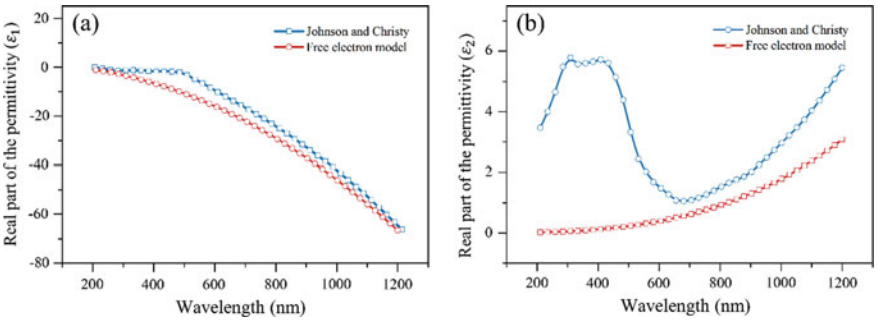

Fig. 2.1 Comparison of the relative permittivity of Au in the visible-light region, with blue lines representing data from the Drude free-electron model and red lines representing data from Johnson and Christy. **a** Relative permittivity of the real part; **b** relative permittivity of the imaginary part

$\hbar\omega_p = 8.5\,\text{eV}$ and $\tau = 14\,\text{fs}$ are compared with the experimental data from Johnson and Christy [1]. In the 200–600 nm region, the imaginary part of the free-electron model's relative permittivity is obviously lower than that observed experimentally. The mismatch results from the interband transitions of the noble metals, like silver and copper.

The interband electronic transition between the valance and conduction bands can be excited by photons with sufficient energy. As shown in Fig. 2.2, there are three kinds of band structures for the insulator, semiconductor, and metal. For the insulator (Fig. 2.2a), a large band gap is present between the valence and conduction bands, which barely allows electron transfer to the latter. For the semiconductor, as shown in Fig. 2.2b, the bandgap is significantly smaller than that for insulator. This bandgap can also be reduced via semiconductor doping, resulting in more electrons contributing to the interband transition. However, for metallic materials, the valence and conduction bands overlap, allowing electrons to move freely across the two. Thus, the interband transitions for metal materials can easily occur through excitation by photons of frequency lower than those needed for semiconductors, causing the noble metals to exhibit strong absorption.

The deficiency of Drude free-electron model is in that it neglects the effects that resulting from interband transitions. Drude-Lorentz model combines both contributions from bound and free electrons and introduces a Lorentz term for the interband transition. This overcomes the inadequacy of Drude model by replacing the kinematic equation shown in (2.35) with

$$m\frac{\partial^2 \boldsymbol{r}(t)}{\partial t^2} + m\Gamma\frac{\partial \boldsymbol{r}(t)}{\partial t} + m\omega_0^2 \boldsymbol{r}(t) = -e\boldsymbol{E}, \tag{2.44}$$

where $m\omega_0^2 \boldsymbol{r}(t)$ represents the contributions from bound electrons with resonance frequency ω_0. We can write the separate contributions as one equation in the form of Eq. (2.44), adding extra term $\frac{f_i\omega_i^2}{\omega_i^2-\omega^2-i\omega\Gamma_i}$ to the dielectric function. The modified

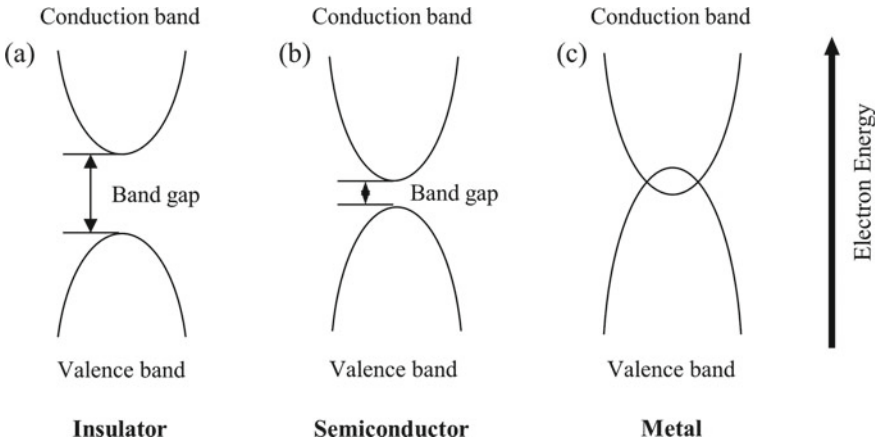

Fig. 2.2 Band structures of insulators, semiconductors, and metal

dielectric function can be given by

$$\varepsilon(\omega) = 1 - \frac{\omega_{\mathrm{P}}^2}{\omega^2 + \mathrm{i}\Gamma\omega} + \sum_{i=1}^{N} \frac{f_i \omega_i^2}{\omega_i^2 - \omega^2 - i\omega\Gamma_i}, \tag{2.45}$$

where N is the total of higher-energy oscillators, and f represents the weighting coefficient.

Note that the interband transition has a nonzero asymptotic value of the relative permittivity at a wavelength far from the resonance one. There, another constant needs to be added to offset this effect, thus, Eq. (2.45) is rewritten as:

$$\varepsilon(\omega) = \varepsilon_\infty - \frac{\omega_{textP}^2}{\omega^2 + \mathrm{i}\Gamma\omega} + \sum_{i=1}^{N} \frac{f_i \omega_i^2}{\omega_i^2 - \omega^2 - i\omega\Gamma_i}, \tag{2.46}$$

where the offset constant $\varepsilon_\infty = 1.2$ for gold.

Reference

1. Johnson PB, Christy RW (1972) Optical constants of the nobles metals. Phys Rev B 6:4370

Chapter 3
Fundamentals of Surface Plasmons

In the last chapter, we introduced the EM properties of materials and discussed the dielectric functions of Drude and Drude-Lorentz models. Under certain conditions, the regular electric-charge oscillation can be induced on the metal surface, driven by external EM fields. Two forms of oscillations are present: surface-plasmon polaritons (SPPs) and localized surface plasmons (LSPs). In this chapter, we will study the SPP excitation, propagation mechanism, and dispersion relation in Sect. 3.1 and the principles of LSP, and the optical properties of different nanostructures in Sect. 3.2.

3.1 Surface-Plasmon Polaritons

SPPs are EM wave-like phenomena that propagate along the interface between the dielectric and metal, which are generated by the coupling between photons and free electrons in the metal [1, 2]. SPP properties are defined by the dielectric constants of both the metal and dielectric as well as the frequency of the excitation light, meaning that SPP can be easily manipulated by varying the above conditions [3]. Moreover, the EM field of SPP is highly confined to the vicinity of the dielectric-metal interface, where energy follows an exponential-decay relation along the vertical direction of the interface [4–6]. Interestingly, this confinement leads to a strongly enhanced EM field and is widely used in electronics, chemical, and biological fields. In this section, we highly focus on the fundamental EM properties of the SPPs and the means of exciting them.

© Tsinghua University Press 2022

Z. Zhang, *Plasmonic Photocatalysis*, Nanoscience and Nanotechnology,
https://doi.org/10.1007/978-981-19-5188-6_3

3.1.1 Properties of Surface-Plasmon Polaritons

As mentioned above, SPPs are EM wave-like phenomena on the interface between the dielectric and metal; they can be described as

$$\text{Transverse electric (TE): } E(x, y, z) = Ae^{\pm k_z z} e^{ik_x x} \tag{3.1}$$

$$\text{Transverse magnetic (TM): } H(x, y, z) = Ae^{\pm k_z z} e^{ik_x x} \tag{3.2}$$

where k_z and k_x are the z- and x-components of the wave vector, respectively. Thus, we can use the Maxwell equations with the boundary conditions to obtain each solution in the metal and dielectric. As shown in Fig. 3.1, we suppose that the SPPs propagate on the interface including an isotropic dielectric with a real and positive dielectric constant ε_d. Furthermore, such constant of the metal is characterized by a frequency-dependent, isotropic complex constant of the form $\varepsilon_m(\omega) = \varepsilon'(\omega) + i\varepsilon''(\omega)$, where $\varepsilon'(\omega)$ and $\varepsilon''(\omega)$ represent its real and imaginary parts, respectively. According to the Maxwell equations, we can easily obtain

$$\nabla \times \boldsymbol{E} = i\mu_0 \omega \boldsymbol{H}, \tag{3.3}$$

$$\nabla \times \boldsymbol{H} = -i\varepsilon_0 \varepsilon \boldsymbol{E}. \tag{3.4}$$

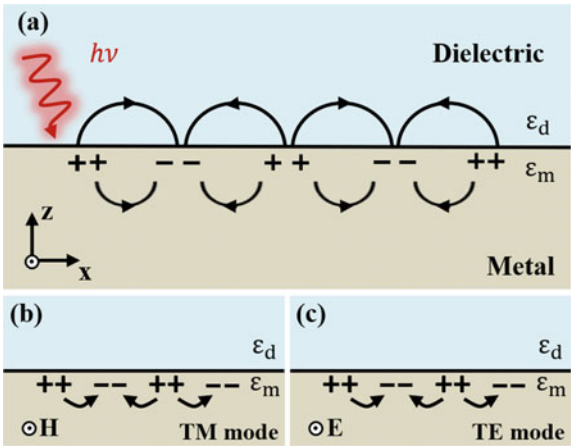

Fig. 3.1 SPP excitation and propagation modes. **a** Sketch of the SPP excitation and propagation mechanism on a smooth metallic surface; **b** sketch of the TM-mode surface wave propagating on the metal–dielectric interface; **c** sketch of the TE-mode surface wave propagating on the metal–dielectric interface

First of all, assume that the SPP is a TM wave propagating along the x direction of the interface. As shown in Fig. 3.1b, the magnetic vector of the TM wave is perpendicular to the xz-plane. Considering the component form of Eqs. (3.3) and (3.4), we obtain

$$\pm k_z E_x - \mathrm{i}\beta E_z = \mathrm{i}\omega\mu_0 H_y, \tag{3.5}$$

$$\pm k_z H_y = \mathrm{i}\omega\varepsilon_0\varepsilon E_x, \tag{3.6}$$

$$\mathrm{i}\beta H_y = -\mathrm{i}\omega\varepsilon_0\varepsilon E_z, \tag{3.7}$$

In the regions of $z > 0$ and $z < 0$, Eq. (3.6) can be described as follows:

$$-k_{z1} H_{y1} = \mathrm{i}\omega\varepsilon_0\varepsilon_1 E_{x1}, \tag{3.8}$$

and

$$k_{z2} H_{y2} = \mathrm{i}\omega\varepsilon_0\varepsilon_2 E_{x2}, \tag{3.9}$$

respectively. Applying the boundary conditions $H_{y1} = H_{y2}$ and $E_{x1} = E_{x2}$ to Eqs. (3.8) and (3.9), the relation of the wave vectors with the dielectric constant is afforded:

$$\frac{k_{z1}}{k_{z2}} = -\frac{\varepsilon_1}{\varepsilon_2}. \tag{3.10}$$

For this equation to exist, the wavevectors k_{z1} and k_{z2} must be real and positive, such that $\varepsilon_m(\omega)$ is negative. From this equation, we can easily see that SPPs are a kind of mixed, wave-like form of photons coupled with the collective oscillation of the free electrons on the metal surface.

Combining Eq. (3.10) and combining it with the wave equation, we can obtain the dispersion relation of SPPs:

$$\beta = k_0\sqrt{\frac{\varepsilon_1\varepsilon_2}{\varepsilon_1 + \varepsilon_2}} = \frac{\omega}{c}\sqrt{\frac{\varepsilon_m\varepsilon_d}{\varepsilon_m + \varepsilon_d}}, \tag{3.11}$$

As shown in Fig. 3.2, it is obvious that in the low-frequency range ($\varepsilon_m \to -\infty$) the wavevector of the SPPs can be approximately to

$$\beta = \frac{\omega}{c}\lim_{\varepsilon_m \to -\infty}\sqrt{\frac{\varepsilon_m\varepsilon_d}{\varepsilon_m + \varepsilon_d}} \approx \frac{\omega}{c}\sqrt{\varepsilon_d}, \tag{3.12}$$

which is very close to the wavevector of the light in the dielectric material.

When $\varepsilon_m \to \varepsilon_d$, ω approaches a certain value:

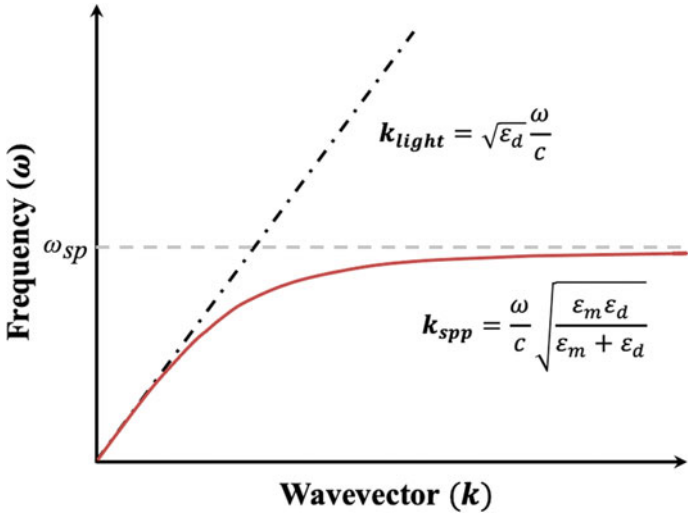

Fig. 3.2 Dispersion relation of the SPP and incident light

$$\omega_{\mathrm{sp}} = \frac{\omega_{\mathrm{p}}}{\sqrt{1+\varepsilon_d}}, \tag{3.13}$$

where ω_{textp} is the plasma frequency, the frequency of bulk plasmon electron oscillation. Consider that the TE wave propagates on the interface between the dielectric and metal. As with the solution of the very TM wave and from the Maxwell equations in Eqs. (3.3) and (3.4), we obtain

$$\pm k_z E_y = -\mathrm{i}\omega\mu_0 H_z, \tag{3.14}$$

$$\mathrm{i}\beta E_y = \mathrm{i}\omega\mu_0 H_z, \tag{3.15}$$

$$\pm k_z H_x - \mathrm{i}\beta H_z = -\mathrm{i}\omega\mu\varepsilon_0\varepsilon E_y. \tag{3.16}$$

In addition, from Eq. (3.6), we obtain:

$$-k_{z1} E_{y1} = \mathrm{i}\omega\mu_0 H_{x1} \quad (z > 0), \tag{3.17}$$

$$k_{z2} E_{y2} = \mathrm{i}\omega\mu_0 H_{x2} \quad (z < 0). \tag{3.18}$$

Combining Eqs. (3.17) and (3.18) with the boundary conditions $H_{x1} = H_{x2}$ and $E_{y1} = E_{y2}$, we obtain:

$$E_y(k_{z1} + k_{z2}) = 0. \tag{3.19}$$

If the SPPs can be seen as TE waves, the wavevectors of k_{z1} and k_{z2} must be positive in Eq. (3.19), meaning that E_{y1} and E_{y2} should be equal to 0. Thus, SPPs cannot exist as a TE wave and only the TM mode can be supported.

3.1.2 Excitation of Surface-Plasmon Polaritons

From the dispersion relation discussed in Sect. 3.1.1, the wavevector of SPPs is clearly mismatched with the light in free space under the same frequency, meaning that the light cannot directly excite SPPs by simply illuminating the smooth surface of a metal. Thus, if we want to excite SPPs using the light in free space, the wavevector of this light should be compensated using other approaches. One way to compensate for the wavevector differences between light and SPPs is using prisms to realize a total-internal-reflection (TIR) system.

Figure 3.3a presents the Kretschmann configuration, comprising a dielectric prism and a thin metal film. When the incident light passes through the prism with an incidence angle of θ (larger than the critical angle), the light will have a TIR with an x-component (evanescent wave) given by:

$$k_{x,n} = \sqrt{\varepsilon_{dn}}\frac{\omega}{c}\sin\theta. \tag{3.20}$$

Equation (3.20) shows that the wavevector of light increases in the prism because of the larger dielectric constant $\varepsilon_{d2} > 1$ (ε_{d1}), and the wavevector $k_{x,2}$ can be changed by choosing a different incident angle. As shown in Fig. 3.3b, when we choose an appropriate angle θ to set $k_{x,2}$ equivalent to k_{spp}, the evanescent wave can pass through the thin metal film with a tunneling effect and couple with the free electron in the metal film to achieve SPP excitation.

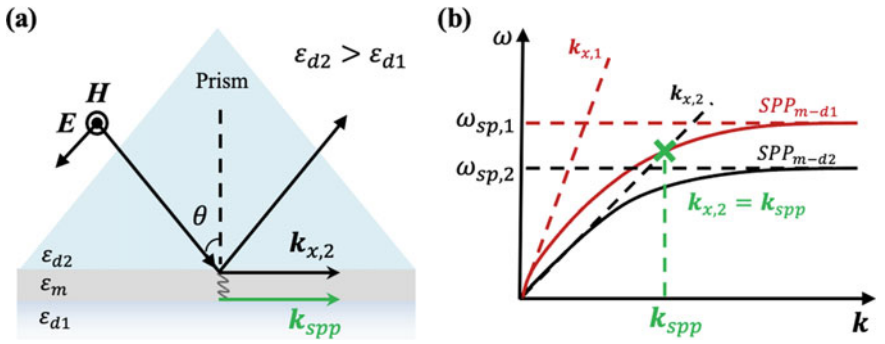

Fig. 3.3 Excitation configuration of SPP. **a** SPPs' excitation configuration of the Kretschmann system; **b** the dispersion relation of SPP and free-space light in the prism and dielectric materials

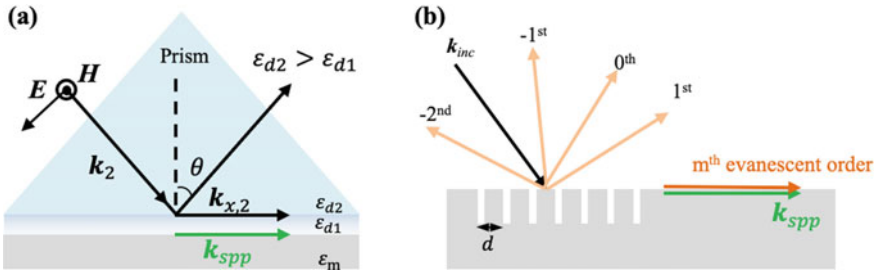

Fig. 3.4 Excitation configuration of SPP. **a** Otto excitation system; **b** periodic grating on the metal surface

However, the Kretschmann system can only be used for a very thin metal film due to tunneling limitations. For thick or bulk metal films, such system is obviously not suitable for SPP excitation. Here, in Fig. 3.4, we also show several other means of SPP excitation on the surface of a metal film with no thickness limitation. Figure 3.4a shows another prism's TIR system for SPP excitation (Otto configuration). As with the Kretschmann configuration, the Otto system uses the evanescent wave created by the prism for SPP excitation. Nevertheless, in the Otto system, a thin air space is introduced between the prism and metal film to prevent the limitation of the tunneling effect in the metal film.

Another means of inducing SPP excitation on a smooth metal surface is to use periodic grating to compensate the wavevector with a diffraction effect. Figure 3.4b shows the periodic grating with period d on the surface of a metal. When the light illuminates the grating, several different diffraction orders will occur. Due to the mismatch between the incident-light wavevector and SPP, the light of the regularly propagating diffraction orders cannot directly excite SPP. Rather, only the light from the evanescent diffraction orders can match the SPP with a wavevector of

$$k_{m,x} = k_{\mathrm{inc},x} + mK, \tag{3.21}$$

where m is the order of diffraction and K is a constant $\frac{2\pi}{d}$. Moreover, light can excite the SPPs on a metal surface with roughness or small particles which can also be treated as an abnormal grating.

3.2 Localized Surface Plasmons

When light is irradiated upon metallic particles whose size is close to or smaller than the wavelength of light, due to boundary confinement, the charge-density-wave will be confined to the particle's surface and form a localized EM field around it, called a localized surface plasmon (LSP). Unlike the SPP, the LSP's dispersion relations are discontinuous in resonant modes with different orders. The resonance of the

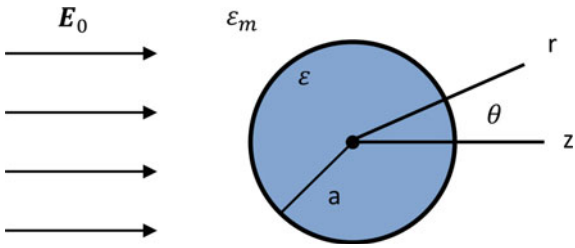

Fig. 3.5 Schematic of the metallic nanosphere in a uniform z-polarized plane wave

LSP will generate a significantly enhanced EM field, providing a strong foundation for many fields of surface-enhanced Raman scattering (SERS), surface-enhanced Raman fluorescence, optical-force enhancement, and manipulation, biosensing, and optical devices. In this section, we mainly discuss the LSP principle and the optical properties of different nanostructures.

A nanosphere can be seen as an electric dipole when its diameter is far below the wavelength of the incident light. Under this circumstance, we can use the quasi-static approximation to solve the resonant-frequency condition of the LSP.

As shown in Fig. 3.5, under quasi-static approximation conditions, the entire LSP system can be seen as a metallic sphere of radius a, and the frequency-dependent dielectric constant $\varepsilon_m(\omega)$ placed in a uniform z-polarized plane wave. The electric fields inside ($\boldsymbol{E_1}$) and outside ($\boldsymbol{E_2}$) of the nanosphere are satisfied with

$$\boldsymbol{E}_{1,2} = -\nabla\phi_{1,2}, \tag{3.22}$$

where the potential ϕ can be described with a Laplace equation

$$\nabla^2\phi_1 = 0 \quad (r < a), \tag{3.23}$$

or

$$\nabla^2\phi_2 = 0 \quad (r > a). \tag{3.24}$$

Combining Eq. (3.23) with the boundary conditions

$$\phi_1 = \phi_2 \quad (r = a), \tag{3.25}$$

$$\varepsilon_m \frac{\partial\phi_1}{\partial r} = \varepsilon_d \frac{\partial\phi_2}{\partial r} \quad (r = a), \tag{3.26}$$

$$\lim_{r\to\infty} \phi_2 = -E_0, \tag{3.27}$$

the potential solutions inside and outside of the nanospheres can be obtained:

$$\phi_1 = -E_0 r\cos\theta + \left(\frac{\varepsilon_m - \varepsilon_d}{\varepsilon_m + 2\varepsilon_d}\right) E_0 r\cos\theta = -\left(\frac{3\varepsilon_d}{\varepsilon_m + 2\varepsilon_d}\right) E_0 r\cos\theta, \quad (3.28)$$

$$\phi_2 = -E_0 r\cos\theta + a^3\left(\frac{\varepsilon_m - \varepsilon_d}{\varepsilon_m + 2\varepsilon_d}\right) E_0 \frac{\cos\theta}{r^2} = -E_0 r\cos\theta + \frac{\boldsymbol{P}\cdot\boldsymbol{r}}{4\pi\varepsilon_0\varepsilon_d r^3}, \quad (3.29)$$

where $\boldsymbol{p}$ is the dipole momentum, which can also be described with the polarizability α:

$$\boldsymbol{P} = \varepsilon_0\varepsilon_d\alpha\boldsymbol{E}_0. \quad (3.30)$$

Combining Eqs. (3.28) and (3.29), one can obtain the relation between the dielectric constant and polarizability:

$$\alpha = 4\pi a^3\left(\frac{\varepsilon_m - \varepsilon_d}{\varepsilon_m + 2\varepsilon_d}\right) \quad (3.31)$$

Thus, from Eq. (3.31), we can easily determine that the polarizability reaches a maximum value when $|\varepsilon(\omega) + 2\varepsilon_m|$ is minimal. This is called the resonant-enhancement condition:

$$|\varepsilon_m(\omega) + 2\varepsilon_d| = \text{ Minimum}, \quad (3.32)$$

also known as Fröhlich condition.

Moreover, we can solve the electric field inside and outside the nanosphere ($E = -\nabla\phi$):

$$\boldsymbol{E}_1 = \frac{3\varepsilon_d}{\varepsilon_m + 2\varepsilon_d}\boldsymbol{E}_0 \quad (3.33)$$

$$\boldsymbol{E}_2 = \boldsymbol{E}_0 + \frac{3n(\boldsymbol{n}\cdot\boldsymbol{p}) - \boldsymbol{p}}{4\pi\varepsilon_0\varepsilon_d}\frac{1}{r^3} \quad (3.34)$$

The above solution of the quasi-static approximation is only suitable for a nanosphere with a diameter less than 100 nm (visible and inferred excitation). For a particle with a larger size, the quasi-static approximation is no longer satisfied. However, Mie theory makes the connection between the size and shape parameters and the extinction spectrum:

$$E(\lambda) = \frac{24\pi^2 N a^3 \varepsilon_m^{\frac{3}{2}}}{\lambda\ln(10)}\left[\frac{\varepsilon_{\mathrm{i}}}{(\varepsilon_{\mathrm{r}} + \chi\varepsilon_m)^2 + \varepsilon_{\mathrm{i}}^2}\right] \quad (3.35)$$

where χ is the shape factor (2 for a sphere, and > 2 for a spheroid), α is the radius of the particle, ε_m is external dielectric constant, ε_{r} is the real metal-dielectric constant, and ε_{i} is the imaginary metal-dielectric constant.

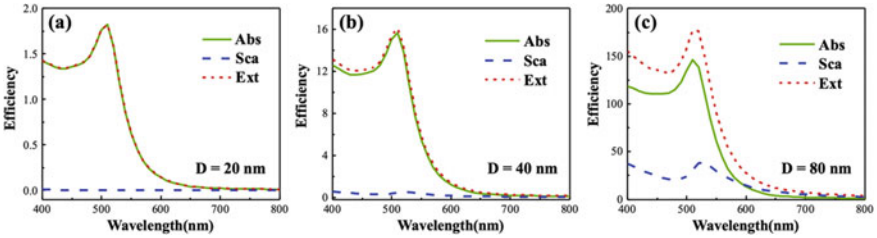

Fig. 3.6 The simulated spectral efficiencies of the absorption (green solid), scattering (blue dash), and extinction (red dot) spectra of Au nanospheres with diameters of **a** $D = 20$ nm, **b** $D = 40$ nm, and **c** $D = 80$ nm

The LSPR effect of the metallic structures strongly depends on the particle size, shape, and dielectric properties of the surrounding medium. Thus, the optical properties of Au nanospheres can be adjusted by changing their size and shape. Based on Mie theory, the efficiencies of the absorption, scattering, and extinction spectra for Au nanospheres of different sizes have been calculated and shown in Fig. 3.6. The figures show that the extinction peaks experience a red shift and the relative contribution of the scattering to extinction also increases with the size of Au nanospheres in the 20–80 nm range. Strong enhancement of absorption and scattering for metal nanoparticles (NPs) is attributed to the well-known collective oscillation of surface-plasmon electrons on the metal surface.

References

1. Kreibig U, Vollmer M (1995) Optical properties of metal clusters. Springer, Berlin
2. Novotny L, Hecht B, Keller O (2006) Principle of nano-optics. Phys Today 60:62
3. Pohl DW (2001) Near-field optics and the surface plasmon polariton. Springer, Berlin
4. Raether H (1988) Surface plasmons on smooth and rough surfaces and on gratings. Springer, Berlin
5. Enoch S, Bonod N (2012) Plasmonics—from basics to advanced topics. Springer, Berlin
6. Griffith DJ, Ruppeiner G (1981) Introduction to electrodynamics. Am J Phys 49:1188–1189

Chapter 4
Surface-Plasmon Relaxation Effects

In the previous chapter, we carefully introduced the EM properties of surface plasmons. Both SPPs and LSPs can be seen as collective electronic oscillation behavior. Thus, further discussing the electronic behavior in noble-metal materials is necessary. In Sect. 4.1, we introduce the Sommerfeld model to discuss the momentum and energy of free electrons in metals. Then, we discuss the statistical distribution of electrons in metals. Finally, we outline the mechanism behind hot-electron generation. In Sect. 4.3, we exhibit the thermal effects of the noble-metal materials coming with the collective electronic oscillations.

4.1 Energy Distribution of Free Electrons

4.1.1 Sommerfeld Free-Electron Model

In 1927, Arnold Sommerfeld further developed another free-electron model by introducing the quantum mechanical theory into Drude model. He proposed that the free electrons in metal materials move freely in a mean-potential field, which follows Fermi–Dirac statistics and the Pauli exclusion principle. The behavior of the free electrons in metals is largely influenced by the potential field generated from the nuclei and inner-shell electrons. Figure 4.1 shows the relation between the potential energy and the distance of the electrons from the isolated nucleus. For electrons with distances from the nucleus smaller than the orbital radius of the K atomic shell ($r < r_K$), the potential energy function $U(r)$ can be given as

$$U(r) = C\frac{Ze^2}{r}, \tag{4.1}$$

© Tsinghua University Press 2022

Z. Zhang, *Plasmonic Photocatalysis*, Nanoscience and Nanotechnology,
https://doi.org/10.1007/978-981-19-5188-6_4

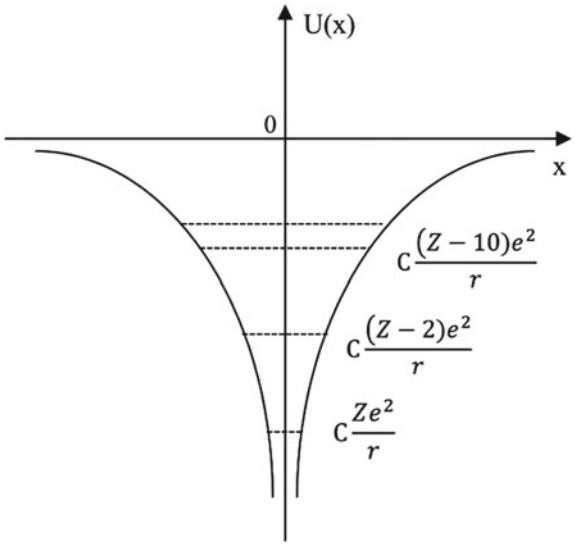

Fig. 4.1 The potential energy of the isolated atom

where Z represents the number of the electrons in the shell and C is a constant. For the electron for which the distance from the nucleus is between the orbital radii of the K and M atomic shells ($r_K < r < r_L$), the potential energy function $U(r)$ can be written as

$$U(r) = C\frac{(Z-2)e^2}{r}. \tag{4.2}$$

For the electron, whose distance from the nucleus is greater than the orbital radius of the M atomic shell ($r > r_L$), the potential energy function $U(r)$ is

$$U(r) = C\frac{(Z-10)e^2}{r}. \tag{4.3}$$

The potential energy diagram of the isolated atom, as shown in Fig. 4.1, clearly shows that the intensity of the potential field will gradually decrease as the distance from the nucleus increases. However, in metals, the nuclei are closely arranged with each other in an array. The outer shells of the metal atoms will overlap, allowing electrons to leave the original atom and move freely between similar orbitals. For valence electrons in a metal, the influence of the periodic potential field is small. Thus, the motion of the valence electrons in metal can be seen as free in an approximately uniform potential field generated by other free electrons and positive ions (comprising nuclei and inner-shell electrons).

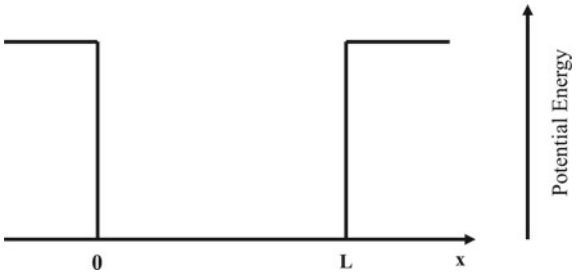

Fig. 4.2 1D square potential well of Sommerfeld model

Figure 4.2 shows the one-dimensional (1D) square potential well of Sommerfeld model. If we identify the bottom of the potential well as zero, the potential can be given by $U(x) = 0 (0 < x < L)$. No electrons are present in the external part of the metal; hence, the wave function is $\psi(x) = 0\,(x < 0, x > L)$.

4.1.2 The Momentum and Energy of Free Electrons in Metal Materials

According to the Sommerfeld model, we can directly write the Schrodinger equation of the electrons inside the metal as

$$\nabla^2\psi(x) + \frac{8\pi^2 m}{h^2}E\psi(x) = 0. \tag{4.4}$$

If we introduce the wavevector k into the equation, the energy level E can be written as $E = \frac{p^2}{2m} = \frac{h^2k^2}{2m}$, thus, Eq. (4.4) can be rewritten as

$$\nabla^2\psi(x) + 4\pi^2k^2\psi(x) = 0. \tag{4.5}$$

Solving Eq. (4.5), we obtain

$$\psi(x) = Ae^{i2\pi kx} + Be^{-i2\pi kx}. \tag{4.6}$$

When $x = 0$, $A + B = 0$ is afforded, and Eq. (4.6) can be written as

$$\psi(x) = A(e^{i2\pi kx} - e^{-i2\pi kx}). \tag{4.7}$$

Equation (4.7) clearly shows that the wave function of the electrons in metal is the same as that of the electrons in free space, which is a plane-wave solution.

Now, if we combine the periodic boundary condition with the boundary condition $(\psi(L) = 0\,(x = L))$, the wave equation becomes

$$\psi(x) = \psi(x + L) \tag{4.8}$$

To satisfy Eq. (4.8), $e^{i2\pi kx} = e^{-i2\pi kx} = 1$ is necessary, which implies that $kL = n$ ($n = 0, \pm1, \pm2, \pm3, \ldots$). The momentum and energy of the free electrons in metallic materials are given by

$$p = kh = \frac{h}{L}n, \tag{4.9}$$

$$E = \frac{p^2}{2m} = \frac{h^2k^2}{2m} = \frac{h^2n^2}{2mL^2}. \tag{4.10}$$

The momentum and energy of free electrons in metal materials are clearly discontinuous and quantized. For a three-dimensional (3D) wave function, the forms of the momentum and energy of the system are

$$p_{(x/y/z)} = \frac{h}{L}n_{(x/y/z)}, \tag{4.11}$$

$$E = \frac{p^2}{2m} = \frac{h^2}{2m}(k_x^2 + k_y^2 + k_z^2) = \frac{h^2}{2mL^2}(n_x^2 + n_y^2 + n_z^2). \tag{4.12}$$

According to the Pauli exclusion principle, on every lattice site of the momentum space, two electrons cannot occupy the same quantum state. Then the quantum number of the momentum space in 3D form can be expressed as

$$\mathrm{d}N_p = \frac{2L^3}{h^3}\mathrm{d}p_x\mathrm{d}p_y\mathrm{d}p_z, \tag{4.13}$$

where the $\frac{L^3}{h^3}$ represents the state density of the momentum space.

For the metal materials in 3D space, the energy level of the electrons is defined by the wavevector (k_x, k_y, k_z). Thus, we can treat the constant energy surface of the free electrons in metal materials as a sphere:

$$k_x^2 + k_y^2 + k_z^2 = \frac{2mE}{h^2}, \tag{4.14}$$

where E is a constant. The density of the energy state depends upon the number of quantum state $\mathrm{d}N$ in the energy region of $E \sim E + \mathrm{d}E$, which is defined as

$$\frac{\mathrm{d}N_E}{\mathrm{d}E} = \frac{8\pi mL^3}{h^3}\sqrt{2mE}, \tag{4.15}$$

where the number of the quantum state is $\mathrm{d}N_E = 2\frac{L^3}{h^3}\mathrm{d}V = \frac{8\pi mL^3}{h^3}\sqrt{2mE}\mathrm{d}E$.

4.1.3 The Statistical Distribution of Free Electrons in Metallic Materials

In the last section, we studied the energy state and momentum distribution of free electrons in metals. However, these states are not necessarily occupied by electrons; hence, in this section, we will further study the electron's occupational probabilities of the quantum state and the distribution regularities of free electrons.

From the above discussion, we know that the constant energy surface of the free electrons in metals is a sphere. When the system temperature is absolute zero ($T = 0$ K), the highest electron-filled energy surface is called the Fermi surface, able to separate the occupied electronic state from the unoccupied one at zero temperature, which is very important for metals, in that their kinetic properties depend on electrons near the Fermi surface.

The probability function for energy-state occupation by the electrons can be described through the Fermi–Dirac distribution:

$$f(E) = \frac{1}{e^{\frac{(E-E_F)}{KT}} + 1} \tag{4.16}$$

where $f(E)$ has been called Fermi factor, K is the Boltzmann constant, T is the temperature of the system and E_F represents the Fermi level.

Figure 4.3 shows the diagram of the Fermi distribution function. When $T = 0$ K and $E > E_F$, the Fermi factor $f(E) = 0$ K. The electron occupation probability of all energy levels that are higher than the Fermi level is zero. For $T = 0$ K and $E > E_F$, the Fermi factor $f(E) = 1$, meaning that energy levels smaller than the Fermi level are all occupied by the electrons. When the temperature T is no longer absolute zero, the energy levels above the Fermi level exhibit a high probability of being occupied by the electrons, with the probability varying exponentially with increasing temperature.

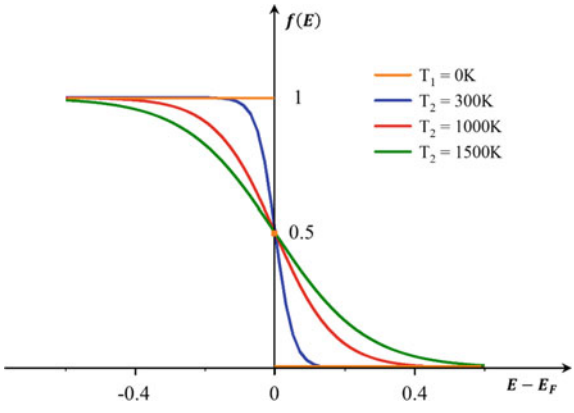

Fig. 4.3 Diagram of the Fermi–Dirac distribution

4.2 Plasmon-Induced Hot Electrons

In the previous section, we introduced the electron distributions in metal materials under different temperatures. When the electrons inside the metal at temperature T_1 ($T_1 > 0$ K) absorb extra energy from outside stimulations, some electrons will be pumped into higher-energy levels (excited states, as shown in Fig. 4.4), so-called "hot electrons."

Using light as an excitation source can generate hot electrons in both metals and semiconductors. Hot electrons can be divided into two categories: those capable of breaking the confinement of the metal surface and those confined within metals. Electrons that have absorbed photons with energies higher than the work function will escape from the material surface; however, electrons that have absorbed-photon energies lower than the work function will be pumped into the excited state (i.e., hot electrons). but still be confined to the metal.

The *d*- and *s*-band of noble metals, like Au and Ag (as shown in Fig. 4.5a), overlap with each other and the *d*-band is located below the Fermi level [1].

When the absorbed-photon energy equals the energy spacing between the ground and excited states of the electrons, the interband electronic transition can proceed. Thus, hot electrons in noble metals can be directly excited by high-frequency light. For non-noble metals, like Pt and Pd, both the *d*- and *s*-band are unfilled, meaning that the energy spacing between the ground and excited states is much smaller than that for the noble metals (Fig. 4.5b). Hence, interband transitions for non-noble metals can be directly excited by visible light.

Hot electrons in metals are generated not only by direct interband excitation of the metal surface using photons but also through intraband transitions caused by the nonradiative decay processes of surface plasmons. When noble micro/nanoparticles couple with incident light, strong LSPR will occur. The plasmon-dipole oscillation will appear as phase mismatch on a femtosecond timescale due to the damping effect,

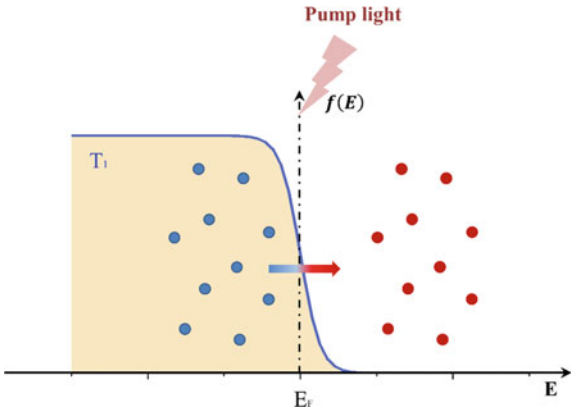

Fig. 4.4 Schematic of hot electrons excited via a pump light source

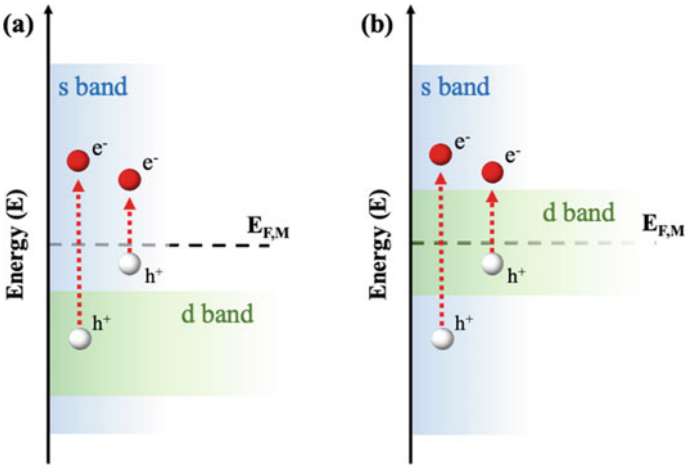

Fig. 4.5 Band structure of the **a** noble metal and **b** non-noble metal

also called the phase retardation effect. The coupled photons will decay through both radiative and nonradiative forms [2]. As shown in Fig. 4.6, the energy produced from the plasmon radiative decay process will be released via reemitted photons from the particle. For nonradiative decay processes, the energy obtained from incident photons will be transferred to the surface plasmon, and then retransfer to ground-state electrons through nonradiative decay, generating hot electrons.

In 2014, Manjavacas et al. developed a theoretical model to explain the plasmon-induced hot-carrier generation by using the Fermi's golden rule. The Hamiltonian used to describe hot-carrier transition is

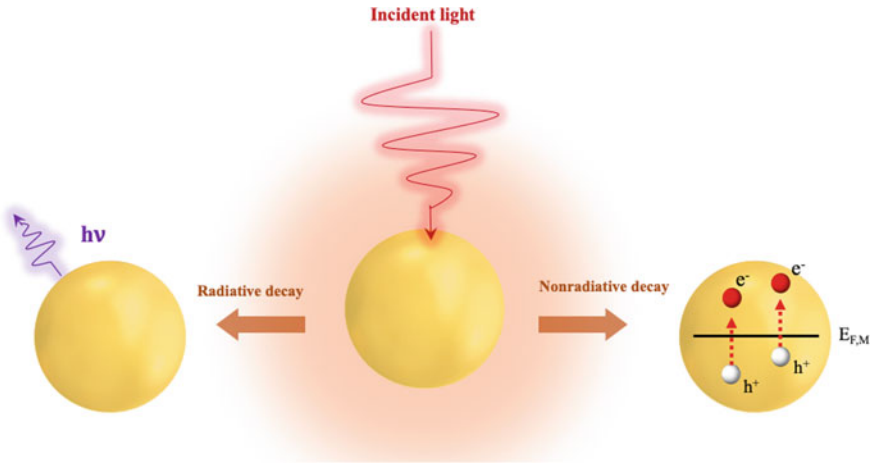

Fig. 4.6 Coupled photon decay process under LSP resonance

$$\mathcal{H} = \int \mathrm{d}\boldsymbol{r}[V(\boldsymbol{r},\omega) + V^*(\boldsymbol{r},\omega)] \sum_{\mathrm{i,f}} \rho_{\mathrm{fi}}(\boldsymbol{r}) b_{\mathrm{f}}^{+} b_{\mathrm{i}}, \tag{4.17}$$

$$\rho_{\mathrm{fi}}(\boldsymbol{r}) = e\Psi_{\mathrm{f}}^*(\boldsymbol{r})\Psi_{\mathrm{i}}(\boldsymbol{r}), \tag{4.18}$$

where Ψ_{i} and Ψ_{f} are the initial and final state located below and above the Fermi level, respectively; $V(\boldsymbol{r},\omega)$ is the total potential; e is the elementary charge, and $b_{\mathrm{i}}^{+}(b_{\mathrm{i}})$ is the operator that creates an electron (hole) in state Ψ_{i}. Then the probability of hot-electron excitation in state f per unit time is given by Fermi's golden rule

$$\Gamma_e(\varepsilon_{\mathrm{f}},\omega) = \frac{4}{\tau}\sum_i \mathcal{F}(\varepsilon_{\mathrm{i}})[1-\mathcal{F}(\varepsilon_{\mathrm{f}})] \cdot \left\{ \frac{|M_{\mathrm{fi}}(\omega)|^2}{(\hbar\omega - \varepsilon_{\mathrm{f}} + \varepsilon_{\mathrm{i}})^2 + \hbar^2\tau^{-2}} + \frac{\left|M_{\mathrm{if}}^*(\omega)\right|^2}{(\hbar\omega + \varepsilon_{\mathrm{f}} - \varepsilon_{\mathrm{i}})^2 + \hbar^2\tau^{-2}} \right\} \tag{4.19}$$

where $\mathcal{F}$ represents Fermi–Dirac distribution, and $M_{\mathrm{fi}} = \int \mathrm{d}\boldsymbol{r} V(\boldsymbol{r},\omega)\rho_{\mathrm{fi}}(\boldsymbol{r})$ represents the transition matrix element. The probability of a hot-hole excitation in state f per unit time is directly obtained by interchanging the subscripts i and f in Eq. (4.19) behind the summation symbol.

If the size of the plasmon particle is significantly smaller than the wavelength of the incident light ($D \ll \lambda$), the phase retardation effects can be neglected and the hot-electron generation system can be discussed under the quasi-static assumption. Now the NP can be seen as a finite square potential well with diameter D and depth V_0 [3, 4]. Qiu and his group calculated the potential of an AgNP excited via a linearly polarized plane wave. They presented the electric potential fields of the NP at frequencies of non-LSPR and LSPR, respectively, and the total potential field of the excitation system. The electric potential of the electron inside the metal nanosphere is still lower than that outside the sphere (i.e., the electron is still localized inside the small sphere, but the probability of escape is increased).

4.3 Thermal Effect of Surface Plasmons

Another important effect of the surface-plasmon relaxation process is heat generation. After hot electrons are generated, their energy is converted to heat through the rapid decay of the surface plasmons, resulting in significant heating of the nanostructures and their surroundings [5]. Schematic diagrams of the LSPR decay process under optical excitation are shown in Fig. 4.7. A photon is absorbed by exciting the LSPR of the metal nanostructure, for which the probability of photon absorption is proportional to the square of the local electric field inside the metal. Plasmon resonances in the metal nanostructure can be radiatively or nonradiatively damped at a timescale of 1–100 fs. The excited oscillations of electrons can be rapidly released through

electron–electron scattering at a time scale of 100 fs–1 ps, resulting in a thermal Fermi–Dirac distribution. After the electrons reach quasi-thermal equilibrium, the electron–electron scattering effect significantly weakens, and the electron–phonon scattering effect becomes obvious at a time scale of 1–10 ps. After a sufficient period (100 ps–10 ns) of internal-particle interaction, the metal NPs again reach a state of thermal equilibrium, leading to heat generation in the metal-nanostructure lattice. The heat dissipates into the surrounding medium, resulting in photothermal conversion of the plasmonic nanostructure.

The analysis of the relaxation processes of surface plasmons at different time scales shows that photothermal conversion mainly depends upon the local electric-field enhancement and light-absorption process of the plasmonic nanostructure (Fig. 4.8) [6]. The local heat intensity $Q(\mathbf{r}, t)$ is derived from the optical dissipation of the plasmonic components in the system [7]:

$$\begin{aligned} Q &= \langle \boldsymbol{j}(\boldsymbol{r}, t) \cdot \boldsymbol{E}(\boldsymbol{r}, t) \rangle_t \\ &= \frac{\omega}{8\pi} |\boldsymbol{E}_\omega(\boldsymbol{r})|^2 \cdot \mathrm{Im}\varepsilon(\boldsymbol{r}) \cdot \mathrm{pulse}(t), \end{aligned} \tag{4.20}$$

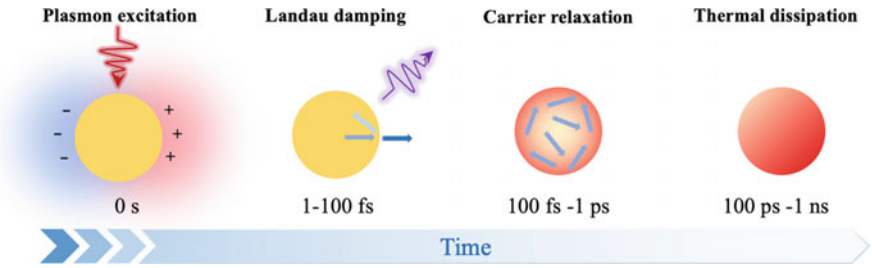

Fig. 4.7 Schematic diagrams of the LSPR decay processes under optical excitation

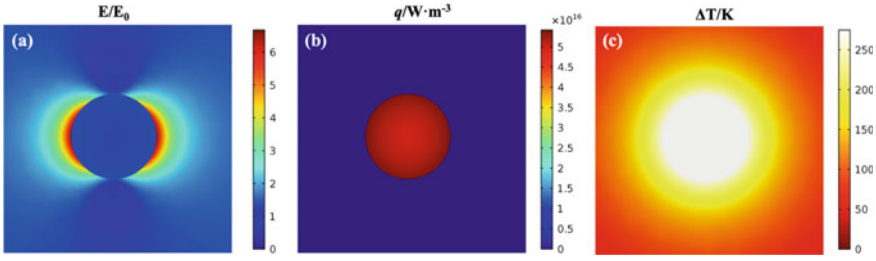

Fig. 4.8 Heat generation of surface plasmons. **a** A gold nanosphere with a diameter of 40 nm; **b** EM distribution of the gold nanosphere; **c** thermal density distribution of the gold nanosphere; **d** steady-state temperature-field distribution of the gold nanosphere

where $\boldsymbol{j}(\boldsymbol{r}, t)$ is the electric current density, $\boldsymbol{E}(\boldsymbol{r}, t)$ represents the electric field inside the system, and $\varepsilon(\boldsymbol{r})$ represents the local dielectric constant. The heat intensity was found to be proportional to the square of the electric-field intensity inside the plasmonic nanostructure [7]. When the scale of the plasmonic nanostructure is significantly smaller than the incident wavelength, the electric field inside the plasmonic structure is approximately uniform, leading to a relatively uniform heat-source density (Fig. 4.8c). Since the thermal conductivity of metals is generally much greater than that of the surrounding media, the thermal energy will diffuse into surrounding environment over a very short time; thus, it can approximately be assumed that the temperature in the metal micro-nano structure is uniform. Its temperature distribution can be given as [8]

$$\Delta T(r) = \frac{Q}{4\pi K_m r}, \tag{4.21}$$

where r is the distance from the center of the plasmonic nanostructure, and K_m is the thermal conductivity between the plasmonic nanostructure and the surrounding environment (assuming it is a homogeneous medium).

References

1. Aslam U, Rao VG, Chavez S, Linic S (2018) Catalytic conversion of solar to chemical energy on plasmonic metal nanostructures. Nat Catal 1:656–665
2. Clavero C (2014) Plasmon-induced hot-electron generation at nanoparticle/metal-oxide interfaces for photovoltaic and photocatalytic devices. Nat Photonics 8:95–103
3. Manjavacas A, Liu JG, Kulkarni V, Nordlander P (2014) Plasmon-induced hot carriers in metallic nanoparticles. ACS Nano 8:7630–7638
4. Pan MY, Li Q, Chou W (2016) Hot electrons in metallic micro/nano-structures. Physics 45:781–789
5. Brongersma ML, Halas NJ, Nordlander P (2015) Plasmon-induced hot carrier science and technology. Nat Nanotechnol 10:25–34
6. Bell AP, Fairfield JA, Mccarthy EK, Mills S, Boland JJ, Baffou G, Mccloskey D (2015) Quantitative study of the photothermal properties of metallic nanowire networks. ACS Nano 9:5551–5558
7. Kong XT, Khosravi Khorashad L, Wang Z, Govorov AO (2018) Photothermal circular dichroism induced by plasmon resonances in chiral metamaterial absorbers and bolometers. Nano Lett 18:2001–2008
8. Wang SJ, Su D, Zhang T (2019) Research progress of surface plasmons mediated photothermal effects. Acta Phys Sin 68(14):144401

Chapter 5
Principles of Plasmon-Driven Photocatalysis

In the last chapter, we clarified the principles of the surface-plasmon relaxation effects. Among them, field-effect enhancements, hot electrons, and thermal effects play critical roles in surface-plasmon-induced photocatalytic reactions. In this chapter, we highly focus on the mechanisms of field-effect enhancements, hot electrons, and thermal effects in plasmon-driven photocatalysis. Moreover, the principles of indirect and direct electron transfer, as well as plasmon-exciton co-driven for photocatalytic reaction, will be elucidated in detail. Related advanced reports will also be provided.

5.1 Local Field-Effect-Driven Photocatalysis

LSPR excitation directly leads to the limitation of the light energy and the redistribution of photons, increasing the photon density on the surface of the metal NPs due to the enhanced plasmonic field [1]. Similarly, reactant molecules can be excited to transfer energy through photons [2]. A local field with a higher photon density can significantly improve the rate of catalytic reactions. For plasmonic field-driven catalysis, resonance-energy transfer with energy overlap between the local field and the reactant band gap needs to be achieved [3]. This energy transfer causes the atoms to reconstruct to adapt to the potential energy surface, indicating the evolution of molecules along a charged potential energy surface. This evolution is accompanied by chemical transformation of the surface from excited-state decay to the ground state through additional vibrational energy, thereby lowering the transformation barrier [4] (Fig. 5.1a).

Kim et al. proposed a direct intramolecular excitation mechanism similar to plasmonic local-field-driven catalysis (Fig. 5.1b) [5, 6]. A direct transition from the ground to excited state can effectively occur when the photon energy of the plasmonic resonance is the same as the HOMO–LUMO energy gap of adsorbed molecules. For the molecular Cu/Ag system, the hybridization of electron orbitals between

© Tsinghua University Press 2022

Z. Zhang, *Plasmonic Photocatalysis*, Nanoscience and Nanotechnology,
https://doi.org/10.1007/978-981-19-5188-6_5

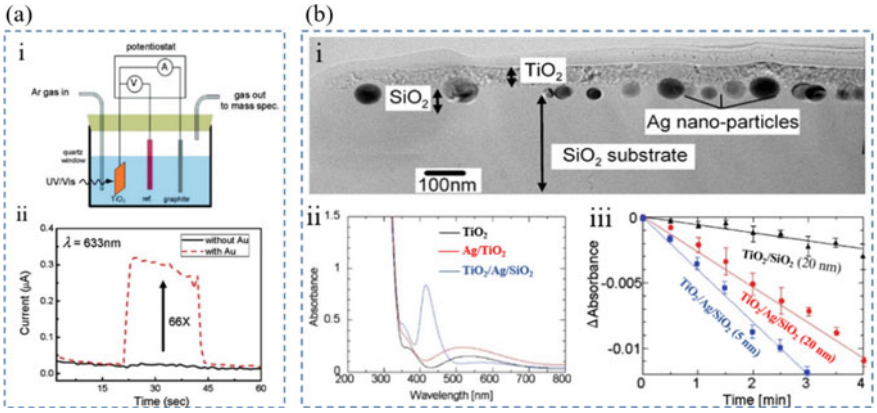

Fig. 5.1 Local field-effect-driven photocatalysis. **a** Schematic of plasmon-driven water splitting (i), and the photocurrent of anodic TiO_2 with and without Au NPs (ii) [8]; **b** TEM image of the cross-section of the TiO_2/Ag/SiO_2 substrate (i), absorption spectra (ii) and the decomposition rate of MB on the surface of TiO_2 (iii) [9]. Adapted with permission from Refs. [8] and [9]. Copyright 2011 and 2008 American Chemical Society

molecules and metals reduces the energy gap between the ground and excited states of the molecules, causing the energy required for molecular activation to shift from the UV to the visible region and providing a new means of low-energy photon excitation. Moreover, electron-orbital hybridization reduces the overlap between the molecular LUMO orbital and the electron orbital of metal substrate; thus, the molecule has a longer excited-state lifetime. In addition, the demethylation reaction induced by LSPR that converts methylene blue (MB) to thionine is ascribed to the plasmon-enhanced electronic excitation from HOMO to LUMO [7].

Under visible-light irradiation, the efficiency of photocatalytic water splitting is enhanced up to 66 times with assistance from the plasmonic field in Fig. 5.1c [8]. The rate of electron–hole-pair generation on the TiO_2 surface increases with the enhancement of the local field effect, leading to better photocatalytic activity. Moreover, under the action of the confined local field, the decomposition efficiency of MB on the TiO_2 surface is increased by sevenfold (Fig. 5.1d) [9]. The LSPR effect of AgNPs significantly increases the photon density in the near-UV region, which overlaps with the TiO_2 band gap. Then, a large number of electron–hole pairs in TiO_2 are excited to enhance its photocatalytic activity. Carter's group reported that heterometallic antenna reactor complexes using the Mo-doped Au nanostructure system can also promote catalytic properties due to amplified resonance-energy transfer caused by the enhanced plasmonic field [2, 10].

5.2 Hot-Electron-Driven Photocatalysis

Plasmonic hot carriers can be transferred to molecules through instantaneous electron exchange between the metal and reactant [11]. As shown in Fig. 5.2, transient negative ions (molecules with high-energy electrons) are generated via electronic exchange, and they survive on the metal surface for a time scale of tens of femtoseconds, promoting a plasmon-induced chemical reaction in the excited state or increasing the vibrational energy of the ground-state molecule. For this electron-transfer mechanism, the energies of hot electrons and hot holes must overlap with the unoccupied-state orbital of the molecule to achieve electron exchange. Specific chemical-reaction channels can be selectively enhanced by controlling the energy distribution of hot carriers to achieve a substantial increase in reaction efficiency and selectivity. The principle of hot-electron transfer in plasmon-induced photocatalysis (including indirect and direct transfer) is described in detail below.

5.2.1 Indirect Electron Transfer

Under Landau damping, due to the energy exchange between the EM wave of the plasmon resonance and the electrons and phonons in the metal, the collective coherent oscillation of electrons rapidly decays, generating hot-electron–hole pairs in the metal NPs [12] (Fig. 5.2a-i). The initially generated hot carriers form a hot Fermi–Dirac distribution through a thermalization process before transferring to the orbital of the adsorbed molecules (Fig. 5.2a-ii). Since hot electrons are continuously distributed near the Fermi level, the two-step indirect transfer process has high transfer efficiency and is the most effective excitation path for plasmonic catalysis, which is called indirect electron transfer. The efficiency of such transfers depends upon the position of the unoccupied-state orbital of the molecule relative to the Fermi level of the metal. However, controlling the Fermi levels of metals is difficult; that is, the energies of hot electrons cannot be effectively controlled by excitation light or LSPR, and thus the ability to selectively enhance specific chemical reactions is limited. Therefore,

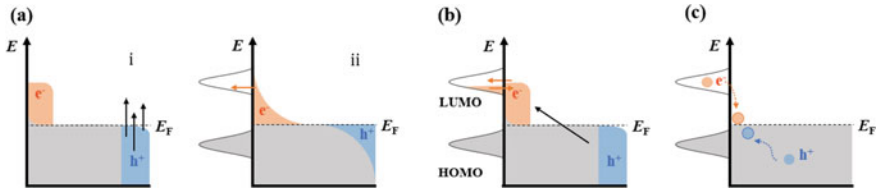

Fig. 5.2 Schematic of plasmon-driven hot-electron transfer from the metal to the adsorbed molecule. **a** Two-step indirect electron-transfer mechanism: (i) nonthermalized distribution of hot carriers; (ii) the Fermi–Dirac distribution of thermal carriers; **b** direct electron-transfer mechanism; **c** recombination of hot-electron–hole pairs in metals and the adsorbed molecule. E_F represents the Fermi energy, and the gray shadow represents the filled electronic states

effective enhancement of electronic excitation is observed by exciting LSPR, which has little influence on the electron distribution.

Most previous studies have attributed plasmonic catalysis to indirect hot-electron transfer [13, 14]. For example, using high-vacuum tip-enhanced Raman spectroscopy (HV-TERS), the in situ plasmon-induced chemical reactions of the p-nitrothiophenol (PNTP) molecule can provide a "hot spot" for exciting strong LSPR at the tip (Fig. 5.3a) [15]. The higher-density hot electrons generated from metal nanostructures are transferred to the unoccupied state of PNTP under stronger surface-plasmon resonances, resulting in dimerization of the PNTP during the catalytic process. The results show that the temperature does not significantly change during the reaction of PNTP catalyzed by plasmon. In addition, the absorption of the molecule occurs in the UV region, while the light excitation occurs in the visible region. Therefore, the thermal effect of surface plasmons and the contributions of photons during this reaction can be eliminated.

The effective dissociation of H_2 and O_2 molecules is of great significance in various photochemical transformation applications [16–20]. The indirect hot-electron transfer mechanism can be used to accelerate the dissociation of H_2 on the Au NPs' surface (Fig. 5.3b) [16]. The thermalization hot electrons generated by the Au NPs are transferred to the antibonding orbital of the H_2 molecules by the presence of a negative ion; these hot electrons then rapidly transfer back to the AuNPs' surface [21], and the H_2 molecules simultaneously return to the ground state. The additional vibrational energy caused by the hot-electron transfer results in the stretching of the H–H bond, ultimately leading to its dissociation. The effective dissociation of O_2 enables most plasmon-induced oxidation reactions, while high temperatures are always necessary for chemical reactions to occur in the traditional

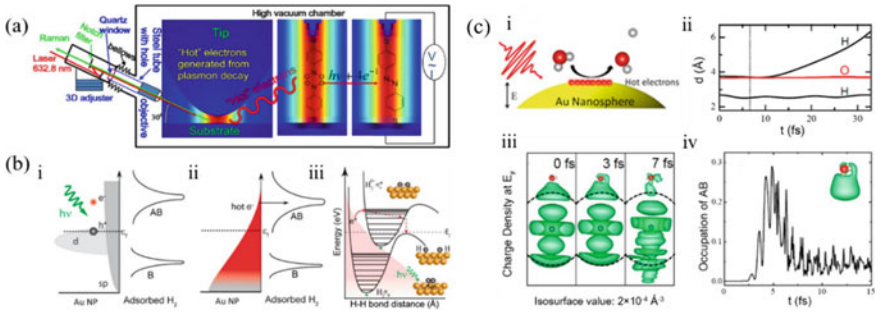

Fig. 5.3 Plasmonic hot-electron catalysis. **a** Hot-electron-induced chemical transformation of PNTP measured by HV-TERS technology [15]; **b** hot-electron-induced H_2 dissociation, (i) hot-electron excitation, (ii) indirect electron transfer, (iii) reaction mechanism of H_2 dissociation [16]; **c** (i) schematic of plasmon-driven water splitting with AuNP, (ii) the atomic distance d from H_2O to the surface of the AuNP changes with time, (iii) time-dependent charge density of the H_2O–Au system, (iv) occupation of the antibonding state of H_2O, and (v) wavelength-dependent photocatalytic rates [18]. Adapted with permission from Refs. [15, 16] and [18]. Copyright 2012 Springer Nature, 2013 and 2016 American Chemical Society

way. The hot electrons produced from surface-plasmon decay promote the dissociation of O_2 and the generation of oxygen activation with O_2^- [17]. In addition, the temperature required to achieve the oxidation reaction of CO and NH_3 with the aid of plasmonic hot electrons is much lower than that required to induce the reaction using only thermal excitation. In this catalysis process, the molecules are weakly adsorbed on the plasmonic metal nanostructures' surface through van der Waals forces, thereby forming relatively weak orbital hybridization. This promotes indirect transfer of plasmonic hot electrons.

5.2.2 Direct Electron Transfer

When adsorbates are present that can couple with electrons in the metal, a surface hybrid state of electrons can be formed at the interface, providing a new channel for plasmon resonance decay (that is, interface damping) [11, 22]. The formed interface state provides another pathway for the dephasing of the plasmon by the coupling between the hybrid state and the plasmon, directly generating a hot electron in the unoccupied orbitals of the adsorbate, thereby leaving a hot hole in the metal (Fig. 5.2b) [23]. The adsorbate acts as the acceptor of plasmon hot electrons, while the metal as an electron donor. If there is no electron–electron scattering occurs in the metal, the energy loss of the hot electrons can be significantly reduced in the catalytic process and the entire plasmon dephasing process can be accelerated.

The direct electron transfer process is less efficient than the indirect one due to the smaller transition dipole moment of the molecule–metal complex and the need to form a hybrid surface state. In addition, the energy overlap between the LSPR excitation and the energy gap of the surface hybrid state in the complex greatly influences the direct electron transfer efficiency, which can realize a direct resonance transition of the hybrid orbital of the system from the occupied orbit to the unoccupied one. Simultaneously, the direct charge-transfer channel can control the hot-electron distribution by regulating the LSPR properties of the plasmonic nanostructures and the conditions of light excitation, thereby selectively catalyzing the target reaction and increasing the rate of the target chemical transformation.

The atomic-scale real-time detection of the decomposition of water molecules on the surface of AuNPs under femtosecond laser excitation confirms the catalytic process of direct electron transfer (Fig. 5.3c) [18]. The energy and spatial coupling between the electron donors (AuNPs) and acceptors (H_2O) in the surface hybrid state of the molecule–metal hybrid system have laid the foundation for direct electron transfer. In the experiment, the gradual accumulation of the anti-bond states of water molecules and the decomposition of water molecules were observed rightly. The wavelength-dependent reaction rate depends on not only the resonance excitation of LSPR but also the plasmon excitation mode. In a specific plasmon excitation mode, a better energy overlap is present between the electron acceptor and donor, resulting in more efficient direct electron transfer.

5.3 Plasmon-Exciton Co-driven Photocatalysis

The interactions between light matter and EM waves can be controlled by the plasmon-exciton interaction in metal–semiconductor nanostructures at the nanoscale [24, 25]. Surface plasmons are electrons-collective oscillations in the conduction bands of metal nanostructures [26, 27]. They are derived from the dielectric constant between the metal nanostructures and the nonconductive environment, in which the resonance wavelength is regulated by the shape and size of metal nanostructures. Electronic levels in the conduction and valence bands of the semiconductor nanostructures are discrete in one or more dimensions due to quantum confinement [28]. The bound electron–hole pairs or excitons are formed by the transitions between these discrete levels under optical excitations. The mechanism of cavity quantum electrodynamics is used to analyze the quantum interactions between light and matter inside a micro/nano-cavity. The Jaynes-Cummings model reveals that the dipole interaction between an emitter [29]. The excitons of metal–semiconductor hybrid nanostructures with EM-field modes are often as a two-level system interacting with a quantum harmonic oscillator [30]. In this section, we will introduce the mechanism of the plasmon-exciton coupling interactions in two interaction regimes, including weak and strong couplings. This will allow a better understanding of the physical mechanism behind metal–semiconductor systems.

The schematic of the exciton-SPP interaction for strong and weak coupling is shown in Fig. 5.4. For strong coupling interactions, $\Omega_R > \frac{\gamma_x^2}{2} + \frac{\gamma^2}{2}$, where γ is the field mode and γ_x is the effective dephasing of excitons [31]. The Rabi frequency is $\Omega_R = \mu E$, where μ is the excitonic dipole moment and E is the vacuum field associated with the coupled mode [32]. The electronic oscillations in upper polaritons (UPs) with high energy and lower polaritons (LPs) with low energy are formed by 2 Ω_R. The Rabi frequency in the strong coupling interaction is greater than the sum of the effective dephasing of the exciton and field modes [33]. For the weak coupling system, the interaction is weaker and the lifetime of LSPR is relatively shorter than the spontaneous decay rate of the isolated emitter [34]. The weak coupling regime is characterized by an enhanced damping rate corresponding to the increase in the density of states associated with the resonator. According to the Purcell factor $F = \frac{3}{4\pi^2}\left(\frac{\lambda_0}{n_0}\right)^3 \frac{Q}{V}$, where n_0 is the refractive index, Q is the resonator quality factor and V is the mode volume, which can describe the decay rate of the emitter modified by the effect of cavity in the weak coupling regime [35]. If the $F > 1$, the spontaneous decay rate will be enhanced. Moreover, the enhancement in quantum yield can be determined by the radiative and nonradiative decay rates.

Plasmon-driven surface catalytic reactions have been widely investigated in recent years due to the higher sensitivity on the surface and the excellent catalytic efficiency. However, the conversion efficiency of the plasmon-to-hot electron is lower than 1% and the lifetime of the plasmonic hot electrons generated by the LSPR decay progress is as short as 150 fs in the surface catalytic reaction, leading to lower

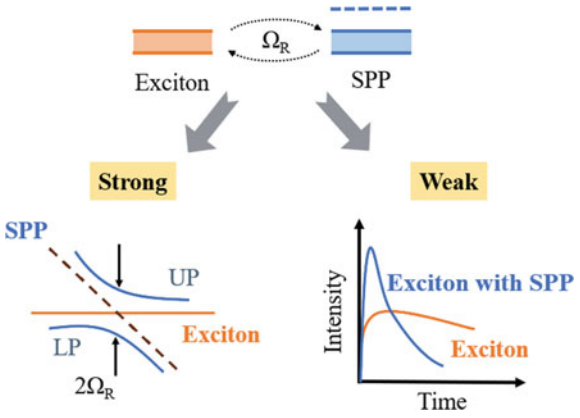

Fig. 5.4 Schematic of the exciton-SPP interaction in the strong and weak coupling regimes

efficiency and probability of plasmon-induced hot-electron transfer chemical reactions [26, 36]. Therefore, an effective system is needed to increase the lifetime and density of plasmonic hot electrons. As a kind of excellent electron acceptability, semiconductor materials have generated great interest in the field of photocatalysis. By combining noble metals and semiconductors, the excitons in the metal oxides strongly couple to the LSPR, leading to significant prolonging of the hot-electron lifetime from femtoseconds to picoseconds, thus enhancing the efficiency of plasmon-driven surface catalytic reactions [37, 38]. By regulating the optical and electronic properties of hybrid structures, plasmon-exciton coupling interactions can be further improved, thereby facilitating the probability and efficiency of surface catalytic reactions.

The hybrid materials of plasmonic metal-TiO_2 serve as catalytic platforms for investigating the surface catalytic performance and the ultrafast conversion due to their excellent optical and photochemical activities [39]. The proposed reaction mechanism is that hot electrons are transferred from metal nanostructures to the conduction band of the TiO_2, leading to the energetic holes promoting the oxidation reaction for the PATP into DMAB. The researchers developed an AgNPs–TiO_2 hybrid system using the UV-photoreduction method (Fig. 5.5). The plasmon-exciton coupling strength can be controlled by changing the size of AgNPs with different LSPR peaks. When the LSPR peak of AgNPs overlaps with the absorption peak of the TiO_2 film, the strongest plasmon coupling occurs. This provides an optimal catalytic platform for a better understanding of the plasmon-exciton co-driven surface catalytic reaction.

Transition-metal dichalcogenide (TMD) monolayers have driven great scholarly interest in light-matter interactions due to their reduced screening effect, large exciton effect, and huge transition dipole moment. Strong coupling between plasmons and TMD excitons in nanocavities can result in the formation of hybrid plexcitonic states. As shown in Fig. 5.6a, Xu et al. realized the strong coupling of surface plasmons on an individual silver nanorod (AgNR) with excitons in a monolayer of WSe_2 [40]. They explored a method for measuring the dispersion relation of plexcitons in the hybrid

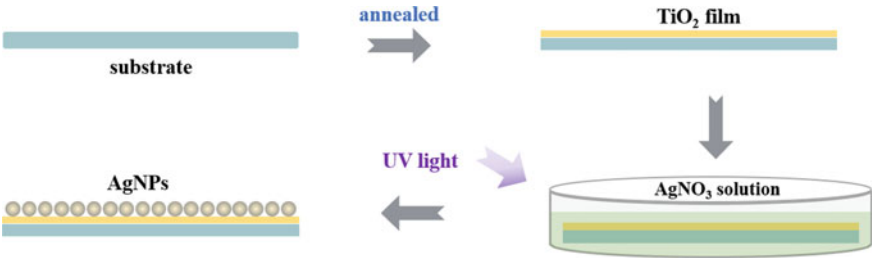

Fig. 5.5 The schematic of AgNPs growth on the TiO_2 surface under UV irradiation

nanocavity, a promising approach for controlling the excitons in semiconductors for optical and optoelectronic applications. In addition, the light-emitting plexcitons from the coupling between the neutral excitons in the WSe_2 monolayer and the nanocavity plasmons in the nanocube-over-mirror system were also investigated (Fig. 5.6b) [41]. A photoluminescence enhancement of 1700 times was observed in the WSe_2 monolayer within the hot spot and an anticrossing dispersion curve of the hybrid system was obtained in the dark-field scattering spectrum, which is attributed to the enhanced local density of states by both the plasmonic and excitonic constituents in the intermediate-coupling regime.

5.4 Thermal-Effect-Driven Photocatalysis

The localized thermal effect followed by LSPR decay can overcome reaction barriers by providing energy to the reactants in the catalytic process, which is an effective way of inducing chemical reactions using plasmons. Photocatalysis based on photoactive plasmonic metal nanostructures has become a promising method for achieving photo-driven chemical conversion under actual conditions much milder than traditional thermal catalysis. However, the inevitable thermal effect in the plasmon decay process can only increase the reaction rate but can't increase the reaction selectivity. In addition, the contributions of the thermal and nonthermal effects in plasmon-induced catalytic reactions are really hard to distinguish. Although it is widely accepted that the main role of plasmonic catalysis is the excitation of hot electrons rather than the thermal effects, some differences of opinion still exist on this issue [42–45].

As shown in Fig. 5.7a, the reaction rates of CO_2 have been studied as a function of laser intensity by employing RhNPs as plasmonic catalysts [46]. The nonthermal effect of the plasmon catalyst is synergetic with heating through temperature measurement of the catalyst bed. Moreover, the relative contributions of hot electrons and thermal effects were quantitatively analyzed for the plasmon-induced catalytic reaction using scanning electrochemical microscopy (SECM) (Fig. 5.7b) [47]. Both hot carriers and thermal effects contribute to the efficiency of plasmon catalytic, and the relative contribution varies with changing excitation intensity.

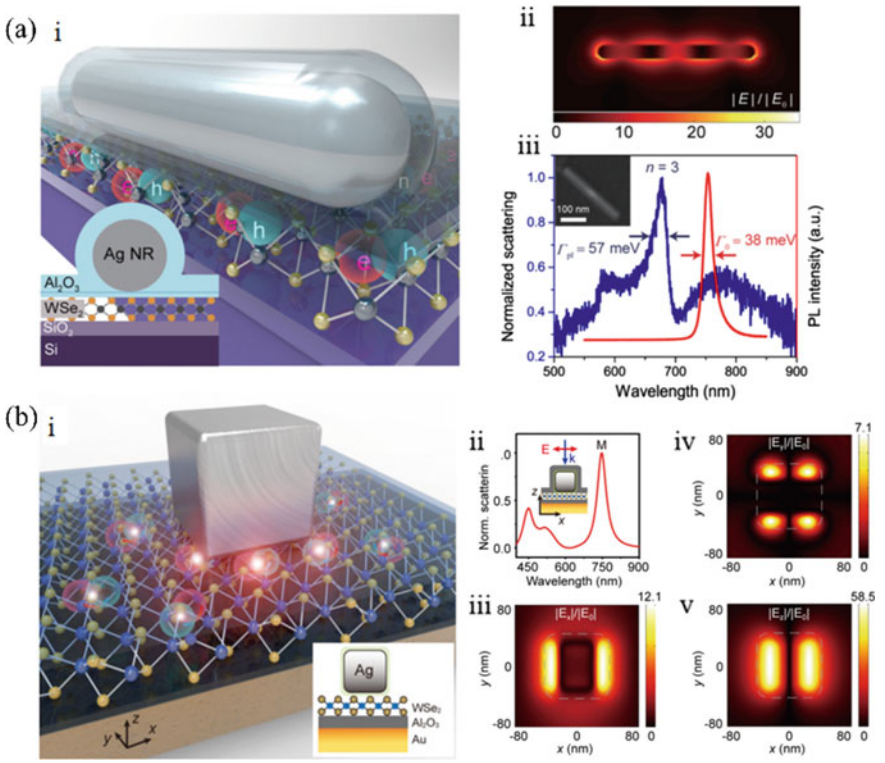

Fig. 5.6 The coupling of plasmons and TMD excitons in nanocavity systems. **a** Schematic of the structure with a single AgNR on a WSe_2 monolayer (i); EM simulation of the near-field distribution of the $n = 3$ AgNR-plasmon mode (ii); photoluminescence spectrum of a single-layer WSe_2 and dark-field-scattering spectrum of an uncoupled AgNR; the inset shows the SEM image of the AgNR (iii) [40]; **b** schematic of the structure with an Ag nanocube on a WSe_2 monolayer; the substrate is the ultra-smooth Au film with an Al_2O_3 deposition and a polyvinylpyrrolidone (PVP) layer around the nanocube. Red and blue spheres represent in-plane excitons (i); simulated scattering spectrum of the system excited by a normally incident *x*-polarized plane wave (ii); the scattered electric-field distribution of the *x*-, *y*-, and *z*-components at the central plane of the WSe_2 layer (iii)–(v) [41]. Adapted with permission from Refs. [41] and [42]. Copyright 2017 and 2018 American Chemical Society

The influence of light illumination upon electron and thermal excitations is considered by introducing the light-dependent activation barrier, and the thermal and nonthermal effects in the plasmon catalysis process are differentiated [48]. The surface temperature of the metal nanostructure is monitored by using a thermal imaging camera to elucidate photothermal effect under different laser wavelengths and intensities. This proves that the reduction of the light-induced reaction barrier is due to hot electrons, which are able to cause multiple vibrational transitions of reactant molecules. As the vibrational energy stored in the bond increases, the activation energy decreases.

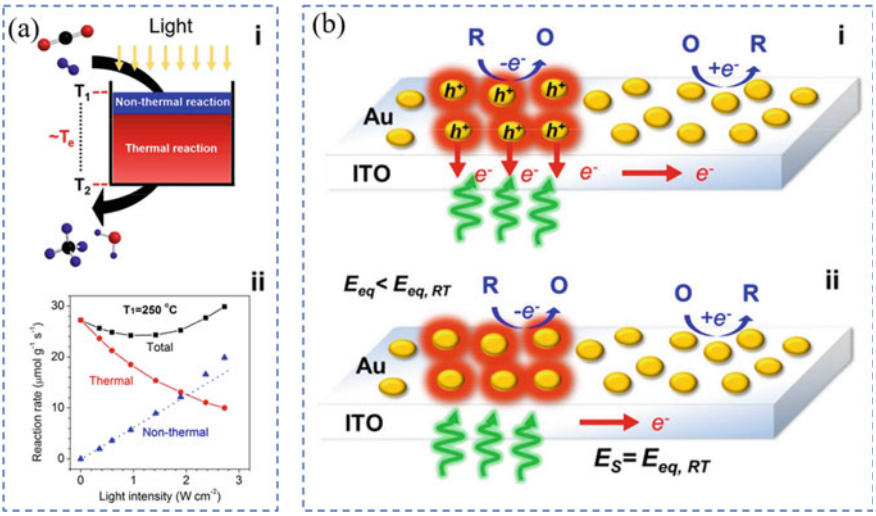

Fig. 5.7 Thermal-effect-driven photocatalysis. **a** Schematic of the plasmonic thermal-induced reaction for CO_2 with Rh/TiO_2 catalyst (i), reaction rates (corresponding to the thermal, nonthermal, and total effects) as functions of laser intensity (ii) [46]; **b** schematic of the mechanism of plasmon hot holes (i) and the thermal effects (ii) induced oxidation reactions [47]. Adapted with permission from Refs. [47] and [48]. Copyright 2018 American Chemical Society

References

1. Amendola V, Pilot R, Frasconi M, Marago OM, Iati MA (2017) Surface plasmon resonance in gold nanoparticles: a review. J Phys Condens Matter 29:48
2. Martirez JMP, Carter EA (2017) Prediction of a low-temperature N_2 dissociation catalyst exploiting near-IR-to-visible light nanoplasmonics. Sci Adv 3
3. Kazuma E, Kim Y (2019) Mechanistic studies of plasmon chemistry on metal catalysts. Angew Chem Int Ed 58:4800–4808
4. Aslam U, Rao VG, Chavez S, Linic S (2018) Catalytic conversion of solar to chemical energy on plasmonic metal nanostructures. Nat Catal 1:656–665
5. Kazuma E, Jung J, Ueba H, Trenary M, Kim Y (2017) Direct pathway to molecular photodissociation on metal surfaces using visible light. J Am Chem Soc 139:3115–3121
6. Kazuma E, Jung J, Ueba H, Trenary M, Kim Y (2018) Real-space and real-time observation of a plasmon-induced chemical reaction of a single molecule. Science 360:521–526
7. Tesema TE, Kafle B, Tadesse MG, Habteyes TG (2017) Plasmon-enhanced resonant excitation and demethylation of methylene blue. J Phys Chem C 121:7421–7428
8. Liu Z, Hou W, Pavaskar P, Aykol M, Cronin SB (2011) Plasmon resonant enhancement of photocatalytic water splitting under visible illumination. Nano Lett 11:1111–1116
9. Awazu K, Fujimaki M, Rockstuhl C, Tominaga J, Murakami H, Ohki Y, Yoshida N, Watanabe T (2008) A plasmonic photocatalyst consisting of sliver nanoparticles embedded in titanium dioxide. J Am Chem Soc 130:1676–1680
10. Spata VA, Carter EA (2018) Mechanistic insights into photocatalyzed hydrogen desorption from palladium surfaces assisted by localized surface plasmon resonances. ACS Nano 12:3512–3522
11. Zhang YC, He S, Guo WX, Hu Y, Huang JW, Mulcahy JR, Wei WD (2018) Surface-plasmon-driven hot electron photochemistry. Chem Rev 118:2927–2954

12. Lim M, Lee SS, Lee BJ (2013) Near-field thermal radiation between graphene-covered doped silicon plates. Opt Express 21:22173–22185
13. Naldoni A, Montini T, Malara F, Mr ZMM, Beltram A, Virgili T, Boldrini CL, Marelli M, Romero-Oca AI, Delgado JJ, dal Santo V, Fornasiero P (2017) Hot electron collection on brookite nanorods lateral facets for plasmon-enhanced water oxidation. ACS Catal 7:1270–1278
14. Sakamoto H, Ohara T, Yasumoto N, Shiraishi Y, Ichikawa S, Tanaka S, Hirai T (2015) Hot-electron-induced highly efficient O_2 activation by Pt nanoparticles supported on Ta_2O_5 driven by visible light. J Am Chem Soc 137:9324–9332
15. Sun M, Zhang Z, Zheng H, Xu H (2012) In-situ plasmon-driven chemical reactions revealed by high vacuum tip-enhanced Raman spectroscopy. Sci Rep 2:647
16. Mukherjee S, Libisch F, Large N, Neumann O, Brown LV, Cheng J, Lassiter JB, Carter EA, Nordlander P, Halas NJ (2013) Hot electrons do the impossible: plasmon-induced dissociation of H_2 on Au. Nano Lett 13:240–247
17. Christopher P, Xin H, Linic S (2011) Visible-light-enhanced catalytic oxidation reactions on plasmonic silver nanostructures. Nat Chem 3:467–472
18. Yan L, Wang F, Meng S (2016) Quantum mode selectivity of plasmon-induced water splitting on gold nanoparticles. ACS Nano 10:5452–5458
19. Mukherjee S, Libisch F, Large N, Neumann O, Brown LV, Cheng J, Lassiter JB, Carter EA, Nordlander P, Halas NJ (2012) Hot electrons do the impossible: plasmon-induced dissociation of H_2 on Au. Nano Lett 13:240–247
20. Mukherjee S, Zhou L, Goodman AM, Large N, Ayala-Orozco C, Zhang Y, Nordlander P, Halas NJ (2013) Hot-electron-induced dissociation of H_2 on gold nanoparticles supported on SiO_2. J Am Chem Soc 136:64–67
21. Liu JG, Zhang H, Link S, Nordlander P (2017) Relaxation of plasmon-induced hot carriers. ACS Photonics 5:2584–2595
22. Chen YC, Hsu YK, Popescu R, Gerthsen D, Lin YG, Feldmann C (2018) Au@Nb@HxK1-xNbO$_3$ nanopeapods with near-infrared active plasmonic hot-electron injection for water splitting. Nat Commun 9
23. Foerster B, Joplin A, Kaefer K, Celiksoy S, Link S, Nnichsen C (2017) Chemical interface damping depends on electrons reaching the surface. ACS Nano 11:2886–2893
24. Fofang NT, Park TH, Neumann O, Mirin NA, Nordlander P, Halas NJ (2008) Plexcitonic nanoparticles: plasmon-exciton coupling in nanoshell-J-aggregate complexes. Nano Lett 8:3481–3487
25. Lee J, Govorov AO, Dulka J, Kotov NA (2004) Bioconjugates of CdTe nanowires and Au nanoparticles: plasmon-exciton interactions, luminescence enhancement, and collective effects. Nano Lett 2323–2330
26. Brongersma ML, Halas NJ, Nordlander P (2015) Plasmon-induced hot carrier science and technology. Nat Nanotechnol 10:25–34
27. Pitarke JM, Silkin VM, Chulkov EV, Echenique PM (2007) Theory of surface plasmons and surface-plasmon polaritons. Rep Prog Phys 70
28. Achermann M (2010) Exciton-plasmon interactions in metal-semiconductor nanostructures. J Phys Chem Lett 1:2837–2843
29. Fofang NT, Grady NK, Fan ZY, Govorov AO, Halas NJ (2011) Plexciton dynamics: exciton-plasmon coupling in a J-aggregate-Au nanoshell complex provides a mechanism for nonlinearity. Nano Lett 11:1556–1560
30. Vasa P, Lienau C (2018) Strong light-matter interaction in quantum emitter/metal hybrid nanostructures. ACS Photonics 5:2–23
31. Vasa P, Lienau C (2017) Strong light–matter interaction in quantum emitter/metal hybrid nanostructures. ACS Photonics 5:2–23
32. Torma P, Barnes WL (2015) Strong coupling between surface plasmon polaritons and emitters: a review. Rep Prog Phys 78
33. Vasa P (2020) Exciton-surface plasmon polariton interactions. Adv Phys X 5:1749884

34. Giannini V, Fernandez-Dominguez AI, Heck SC, Maier SA (2011) Plasmonic nanoantennas: fundamentals and their use in controlling the radiative properties of nanoemitters. Chem Rev 111:3888–3912
35. Tischler JR, Bradley MS, Zhang Q, Atay T, Nurmikko A, Bulovic V (2007) Solid state cavity QED: strong coupling in organic thin films. Org Electron 8:94–113
36. Kale MJ, Avanesian T, Christopher P (2014) Direct photocatalysis by plasmonic nanostructures. ACS Catal 4:116–128
37. Ding Q, Shi Y, Chen M, Li H, Yang X, Qu Y, Liang W, Sun M (2016) Ultrafast dynamics of plasmon-exciton interaction of Ag nanowire-graphene hybrids for surface catalytic reactions. Sci Rep 6:32724
38. Lin WH, Shi Y, Yang XZ, Li J, Cao E, Xu XF, Pullerits T, Liang WJ, Sun MT (2017) Physical mechanism on exciton-plasmon coupling revealed by femtosecond pump-probe transient absorption spectroscopy. Mater Today Phys 3:33–40
39. Ding Q, Li R, Chen M, Sun M (2017) Ag nanoparticles-TiO_2 film hybrid for plasmon-exciton co-driven surface catalytic reactions. Appl Mater Today 9:251–258
40. Zheng D, Zhang S, Deng Q, Kang M, Nordlander P, Xu H (2017) Manipulating coherent plasmon-exciton interaction in a single silver nanorod on monolayer WSe_2. Nano Lett 17:3809–3814
41. Sun J, Hu H, Zheng D, Zhang D, Deng Q, Zhang S, Xu H (2018) Light-emitting plexciton: exploiting plasmon-exciton interaction in the intermediate coupling regime. ACS Nano 12:10393–10402
42. Zhang X, Li X, Reish ME, Zhang D, Su NQ, Guti Rrez Y, Moreno F, Yang W, Everitt HO, Liu J (2018) Plasmon-enhanced catalysis: distinguishing thermal and nonthermal effects. Nano Lett 18:1714–1723
43. Keller EL, Frontiera RR (2018) Ultrafast nanoscale Raman thermometry proves heating is not a primary mechanism for plasmon-driven photocatalysis. ACS Nano 12:5848–5855
44. Kamarudheen R, Castellanos GW, Kamp LPJ, Clercx HJH, Baldi A (2018) Quantifying photothermal and hot charge carrier effects in plasmon-driven nanoparticle syntheses. ACS Nano 12:8447–8455
45. Golubev AA, Khlebtsov BN, Rodriguez RD, Chen Y, Zahn DRT (2018) Plasmonic heating plays a dominant role in the plasmon-induced photocatalytic reduction of 4-nitrobenzenethiol. J Phys Chem C 122:5657–5663
46. Zhang X, Li XQ, Reish ME, Zhang D, Su NQ, Gutierrez Y, Moreno F, Yang WT, Everitt HO, Liu J (2018) Plasmon-enhanced catalysis: distinguishing thermal and nonthermal effects. Nano Lett 18:1714–1723
47. Yu Y, Sundaresan V, Willets KA (2018) Hot carriers versus thermal effects: resolving the enhancement mechanisms for plasmon-mediated photoelectrochemical reactions. J Phys Chem C 122:5040–5048
48. Zhou L, Swearer DF, Zhang C, Robatjazi H, Zhao H, Henderson L, Dong L, Christopher P, Carter EA, Nordlander P, Halas NJ (2018) Quantifying hot carrier and thermal contributions in plasmonic photocatalysis. Science 362:69–72

Chapter 6
Measurement and Analysis of Plasmon-Driven Photocatalysis

After exploring the fundamental mechanism of plasmon-driven photocatalysis, some measurement and analytical methods are introduced in this chapter. The performance of the plasmonic photocatalytic reaction depends on the noble-metal nanostructures with LSPR; thus, designing suitable plasmonic structures is necessary to achieve better catalytic efficiency. Due to the complexity of the surface-plasmon catalytic mechanism, reasonable selection and comprehensive application of characterization techniques are essential for achieving an accurate description of plasmon-driven photocatalysis.

6.1 Design of Surface-Plasmon Structures

Plasmonic photocatalysis is an important research achievement of the LSPR of metal nanostructures, which is an effective approach to enhancing light energy conversion [1]. When the incident light frequency is the same as the charge collective oscillation one, LSPR can greatly enhance the light-absorption efficiency of metal nanostructures, and form instantaneous high-density charge oscillations on the metal surface, resulting in enhanced local EM fields [2], hence greatly enhance the Raman scattering intensity of molecules [3].

The photocatalytic performance largely depends on the LSPR effect of noble-metal nanostructures with controllable shape and size [4]. Thus designing a simple and efficient surface-plasmon structure is essential for realizing a highly reactive photocatalytic reaction. Gold and silver nanostructures are most commonly thought of as photocatalysts and can offer better plasmonic support in terms of photocatalysis. Other metals also afford the LSPR effect, such as AlNPs with LSPR in the UV region. Due to the low intrinsic loss of silver, plasmonic nanostructures with narrow LSPR, high oscillation intensity, and large optical-field enhancements are advantageous for high catalytic efficiency. However, the plasmonic performance of silver nanostructures is unstable because they easily oxidize in air. Gold is an inert

© Tsinghua University Press 2022

Z. Zhang, *Plasmonic Photocatalysis*, Nanoscience and Nanotechnology,
https://doi.org/10.1007/978-981-19-5188-6_6

metal nanostructure with a higher inherent loss than silver, particularly in the short wavelength range of the visible spectra [5]. The sizes and shapes of metal nanostructures can be tuned via photolithography or colloidal synthesis [6]. Normally, the former is suitable for structures $\geq$ 100 nm, while the latter is suitable for structures < 100 nm. The location of metal nanostructures can be directly controlled by photolithography, even if large arrays with sizes of 100 nm can be fabricated [7]. Self-assembly of colloidal-metal nanostructures provides a cost-effective method for aligning NPs [8, 9]. In addition, uniform periodic surface structures of metals are achieved over a large area using a deposition technique, such as thermal or electron-beam evaporation. Then, metal nanoislands (NIs) are fabricated based on solid-state dewetting under laser irradiation, whose LSPR effect can be controlled by changing the evaporation thickness, annealing temperature, and film strain [10–12].

Plasmonic nanostructures have important potential applications in many fields, including improving reaction rates and selectivities in the chemical industry, providing photothermal therapy in the biological branch, and enhancing the efficiency of photovoltaic cells in the energy area. In recent years, plasmon-catalyzed chemical reactions based on different metal nanostructures have received extensive attention from researchers. Encouraging results show that the hot electrons produced by the AgNPs are transferred to the molecules attached to the metal surface, thereby driving the reduction reaction. Duchene et al. designed the Au/p–GaN metal–semiconductor structure capable of capturing the hot holes generated by the plasmon relaxation of AuNPs, driving the CO_2-reduction reaction, and improving the selectivity of the reaction product CO (Fig. 6.1) [13]. Halas et al. discovered a simple technique for synthesizing aluminum nanocrystals with high purity that can be scaled up to 70–220 nm by simply modifying the proportion of solvent in the reaction solution (Fig. 6.2) [14]. Chen et al. reported the enhancement of the local EM field of WSe_2 by depositing an AuNI film with a thickness of 5 nm on a WSe_2 monolayer film, improving its catalytic performance in the visible region (Fig. 6.3) [15]. Kong et al. realized crystal transformation from polycrystalline $NaYF_4$ to a single-crystal Y_2O_3 material by assistance of plasmonic AuNIs with different annealing temperatures (Fig. 6.4) [16]. Akshaya et al. designed a simple and efficient method for the aqueous synthesis of Au@Ag core–shell NPs, which are stable, uniform, and adjustable in size with a higher SERS efficiency under near-infrared excitation (Fig. 6.5) [17]. Xie and Schlücker designed a single dual-function 3D superstructure comprising small Au satellites self-assembling on a large shell-isolated gold core in 2013 and designed a satellite-structured AgNPs to perform the reduction reaction of 4-nitrothiophenol (PNTP) to 4-aminothiophenol (PATP) without chemical reducing agents in 2015 (Fig. 6.6) [18, 19]. Zhu's group explored a 3D self-assembled AlNPs for plasmon-enhanced solar desalination, which can efficiently enhance the solar absorption and enable effective desalination ability (Fig. 6.7) [20].

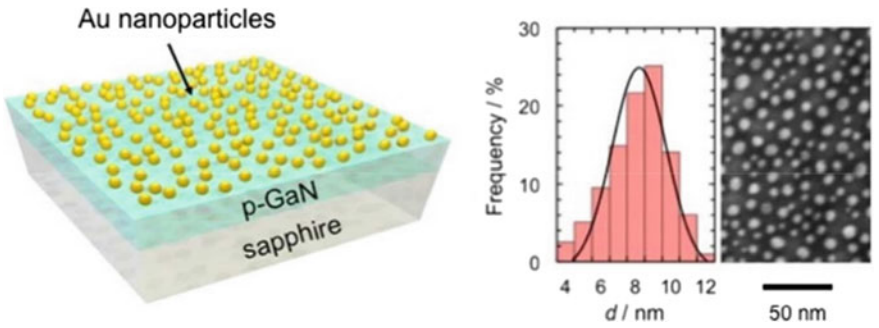

Fig. 6.1 Schematic of CO_2 photochemical reduction reaction with a metal–semiconductor structure of plasmonic AuNPs on p-GaN [13]. Adapted with permission from Ref. [13]. Copyright 2018 American Chemical Society

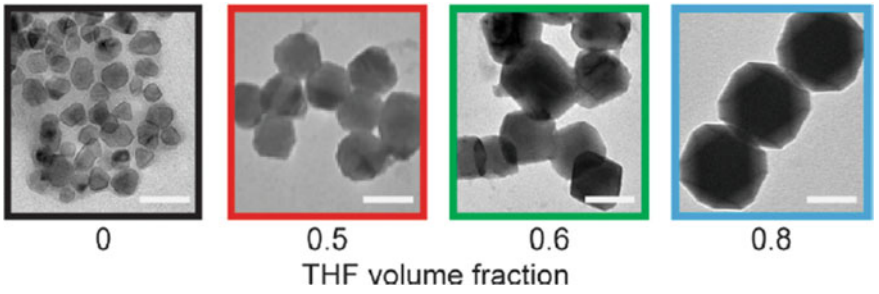

Fig. 6.2 TEM images of aluminum nanocrystals with different sizes, scale bar = 100 nm [14]. Adapted with permission from Ref. [14]. Copyright 2015 American Chemical Society

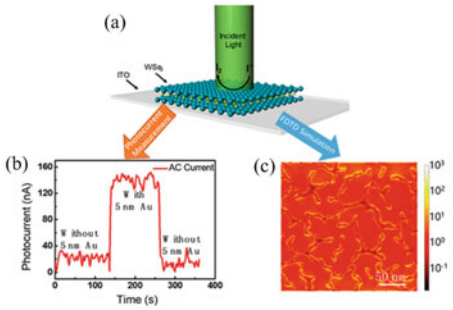

Fig. 6.3 Plasmonic enhancement of photocatalysis on monolayer WSe_2 with AuNIs. **a** Schematic of an iodine redox reaction with AuNIs; **b** measurements of AC current with and without AuNIs for the monolayer WSe_2 electrode under visible excitation; **c** enhancement factor of the interface electric-field intensity of AuNIs/WSe_2 monolayer, as calculated by the FDTD method [15]. Adapted with permission from Ref. [15]. Copyright 2019 American Chemical Society

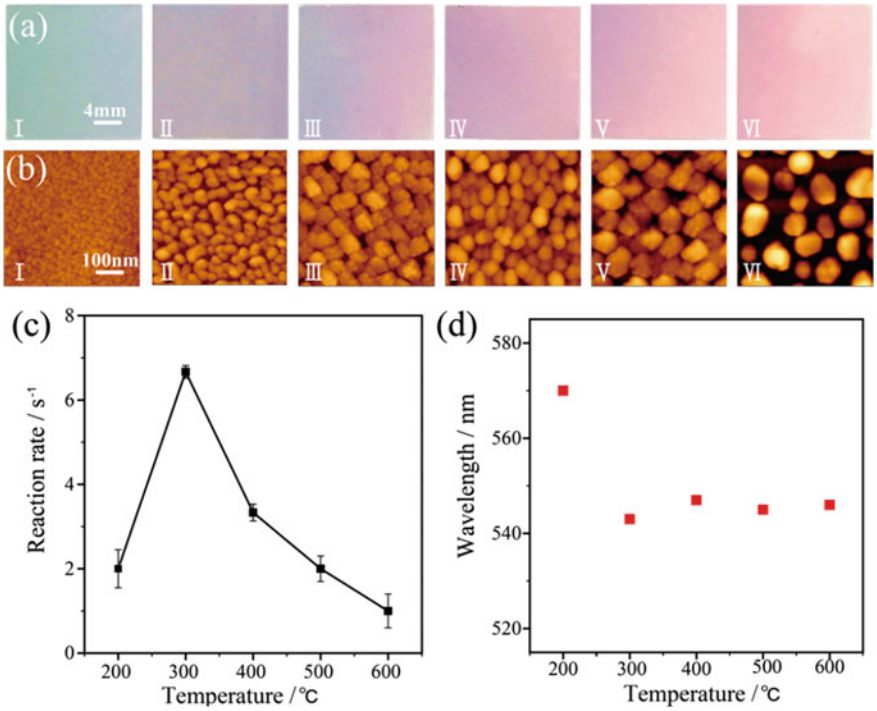

Fig. 6.4 Plasmon-driven crystal transformation with AuNIs. **a** Optical images and **b** AFM images of AuNIs film with different sizes and gaps (AuNIs annealed at 200–600 °C are shown in II-VI, respectively); **c** Reaction rates and **d** LSPR extinction peaks of AuNIs (II–VI NIs) [16]. Adapted with permission from Ref. [16]

6.2 Measurement by Chromatography and Electron Microscopy

Gas chromatography (GC) and gas chromatography-mass spectrometry (GC–MS) are common techniques for the separation and quantitative analysis of gas-phase components and are effective tools for studying surface-plasmon gas catalytic reactions. High-performance liquid chromatography is a liquid-phase sample analysis technology that pumps the sample from the mobile phase into a chromatographic column for separation. This method can realize separation, component identification, and quantitative analysis of the mixture, hence, widely used for chemical analysis and biological detection. Zeng et al. first reported a true plasmonic *z*-scheme photocatalyst based on an Au/TiO_2 heterojunction [21]. GC–MS was employed to analyze the obtained gas samples and verify that the products were generated from the photocatalytic reaction. CH_4 (302 μmol/(g h) with 89.3% selectivity) was observed as

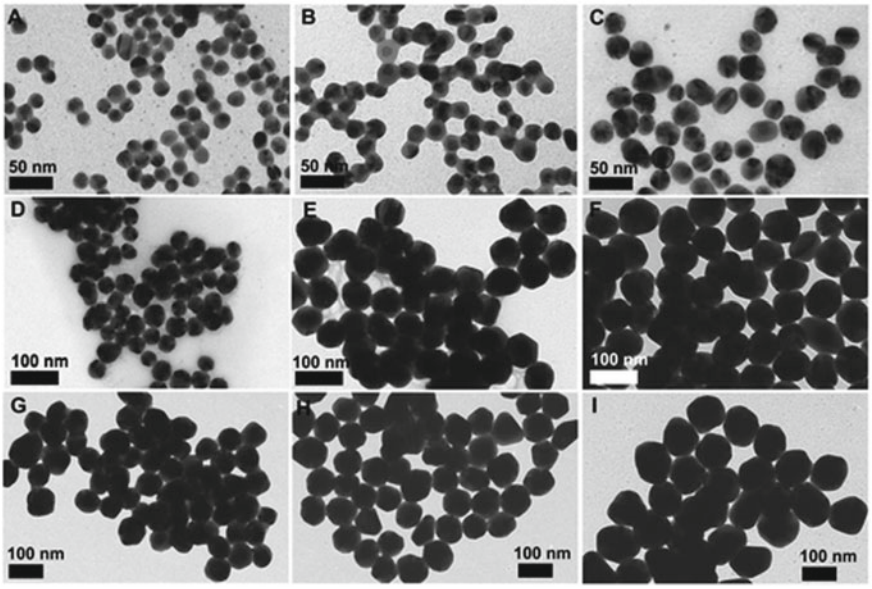

Fig. 6.5 TEM images of Au@Ag core-shell NPs of different sizes from 20 nm (**a**) to 120 nm (**i**) [17]. Adapted with permission from Ref. [17]. Copyright 2013 American Chemical Society

the dominant CO_2 photoreduction product under simulated sunlight while CH_2O [420 μmol/(g h)] and CO [323 μmol/(g h)] were predominantly produced under visible + UV light.

In addition to chromatography and mass spectrometry for monitoring in situ plasmon catalysis, other techniques are very suitable for specific systems and molecules. Scanning transmission electron microscopy (STEM) is often used to characterize the microstructure of nanoscale samples, which is essential for studying plasmon-induced phase transitions and catalytic reactions. Vadai et al. proposed an experimental method combining STEM and optical excitation to achieve in situ and real-time monitoring of the plasmon-driven dehydrogenation phase transition of a single palladium nanocube as well as nanoscale spatial resolution [22]. The reaction process was characterized, as shown in Fig. 6.8. The figure shows that the transition of the palladium nanocube from the hydrogen-rich phase to the hydrogen-depleted phase occurs in two steps, and the activation-energy barriers of the two-step reactions differ noticeably. The phase-change reaction can also achieve selectivity of the reaction site by changing the position of the plasmon hot spot. This result indicates that STEM in combination with optical excitation is expected to become a powerful tool for exploring single-NP-plasmon photocatalytic processes.

Based on the principle of quantum tunneling, STM not only obtains images of the sample surface at atomic-level resolution but also manipulates molecules or atoms. Bin Ren et al. reported that the electronic and catalytic properties at specific locations on the Pd/Au(111) bimetal surface can be spatially resolved with a resolution of 3 nm

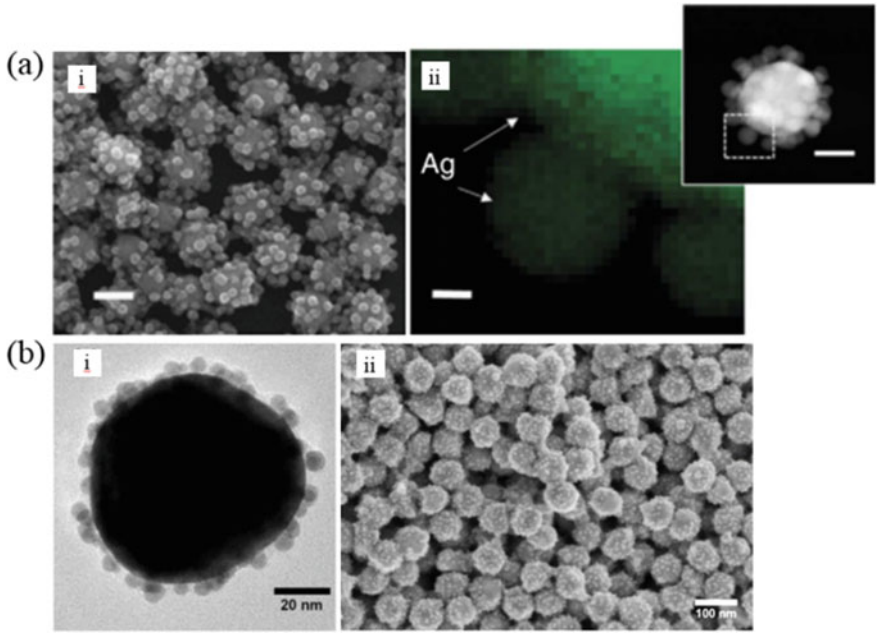

Fig. 6.6 The design of plasmonic satellites structure. **a** SEM image (scale bar = 100 nm) (i) and EDS element mapping (scale bar = 10 nm) and the corresponding STEM image (scale bar = 50 nm) of Ag superstructure (ii) [18]; **b** TEM image (i) and SEM image of Au superstructure (ii) [19]. Adapted with permission from Refs. [18] and [19]. Copyright 2015 Springer Nature and 2013 American Chemical Society

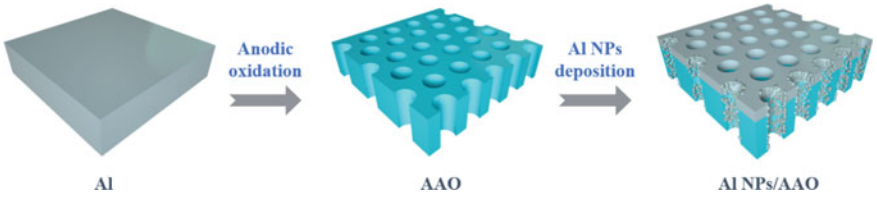

Fig. 6.7 Schematics of the fabrication process of the plasmonic AlNPs/AAO structure

in real-space via STM [23]. It shows that in comparison to the Pd terrace, the C≡N bond is weakened and the reactivity of the phenyl isocyanide adsorbed on the edge of the Pd step is enhanced. Moreover, a 3 nm spatial resolution was attributed to the enhanced electric field and unique electronic properties at the edge of the step.

Scanning electrochemical microscopy (SECM) is based on electrochemical principles and uses electrode probes to scan samples to obtain electrochemical information about chemical reactions of substances in the microregion. Yu et al. proposed a method of using SECM to explore the hot electrons and local temperature in the plasmon catalysis process, as shown in Fig. 6.9 [24]. The electrode tip is moved close

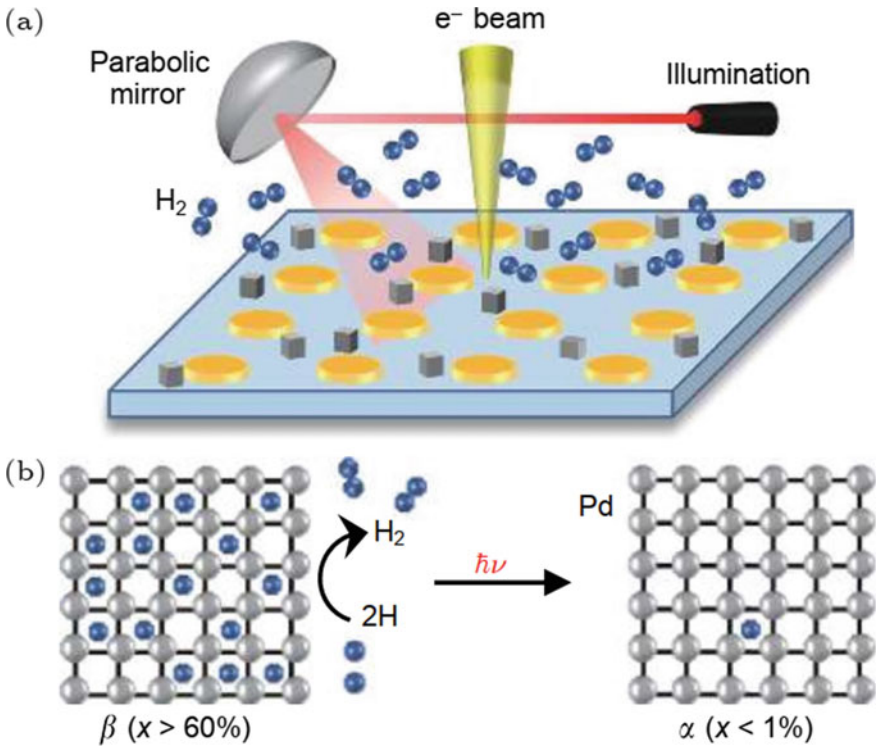

Fig. 6.8 Plasmon-induced phase transition by STEM technology. **a** Schematic of the STEM monitoring of plasmon-induced Pb nanocube phase transitions; **b** schematic of the phase transition of the Pb nanocube from the beta phase to the alpha phase under light induction [22]. Adapted with permission from Ref. [22]. Copyright 2018 Springer Nature

to the plasmon substrate to obtain the reaction rate of plasmon catalytic process. By adjusting the potentials of the tip and the substrate, the chemical-reaction process caused by local heating and hot electrons can be separately studied. The linear dependence of the hot-electron effect and the exponential dependence of the thermal effect is observed and the relative contributions of these two catalytic mechanisms to the redox reaction are quantified.

6.3 Analytical Methods for Raman Spectra

Raman scattering is the inelastic scattering of photons from matter, meaning that energy exchange and a change in the direction of light occur. An energy-level diagram of Raman scattering is shown in Fig. 6.10. If the scattering frequency is lower than that of incident light, it is called Stokes Raman scattering; otherwise, it is called anti-Stokes Raman scattering. Since Raman spectra act as molecular fingerprints,

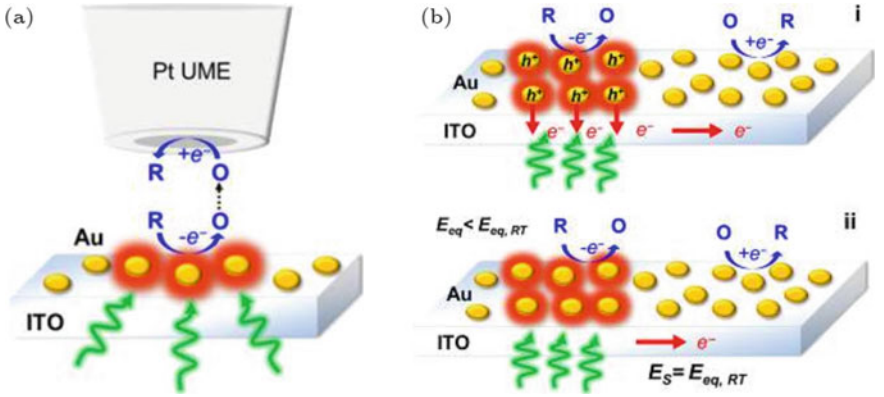

Fig. 6.9 Plasmon-driven photoelectrochemical reactions by SECM technology. **a** Schematic of the chemical-reaction measurement using SECM; **b** schematic of the catalytic mechanism of hot electrons revealed by SECM [24]. Adapted with permission from Ref. [24]. Copyright 2018 American Chemical Society

sample components can be qualitatively or quantitatively analyzed based on the peak position and intensity. Raman technology can be used to identify materials, measure temperature, analyze crystallographic orientation, etc. whereas solid materials, like single molecules, can be identified by characteristic phonon modes. The population of a phonon mode can be given by the ratio of Stokes to anti-Stokes intensities in the spontaneous Raman signal.

Raman spectra offer several advantages for analyzing the plasmonic photocatalytic reaction. The sample does not need to be fixed or sliced because it is a light-scattering technique. The signals within very small volumes can be collected from Raman spectra, and consequently, the species present in the volume can be identified. Raman spectroscopy usually does not require complicated sample preparation or even nondestructive techniques. Moreover, it is not sensitive to water-containing samples; hence, can be used to directly measure solid, liquid, and colloidal substances. Combined with a suitable gas-sample cell, it can also directly detect gas. Similar to infrared spectroscopy, Raman spectroscopy has very good specificity and selectivity, and thus, it can be used to identify some compounds with similar structures. Using Raman spectral library, we can easily identify unknown substances or confirm known ones. The high-resolution Raman system reveals many clearly defined Raman bands, which can be used to not only identify materials but also determine the sample stress.

At present, Raman spectroscopy is widely used in nondestructive testing, biosensing, and other fields. In the photocatalytic field, plasmon-driven catalytic reactions can be monitored in real-time using Raman spectroscopy to realize qualitative or quantitative analysis of the reaction's intermediate and final products. Kim et al. explored the photocatalytic reaction of 4-NBT and 4-ABT at liquid-nitrogen

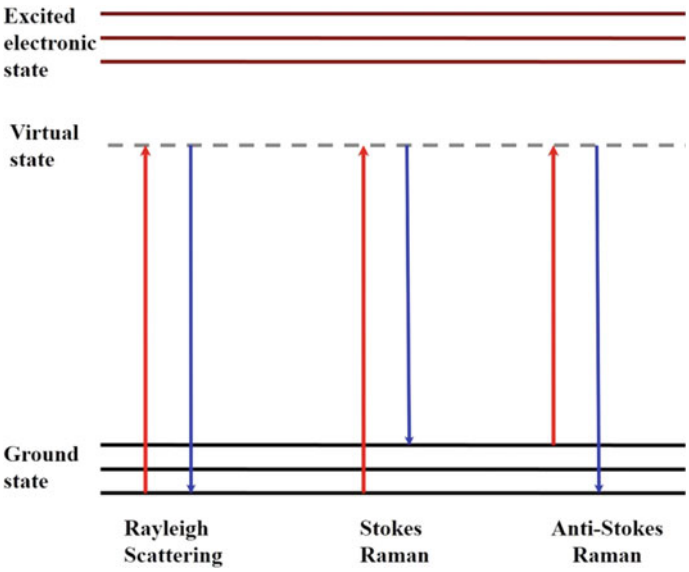

Fig. 6.10 The energy-level diagram of Raman scattering

temperature via analyses of the Raman spectra and clarified the origin of the b_2-type bands (Fig. 6.11a) [25]. Since hot electrons are generated from the plasmonic Ag nanostructure even at the liquid-nitrogen temperature, the failure of 4-NBT to achieve conversion may be due to the small spaces between ice crystals, making it difficult to break the N–O bonds. Under the same conditions, the situation of 4-ABT on Ag is the same as that of 4-NBT on Ag; thus, the b_2-type bands observed at low temperature should be due to 4-ABT rather than the formation of 4,4′-DMAB or other reaction products. In addition, hot electrons are more likely to be generated at low excitation wavelengths, and b_2-type bands appear more clearly as the excitation wavelength decreases. We conclude that both the hot electrons and the b_2-type bands of 4-ABT are related to the chemical enhancement mechanism of charge transfer. Zhang and Kneipp proposed a precise method for in situ characterization of plasmon-catalyzed reactions at a microscale resolution based on Raman spectroscopy and Raman mapping (Fig. 6.11b) [26]. The results showed that only a small portion of the AuNPs is responsible for high catalytic activity under different incubation conditions. Plasmon-induced catalytic reaction of the PNTP also showed high point-to-point change in catalytic activity during the formation of DMAB, and the characterization accuracy and repeatability of the catalytic reaction were improved by detecting many positions at microscale resolution.

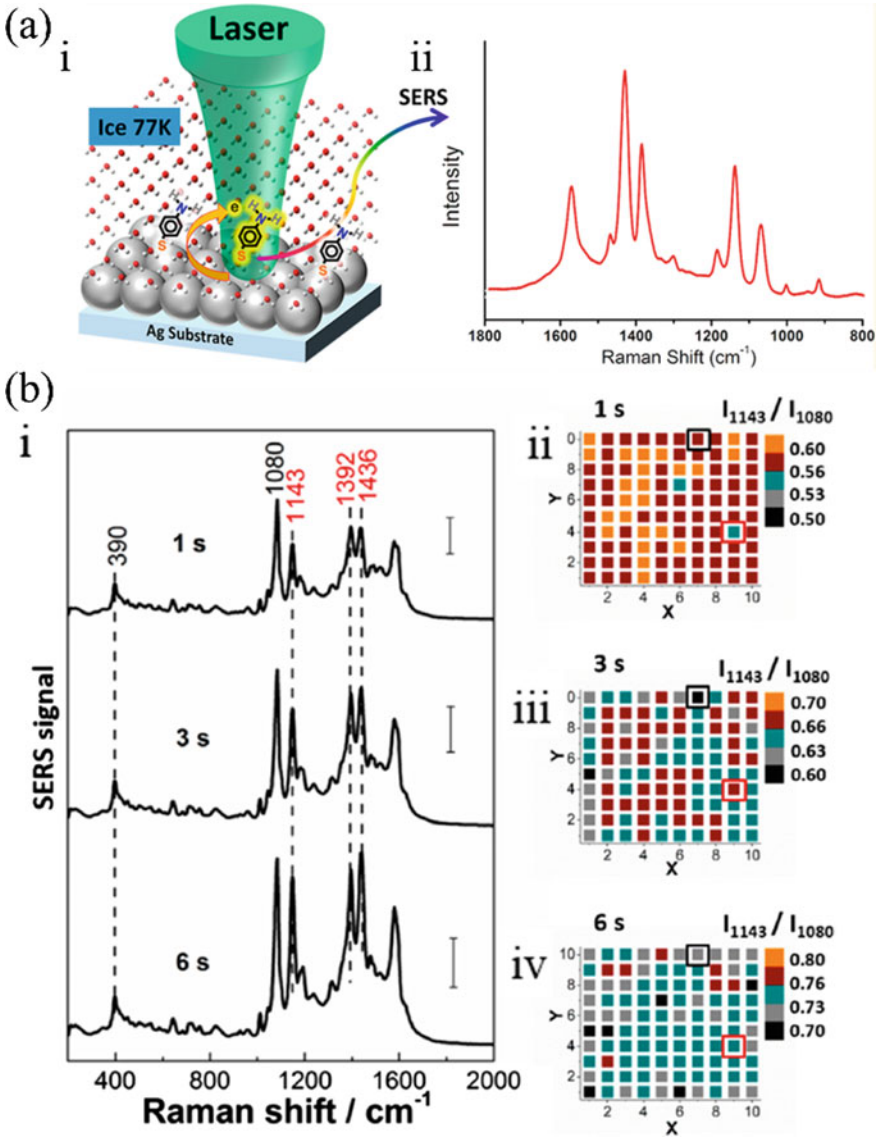

Fig. 6.11 Plasmon-induced catalytic reaction by Raman spectra analysis. **a** Schematic of the SERS spectra measurement of 4-NBT, 4-ABT, and Fe^{3+}-adsorbed cyanide on the Ag substrate at liquid temperature (i) and the SERS spectrum of 4-ABT on the Ag substrate under laser excitation at 514.5 nm (ii) [25]; **b** SERS signal of PATP on AuNPs with exposure times of 1 s, 3 s, and 6 s (i); corresponding SERS mappings of DMAB with intensity ratio I_{1143}/I_{1080} for different exposure times of 1 s, 3 s, and 6 s (ii–iv), respectively [26]. Adapted with permission from Refs. [25] and [26]. Copyright 2014 and 2018 American Chemical Society

6.4 Analytical Methods of Surface-Plasmon-Enhanced Spectra

The sensitivity of Raman spectra measurements is very poor due to the small Raman scattering cross-section, which is a great challenge for directly observing the products of the catalytic reactions. In 1977, Van Duyne et al. observed the SERS effect on the rough surface of an Ag electrode, which was a major breakthrough in Raman spectra research [27]. The enhancement of the local EM field on a metal nanostructure's surface is achieved via surface-enhanced Raman spectroscopy with the LSPR effect, thereby effectively enhancing the Raman scattering signal of molecules on the metal surface. The SERS enhancement factor is

$$\mathrm{EF} = \frac{I_{\mathrm{sers}}/N_{\mathrm{sers}}}{I_{\mathrm{nrs}}/N_{\mathrm{nrs}}}$$

where I_{sers} and I_{nrs} are the signal intensities of SERS and normal Raman spectra, respectively. N_{sers} and N_{nrs} are the numbers of molecules contributing to SERS and normal Raman spectra, respectively. SERS technology enhances the molecular signal through local field enhancement of the plasmonic metal nanostructure in hot spots, where the enhancement factor generally ranges from 10^5 to 10^{10} [28–30]. Due to the large signal enhancement, rapid signal collection can be achieved while improving the detection sensitivity, which allows the in situ detection of products in catalytic reactions.

Although SERS greatly enhances the Raman signal, conventional SERS is derived from only the average enhancement effect under the laser spot. Analyzing and studying the in situ chemical reactions of a single molecule is difficult. Therefore, overcoming the optical diffraction limit and obtaining nanoscale spatial resolution to monitor in situ plasmon-induced chemical reactions, remains a challenge for research on plasmon catalysis. TERS is a technique including a Raman spectrometer and scanning-probe microscope, capable of enhancing the Raman signal using the hot spots generated by the scanning tip of a metal. TERS not only enhances the molecules' Raman signal but also realizes Raman imaging with sub-molecular-scale spatial resolution [31]. The enhanced EM field rapidly decays along the extension direction of the tip, thus obtaining high optical resolution. HV-TERS can realize single-molecule Raman spectroscopy using a clean environment, which is ideal for exploring single-molecule plasmonic catalysis [32].

SERS and TERS are the most commonly used technologies for studying plasmon catalysis. On the one hand, surface plasmons greatly enhance the local field on the surfaces of metal nanostructures to achieve enhanced Raman scattering and improve detection sensitivity. On the other hand, the field-effect enhancement, hot electrons, and thermal effects through surface-plasmon decay can promote plasmon-induced

chemical reactions. Tian et al. first reported shell-isolated NP-enhanced Raman spectroscopy (SHINERS), whereby the Raman signals could be enhanced by $Au@SiO_2$ or $Au@Al_2O_3$ structures [33]. From experimental and theoretical SERS investigations, Sun et al. reported that molecular PATP can be selectively catalyzed to molecular DMAB with plasmonic AgNPs (Fig. 6.12) [34]. The time-dependent SERS of DMAB shows the optimal concentration of PATP and the time delay for observing strong SERS signals. In 2012, Lantman et al. researched the plasmon-induced catalytic reaction of PNTP on an Au nanoplate using AFM-TERS [35]. The hot spots formed by an Ag-coated AFM tip were used to enhance the intensity of plasmon for conversion of PNTP to DMAB. The excitation at 532 nm was found to activate a chemical reaction from PNTP to DMAB; 633 nm light was used to monitor the catalytic process during the reaction. As shown in Fig. 6.13, Sun et al. designed a self-made HV-TERS apparatus to study the plasmon-mediated in situ molecular conversion of 4NBT dimerization to DMAB, affording a new method for designing efficient HV-TERS systems and significantly extending the applications of molecular reactions [36].

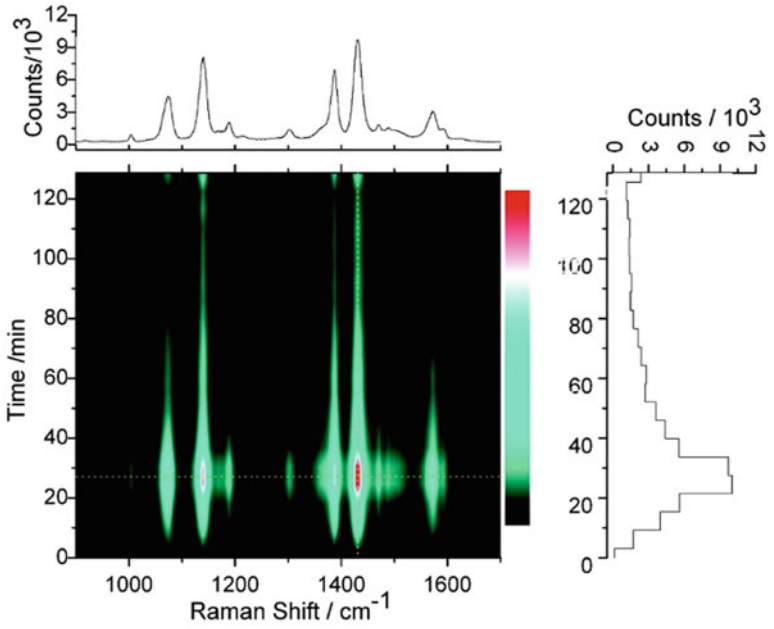

Fig. 6.12 Time-dependent SERS spectra of DMAB molecular with AgNPs [34]. Adapted with permission from Ref. [34]. Copyright 2010 American Chemical Society

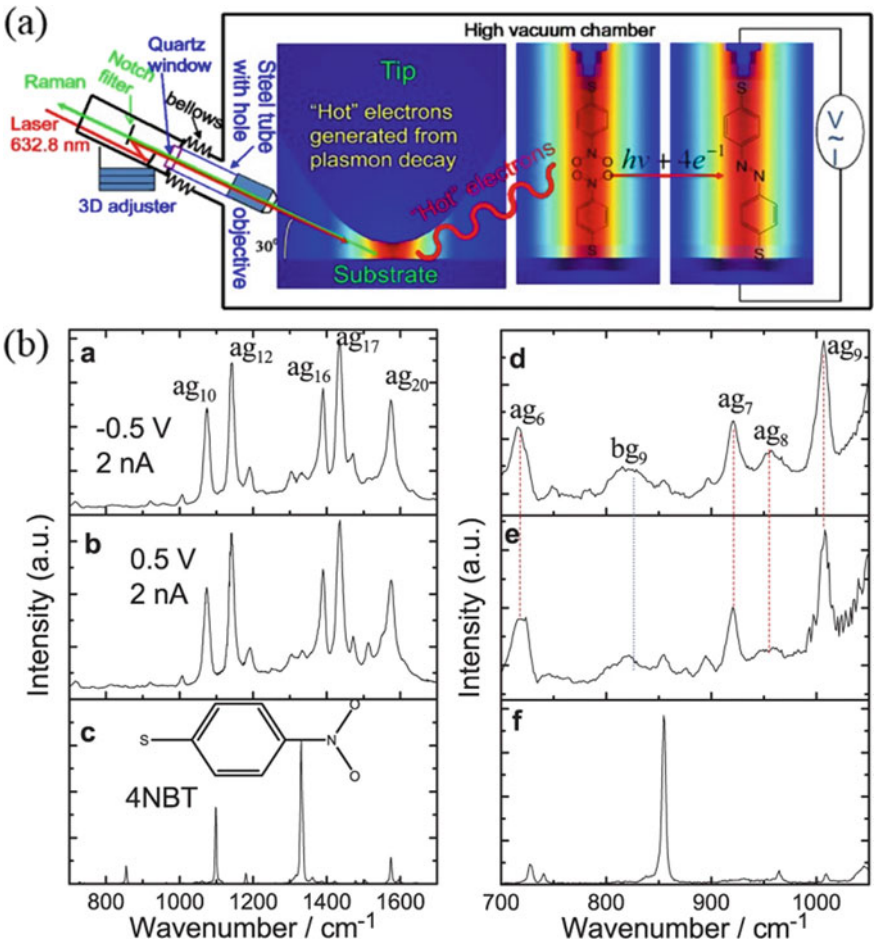

Fig. 6.13 Plasmon-induced chemical reaction measured via HV-TERS. **a** Schematics of HV-TERS. **b** Raman spectra of plasmon-induced chemical reactions by HV-TERS measurement for DMAB and 4NBT powder, and part of the corresponding amplification spectra from 700 to 1050 cm^{-1} [36]. Adapted with permission from Ref. [36]. Copyright 2012 Springer Nature

References

1. Zhang Z, Zhang C, Zheng H, Xu H (2019) Plasmon-driven catalysis on molecules and nanomaterials. Acc Chem Res 52:2506–2515
2. Brongersma ML, Halas NJ, Nordlander P (2015) Plasmon-induced hot carrier science and technology. Nat Nanotechnol 10:25–34
3. Lombardi JR, Birke RL (2008) A unified approach to surface-enhanced Raman spectroscopy. J Phys Chem C 112:5605–5617
4. Golubev AA, Khlebtsov BN, Rodriguez RD, Chen Y, Zahn DRT (2018) Plasmonic heating plays a dominant role in the plasmon-induced photocatalytic reduction of 4-nitrobenzenethiol. J Phys Chem C 122:5657–5663

5. Johnson PB, Christy RW (1972) Optical constants of noble metals. Phys Rev B 6
6. Haynes CL, van Duyne RP (2001) Nanosphere lithography: a versatile nanofabrication tool for studies of size-dependent nanoparticle optics. J Phys Chem B 105:5599–5611
7. Henzie J, Lee J, Min HL, Hasan W, Odom TW (2008) Nanofabrication of plasmonic structures. Annu Rev Phys Chem 60:147–165
8. Bigioni TP, Lin XM, Nguyen TT, Corwin EI, Witten TA, Jaeger HM (2006) Kinetically driven self assembly of highly ordered nanoparticle monolayers. Nat Mater 5:265–270
9. Mistark PA, Park S, Yalcin SE, Lee DH, Yavuzcetin O, Tuominen MT, Russell TP, Achermann M (2009) Block-copolymer-based plasmonic nanostructures. ACS Nano 3:3987–3992
10. Oh H, Pyatenko A, Lee M (2019) Laser dewetting behaviors of Ag and Au thin films on glass and Si substrates: experiments and theoretical considerations. Appl Surf Sci 475:740–747
11. Leroy F, Borowik Ł, Cheynis F, Almadori Y, Curiotto S, Trautmann M, Barb JC, Müller P (2016) How to control solid state dewetting: a short review. Surf Sci Rep 71:391–409
12. Feng P, Jiang L, Li X, Rong W, Zhang K, Cao Q (2015) Gold-film coating assisted femtosecond laser fabrication of large-area, uniform periodic surface structures. Appl Opt 54:1314–1319
13. Duchene J, Tagliabue G, Welch AJ, Cheng WH, Atwater HA (2018) Hot hole collection and photoelectrochemical CO_2 reduction with plasmonic Au/p-GaN photocathodes. Nano Lett 18:2545–2550
14. McClain MJ, Schlather AE, Ringe E, King NS, Liu L, Manjavacas A, Knight MW, Kumar I, Whitmire KH, Everitt HO, Nordlander P, Halas NJ (2015) Aluminum nanocrystals. Nano Lett 15:2751–2755
15. Chen J, Bailey CS, Hong Y, Wang L, Cai Z, Shen L, Hou B, Wang Y, Shi H, Sambur J (2019) Plasmon-resonant enhancement of photocatalysis on monolayer WSe_2. ACS Photonics 6:787–792
16. Kong T, Zhang C, Gan X, Xiao F, Li J, Fu Z, Zhang Z, Zheng H (2020) Fast transformation of a rare-earth doped luminescent sub-microcrystal via plasmonic nanoislands. J Mater Chem C 8:4338–4342
17. Samal AK, Polavarapu L, Rodal-Cedeira S, Liz-Marzan LM, Perez-Juste J, Pastoriza-Santos I (2013) Size tunable Au@Ag core-shell nanoparticles: synthesis and surface-enhanced Raman scattering properties. Langmuir 29:15076–15082
18. Xie W, Schlücker S (2015) Hot electron-induced reduction of small molecules on photorecycling metal surfaces. Nat Commun 6:7570
19. Xie W, Walkenfort B, Schlucker S (2013) Label-free SERS monitoring of chemical reactions catalyzed by small gold nanoparticles using 3D plasmonic superstructures. J Am Chem Soc 135:1657–1660
20. Zhou L, Tan Y, Wang J, Xu W, Yuan Y, Cai W, Zhu S, Zhu J (2016) 3D self-assembly of aluminium nanoparticles for plasmon-enhanced solar desalination. Nat Photonics 10:393–398
21. Zeng S, Vahidzadeh E, Vanessen CG, Kar P, Kisslinger R, Goswami A, Zhang Y, Mandi N, Riddell S, Kobryn AE, Gusarov S, Kumar P, Shankar K (2020) Optical control of selectivity of high rate CO_2 photoreduction via interband or hot electron z-scheme reaction pathways in Au-TiO_2 plasmonic photonic crystal photocatalyst. Appl Catal B-Environ 267:118644
22. Vadai M, Angell DK, Hayee F, Sytwu K, Dionne JA (2018) In-situ observation of plasmon-controlled photocatalytic dehydrogenation of individual palladium nanoparticles. Nat Commun 9:4658
23. Zhong JH, Jin X, Meng L, Wang X, Su HS, Yang ZL, Williams CT, Ren B (2017) Probing the electronic and catalytic properties of a bimetallic surface with 3 nm resolution. Nat Nanotechnol 12:132–136
24. Yu Y, Sundaresan V, Willets KA (2018) Hot carriers versus thermal effects: resolving the enhancement mechanisms for plasmon-mediated photoelectrochemical reactions. J Phys Chem C 122:5040–5048
25. Kim K, Choi J-Y, Shin KS (2014) Surface-enhanced Raman scattering of 4-nitrobenzenethiol and 4-aminobenzenethiol on silver in icy environments at liquid nitrogen temperature. J Phys Chem C 118:11397–11403

26. Zhang Z, Kneipp J (2018) Mapping the inhomogeneity in plasmonic catalysis on supported gold nanoparticles using surface-enhanced Raman scattering microspectroscopy. Anal Chem 90:9199–9205
27. Jeanmaire DL, Duyne RPV (1977) Surface Raman spectroelectrochemistry: part I. Heterocyclic, aromatic, and aliphatic amines adsorbed on the anodized silver electrode. J Electroanal Chem Interfacial Electrochem 84:1–20
28. Kleinman SL, Frontiera RR, Henry AI, Dieringer JA, Duyne RPV (2013) Creating, characterizing, and controlling chemistry with SERS hot spots. Phys Chem Chem Phys 15:21–36
29. Wang YQ, Feng F, Guo Y, Xin-Jian LI (2010) SERS detection of Rhodamine 6G by patterned silver structure immersion plated on silicon nanoporous pillar array. J Light Scattering 22:255–259
30. Cao E, Lin W, Sun M, Liang W, Song Y (2018) Exciton-plasmon coupling interactions: from principle to applications. Nanophotonics 7:145–167
31. Zhang Z, Sheng S, Wang R, Sun M (2016) Tip-enhanced Raman spectroscopy. Anal Chem 88:9328–9346
32. Verma P (2017) Tip-enhanced Raman spectroscopy: technique and recent advances. Chem Rev 117:6447–6466
33. Li JF, Huang YF, Ding Y, Yang ZL, Li SB, Zhou XS, Fan FR, Zhang W, Zhou ZY, Wu DY, Ren B, Wang ZL, Tian ZQ (2010) Shell-isolated nanoparticle-enhanced Raman spectroscopy. Nature 464:392–395
34. Fang Y, Li Y, Xu H, Sun M (2010) Ascertaining p, p′-dimercaptoazobenzene produced from p-aminothiophenol by selective catalytic coupling reaction on silver nanoparticles. Langmuir 26:7737–7746
35. Van Schrojenstein Lantman EM, Deckert-Gaudig T, Mank AJG, Deckert V, Weckhuysen BM (2012) Catalytic processes monitored at the nanoscale with tip-enhanced Raman spectroscopy. Nat Nanotechnol 7:583–586
36. Sun MT, Zhang ZL, Zheng HR, Xu HX (2012) In-situ plasmon-driven chemical reactions revealed by high vacuum tip-enhanced Raman spectroscopy. Sci Rep 2:647

Chapter 7
Plasmon-Driven Catalysis of Molecular Reactions

In plasmonic catalysis, measurement technologies and analytical methods are used to study the photocatalytic process of NH_3 decomposition, CO_2 reduction, and other gas dissociation as well as the surface catalytic reactions of typical molecular PNTP and PATP. Taking advantage of the LSPR effect of metallic NPs, understanding the mechanism of plasmon catalysis is beneficial for practical applications. In this chapter, advanced reports on gas dissociation catalytic, surface-molecular, and single-molecular catalytic reactions are introduced to better understand the development and applications of plasmon-driven catalysis.

7.1 Gas Dissociation Catalytic Reactions

Jain et al. showed that plasmonic AuNP photocatalysts can absorb visible light and perform multi-electron, multi-proton reduction on CO_2 to produce methane and ethane hydrocarbons [1]. The plasmon-catalyzed reduction reaction products were quantitatively analyzed via GC. By controlling the excitation conditions, the selective formation of reactants could be achieved. The hot electrons generated by plasmon relaxation catalyze the CO_2 reduction reactions, thereby improving the selectivity of the reaction.

Halas et al. prepared a Cu–Ru alloy NP as a plasmon catalyst and studied the NH_3-decomposition process [2]. GC–MS technology was used to characterize the apparent activation barriers under different light irradiation conditions, thus realizing the quantification of the contribution of hot electrons and thermal effects in the process of plasmon-driven chemical reactions. At the same time, it was also found that the hot electrons generated during the plasmon decay process can effectively reduce the apparent activation barrier of NH_3 decomposition, thereby catalyzing the decomposition reaction of molecules at room temperature.

© Tsinghua University Press 2022

Z. Zhang, *Plasmonic Photocatalysis*, Nanoscience and Nanotechnology,
https://doi.org/10.1007/978-981-19-5188-6_7

7.2 Surface Molecular Catalytic Reactions

PNTP and PATP molecules are often used for the plasmon catalysis of various chemical reactions. PNTP molecules can be hydrogenated to PATP molecules or undergo a coupling reaction to generate p-mercaptoazobenzene (DMAB, dimethylamineborane) under plasmon catalysis. In addition, the two molecules are firmly fixed on the surface of the metal nanostructure through the stable chemical bond formed by the sulfhydryl group and the metal. The Raman scattering spectra enhanced by surface plasmons can be obtained, and the in situ study of the plasmon catalytic mechanism can be achieved. In 2002, Kim et al. [3] observed the transformation from PNTP molecules to PATP molecules under the excitation of visible light by using SERS technology. In 2010, Huang et al. [4] reported the azo-coupling reaction of PATP molecules to DMAB molecules on Ag substrate induced by SERS (Fig. 7.1). In 2011, Dong et al. [5] studied the surface plasmon resonance induced catalytic reaction from PNTP to DMAB.

Figure 7.2a shows that Kneipp et al. [6] observed the plasmon catalytic reaction, in which PATP molecules were selectively oxidized to DMAB molecules with Ag^{+}, Au^{3+}, Pt^{4+}, and Hg^{2+} metal cations. Golubev et al. [7] used SERS to systematically study the reaction mechanism of plasmon catalysis, emphasizing the role of local temperature in plasmon catalysis. The gold nanocage cannot cause any reaction of PNTP molecules at room temperature, and it is used as a research object to distinguish the contributions of thermal effect in plasmon catalysis. As shown in Fig. 7.2b, the SERS spectra of the molecule were recorded under 633 nm laser irradiation. When the gold nanocage was uniformly heated to 55 °C, the SERS spectra of the molecule hardly changed, indicating that the PNTP molecule did not appear. With further increase in temperature, the SERS spectra changed and reflected the conversion process of PNTP molecules to PATP molecules. This result can distinguish the

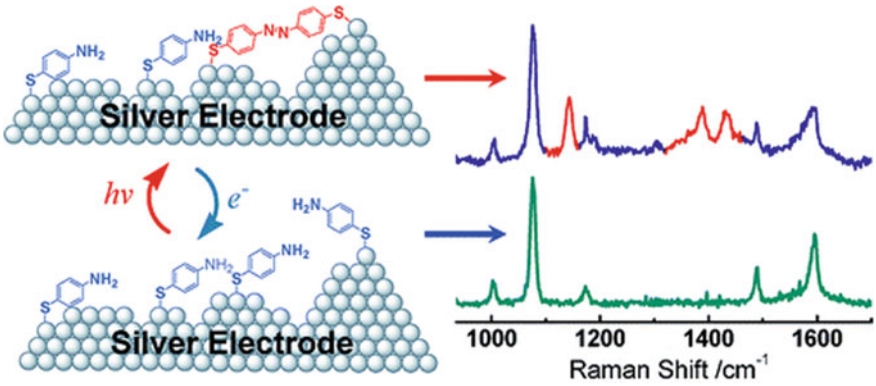

Fig. 7.1 Catalytic reaction of PATP molecules to DMAB molecules on Ag substrate and the SERS spectroscopy [4]. Adapted with permission from Ref. [4]. Copyright 2010 American Chemical Society

contribution of local thermal effects and plasmonic hot electrons for the catalytic reaction of PNTP molecules under laser irradiation. The plasmon catalytic reaction not only depends on the excitation of SPR or the transfer of hot electrons but also strongly relates to the local thermal effect caused by surface plasmons decay. Therefore, when designing and developing a new plasmon catalysis system, it is necessary to consider the role of local temperature in plasmon catalysis. In order to distinguish the plasmonic hot-electron-induced catalysis and light-induced catalysis, the molecular coupling reaction of D3ATP in air and inert gas conditions was investigated in Fig. 7.2c [8]. Sufficient photon energy and an aerobic environment were found to be indispensable in photocatalysis. For plasmonic catalysis, in either aerobic or anaerobic environments, the coupling reactions of D3ATP molecules can be observed with laser excitation at 457 nm, 532 nm, and 633 nm.

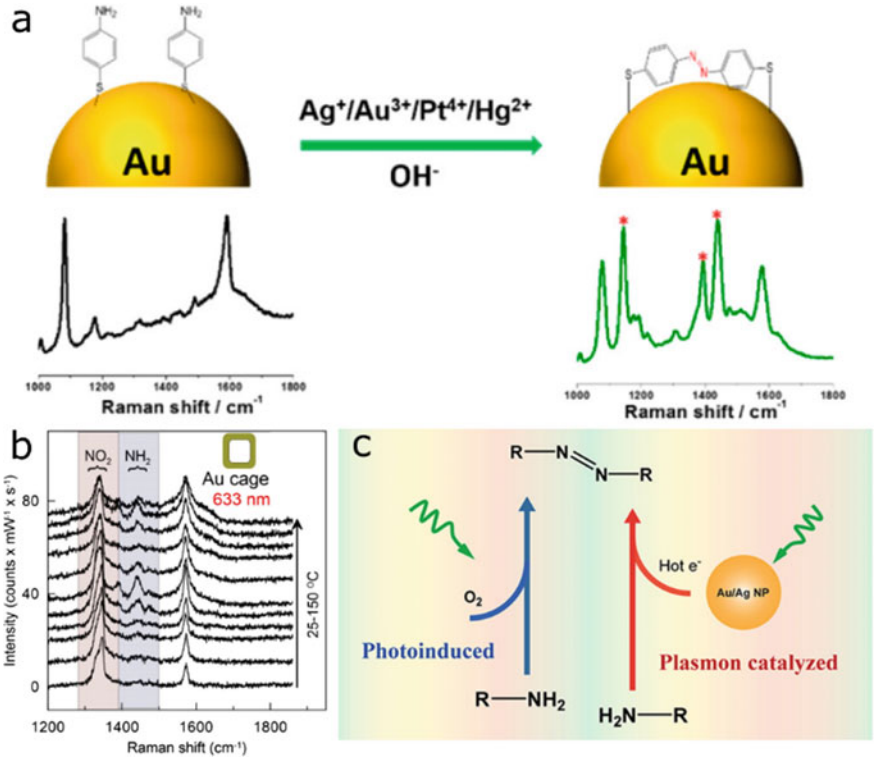

Fig. 7.2 Plasmon-induced surface molecular catalytic reaction. **a** Schematic of Ag^+, Au^{3+}, Pt^{4+} and Hg^{2+} ions promoting the polymerization of PATP molecules on Au nanoparticle and the SERS spectra of its products [6]; **b** SERS spectra of PNTP molecules on gold nanocages at elevated temperatures [7]; **c** schematic of the reaction of D3ATP molecules under both photon-induced and plasmon hot-electrons catalysis [8]. Adapted with permission from Refs. [6–8]. Copyright 2017, 2018 and 2016 American Chemical Society

In 2010, a shell-isolated nanoparticle-enhanced Raman spectroscopy (SHINERS) technology is proposed by Tian' Group, which can significantly improve the Raman enhancement [9]. The core–shell satellite structure constructed with SHINERS can simultaneously improve the effects of catalysis and signal detection in plasmon catalytic reactions and has huge development potential [10]. As shown in Fig. 7.3a, Xie et al. designed a nanostructure of silica-shell-isolated enhanced Raman spectroscopy. The nanostructure consists of large-sized AuNPs with SERS activity as the core and small-sized AuNPs with catalytic activity as satellites, which are used to start and in situ monitor the plasmon catalytic reaction [11]. The model used in this study is the hydrogenation of PNTP molecules into PATP molecules. The Raman peak of the intermediate DMAB molecule was detected when bare metal nanoparticles were used to initiate the photocatalytic reaction of PATP molecules. In the photocatalytic experiment initiated by SHINERS, PNTP molecules were directly reduced to PATP molecules, and the Raman peaks of DMAB intermediate products or other by-products were not observed, as shown in Fig. 7.3b. The photocatalysis experiments conducted using SHINERS show that it can eliminate unnecessary side reactions and provide a deeper understanding of the mechanism of plasmon-catalyzed PNTP molecular reactions.

In addition to studying model reactions, SHINERS has been used to study actual catalytic systems. Tian's research group has developed a simple and versatile satellite structure nanocatalyst based on SHINERS technology, which has good catalytic activity and Raman detection sensitivity. As shown in Fig. 7.3c, two peaks caused by Pt–C stretching vibration and linear absorption can be observed in the presence of shell isolation PtFe nanoalloy (PtFe-on-SHIN) or shell isolation Pt nanostructure (Pt-on-SHIN) catalysts, while the Raman peaks are not observed in the case of catalysts without a shell-isolated nanostructure, indicating that SHINERS technology can be used to initiate and monitor catalytic reactions. Since the Pt–C bond can be weakened by the ferrous center of the PtFe nanocatalyst, accompanied by generation of active oxygen species at room temperature, peaks at 870 cm^{-1} and 951 cm^{-1} and 1158 cm^{-1} for the PtFe-on-SHIN catalyst can be observed.

7.3 Single-Molecule Catalytic Reactions

Raman spectroscopy of the overall detection of SERS technology is widely used in the research of plasmonic catalysis, and many fruitful conclusions have been obtained. However, the collective average effect of molecular photocatalysis cannot accurately characterize the reaction of a single molecule. Detailed description in the study of single-molecule plasmon catalysis is lacking. Single-molecule SERS was first reported in two seminal articles in 1997 [13, 14] and great progress has since been made in the field [15–18]. Numerous reports exist on its use for monitoring plasmon catalysis. Figure 7.4a, b shows the two typical experimental designs of single-molecule SERS [19–22].

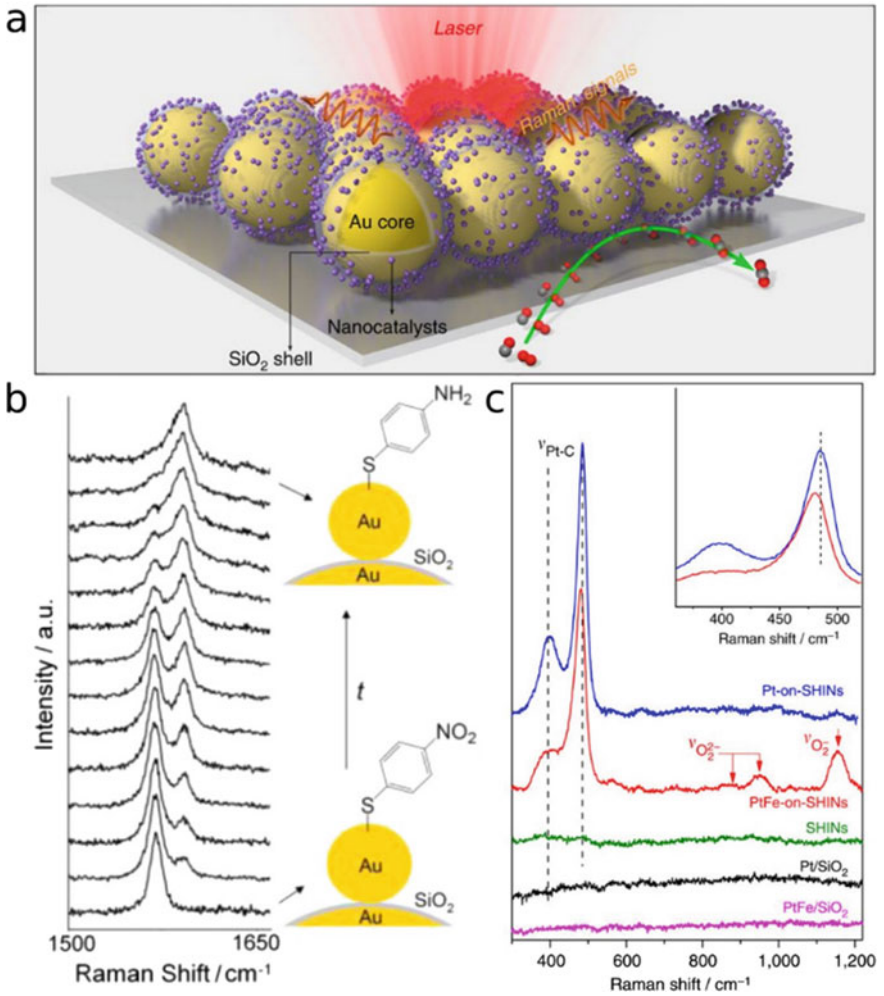

Fig. 7.3 Plasmon-induced catalytic reaction by SHINERS technology. **a** Schematic of the shell-isolated NP satellite structure with AuNPs core [12]; **b** in situ Raman spectroscopy of the PNTP to PATP catalytic reaction process monitored [11]; **c** in situ Raman spectroscopy of CO oxidation reactions on PtFe-on-SHIN and Pt-on-SHIN nanostructures monitored [12]. Adapted with permission from Refs. [11] and [12]. Copyright 2013 American Chemical Society and 2017 Springer Nature

In the hot spots generated by plasmonic NPs (such as the dimer gap), a very high enhancement factor (10^8) can be obtained, offering sufficient Raman signal enhancement for realizing single-molecule SERS detection. Related technology has been used to discover the unusual catalytic reaction process of PNTP molecules at the single-molecule level [22]. As shown in Fig. 7.4c, d, a single AuNP dimer was used for SERS detection of PNTP molecules with a concentration of 10^{-9} M. The vibration modes of PNTP molecules were observed to disappear, indicating that the

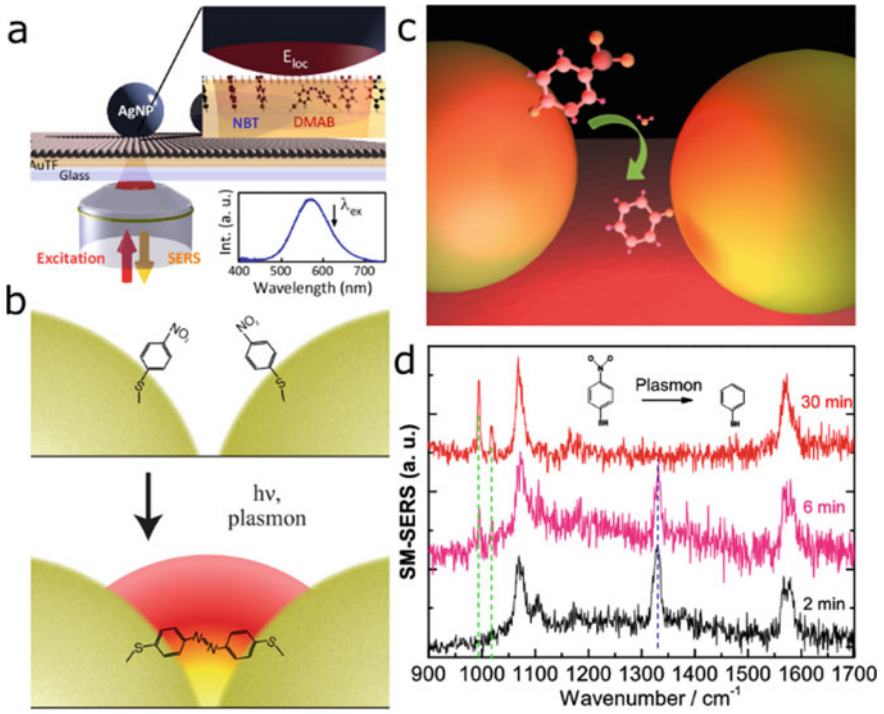

Fig. 7.4 Plasmon-induced single-molecule catalytic reaction by SERS technology. **a** Schematic of the molecular reaction of PNTP to DMAB at the single-molecule level [19]; **b** schematic of PNTP-to-DMAB molecular catalysis at the single-molecule level between two AuNPs [21]; **c** schematic of PNTP molecular decomposition at the single-molecule level; **d** time-dependent Raman spectroscopy of the PNTP molecular with plasmonic catalysis [22]. Adapted with permission from Refs. [19, 21], and [22]. Copyright 2016 American Chemical Society

nitro group was cleaved from the benzene ring during the plasmon catalysis process, leading to the formation of thiophenol. This result was obviously different from the conversion of PNTP molecules into DMAB in the case of high concentration, revealing a new phenomenon in the catalytic reaction of PNTP molecules at the single-molecule level. This study also proved the ability of single-molecule SERS to monitor single-molecule catalysis on plasmonic NPs.

TERS induces plasmon-catalyzed reactions in a similar way to SERS, which can also be used to monitor reactants in situ and in real-time. The advantage of TERS is that its nanoscale spatial resolution allows the tip to be selectively positioned on specific molecules, thereby effectively controlling the transfer of hot electrons to molecular excited states. In 2018, Kazuma et al. realized the real-time observation of plasmon-driven single-molecule dissociation reactions in space based on STM. A single dimethyl disulfide (CH_3S_2) molecule is shown as an elliptical protrusion in the STM image. After the LSP is excited, some molecules near the needle tip form two identical spherical projections, showing that CH_3S_2 breaks chemical bonds [23].

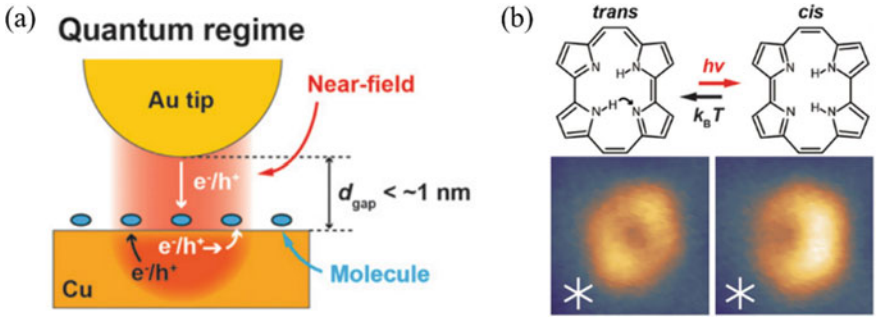

Fig. 7.5 Plasmon-induced single-molecule catalytic reaction by STM technology. **a** Schematic of the STM monitoring of the plasmon-catalyzed porphyrin molecular transformation configuration; **b** chemical structure and STM image of porphyrin molecules in trans and cis configurations [24]. Adapted with permission from Ref. [24]. Copyright 2018 American Chemical Society

In this study, a nanogap was formed between the silver tip of the STM and metal substrate. A silver tip with a radius of curvature of about 60 nm was selected to excite the SPR with a 532 nm laser to induce the dissociation reaction of CH_3S_2 molecules. Since tunneling electrons under a bias of 20 mV cannot generate vibration modes related to chemical reactions, the reaction of CH_3S_2 molecules is only related to plasmon catalysis. Based on the experimental research and theoretical calculation of STM, they proposed a catalytic mechanism of direct intramolecular excitation, that is, using SPR to induce the direct excitation of molecules from the highest occupied state to the lowest unoccupied state without the need for hot-electron transfer. As shown in Fig. 7.5, Kumagai et al. [24] also used STM to observe the tautomerism of porphyrin molecules on the Cu(111) surface. Thus, STM has become a powerful tool for studying the chemical reactions at the single-molecule level.

References

1. Yu S, Wilson AJ, Heo J, Jain PK (2018) Plasmonic control of multi-electron transfer and C-C coupling in visible-light-driven CO_2 reduction on au nanoparticles. Nano Lett 18:2189–2194
2. Sivan Y, Baraban J, Un IW, Dubi Y (2019) Comment on "quantifying hot carrier and thermal contributions in plasmonic photocatalysis". Science 364
3. Han SW, Lee I, Kim K (2002) Patterning of organic monolayers on silver via surface-induced photoreaction. Langmuir 18:182–187
4. Huang YF, Zhu HP, Liu GK, Wu DY, Ren B, Tian ZQ (2010) When the signal is not from the original molecule to be detected: chemical transformation of para-aminothiophenol on Ag during the SERS measurement. J Am Chem Soc 132:9244–9246
5. Dong B, Fang Y, Chen X, Xu H, Sun M (2011) Substrate-, wavelength-, and time-dependent plasmon-assisted surface catalysis reaction of 4-nitrobenzenethiol dimerizing to p, p′-dimercaptoazobenzene on Au, Ag, and Cu films. Langmuir 27:10677–10682
6. Zhang Z, Merk V, Hermanns A, Unger WES, Kneipp J (2017) Role of metal cations in plasmon-catalyzed oxidation: a case study of p-aminothiophenol dimerization. ACS Catal 7:7803–7809

7. Golubev AA, Khlebtsov BN, Rodriguez RD, Chen Y, Zahn DRT (2018) Plasmonic heating plays a dominant role in the plasmon-induced photocatalytic reduction of 4-nitrobenzenethiol. J Phys Chem C 122:5657–5663
8. Zhang ZL, Kinzel D, Deckert V (2016) Photo-induced or plasmon-induced reaction: investigation of the light-induced azo-coupling of amino groups. J Phys Chem C 120:20978–20983
9. Zhang YJ, Radjenovic PM, Li JF (2020) Shell-isolated nanoparticle-enhanced Raman spectroscopy towards in-situ investigating of interfacial structure. Chin J Struct Chem 39:1372–1376
10. Wang YH, Wei J, Radjenovic P, Tian ZQ, Li JF (2019) In situ analysis of surface catalytic reactions using shell-isolated nanoparticle-enhanced Raman spectroscopy. Anal Chem 91:1675–1685
11. Xie W, Walkenfort B, Schluecker S (2013) Label-free SERS monitoring of chemical reactions catalyzed by small gold nanoparticles using 3D plasmonic superstructures. J Am Chem Soc 135:1657–1660
12. Zhang H, Wang C, Sun HL, Fu G, Chen S, Zhang YJ, Chen BH, Anema JR, Yang ZL, Li JF, Tian ZQ (2017) In situ dynamic tracking of heterogeneous nanocatalytic processes by shell-isolated nanoparticle-enhanced Raman spectroscopy. Nat Commun 8:15447
13. Zou S, Wang Y, Ning S, Liu Y, Xie Z, Zhao D, Ling Y, Wang W, Zhang Z (2020) Tailoring plasmonic properties of Ag-SiO_2 nanorods and their surface-enhanced Raman scattering activities. J Phys D Appl Phys 53:404001
14. de Albuquerque CDL, Schultz ZD (2020) Super-resolution surface-enhanced Raman scattering imaging of single particles in cells. Anal Chem 92:9389–9398
15. Marshall ARL, Stokes J, Viscomi FN, Proctor JE, Gierschner J, Bouillard J-SG, Adawi AM (2017) Determining molecular orientation via single molecule SERS in a plasmonic nano-gap. Nanoscale 9:17415–17421
16. Kim NH, Hwang W, Baek K, Rohman MR, Kim J, Kim HW, Mun J, Lee SY, Yun G, Murray J, Ha JW, Rho J, Moskovits M, Kim K (2018) Smart SERS hot spots: single molecules can be positioned in a plasmonic nanojunction using host guest chemistry. J Am Chem Soc 140:4705–4711
17. de los Santos-Sanchez O (2019) Probing intensity-field correlations of single-molecule surface-enhanced Raman-scattered light. Front Phys 14:61601
18. Yuan B, Guo J, Bai S (2020) In situ thermally induced reduction of silver nitrate by polyvinyl alcohol to prepare a three-dimensional porous Ag substrate with excellent adsorption and surface-enhanced Raman scattering properties. J Mater Chem C 8:6478–6487
19. Choi HK, Park WH, Park CG, Shin HH, Lee KS, Kirn ZH (2016) Metal-catalyzed chemical reaction of single molecules directly probed by vibrational spectroscopy. J Am Chem Soc 138:4673–4684
20. Sprague-Klein E, Mcanally M, Zhdanov D, Zrimsek A, Apkarian V, Seideman T, Schatz G, van Duyne R (2018) Observation of single molecule plasmon-driven electron transfer in isotopically edited 4,4′-bipyridine gold nanosphere oligomers. Abs Pap Am Chem Soc 255
21. Brooks JL, Frontiera RR (2016) Competition between reaction and degradation pathways in plasmon-driven photochemistry. J Phys Chem C 120:20869–20876
22. Zhang Z, Deckert-Gaudig T, Singh P, Deckert V (2015) Single molecule level plasmonic catalysis-a dilution study of p-nitrothiophenol on gold dimers. Chem Commun 51:3069–3072
23. Kazuma E, Jung J, Ueba H, Trenary M, Kim Y (2018) Real-space and real-time observation of a plasmon-induced chemical reaction of a single molecule. Science 360:521–525
24. Boeckmann H, Gawinkowski S, Waluk J, Raschke MB, Wolf M, Kumagai T (2018) Near-field enhanced photochemistry of single molecules in a scanning tunneling microscope junction. Nano Lett 18:152–157

Chapter 8
Plasmon-Driven Photocatalysis of Water Decomposition and Phase Transition

With the explosive growth of the world population and the rapid development of human society and economy, the demand for fresh water is remarkably increasing. The lack of freshwater resources on earth may threaten the survival of hundreds of millions of people worldwide [1]. Water is fundamentally important for environmental protection, renewable energy, sterilization, disinfection, and so on [2]. Significant efforts have been made to find technical solutions to the water-shortage problem [3]. Solar energy has served as a low-cost renewable-energy source for providing high-quality fresh water. With the assistance of noble-metal-based plasmonics, efficient light absorption and solar-energy conversion have been extensively investigated in the photothermal field [4, 5]. In this chapter, we discuss the principles and practical applications of plasmonic photocatalytic water splitting, seawater desalination, and steam sterilization.

8.1 Water Splitting

Due to the rapid growth of global energy demand, and the limitations of natural resources such as oil, coal, and natural gas, the use of solar energy, wind power, and hydropower to create renewable energy has become a hot topic [6, 7]. Although such kinds of energy/power generation are also rapidly developing, they can only provide about one-third of the required energy growth [8]. Photocatalytic water splitting with solar energy is a promising method for clean energy production [9]. In principle, this approach using semiconductor photocatalysts only needs inexhaustible solar energy and water [10]. Both hydrogen and oxygen produced by water decomposition can be used in fuel cells to generate electricity and produce useful compounds. Further efforts have been made to improve the conversion efficiency from water to hydrogen and oxygen [11–13].

To decompose water, electrons and holes with certain reduction and oxidation potentials are indispensable (Fig. 8.1). In practical applications of photocatalytic

© Tsinghua University Press 2022

Z. Zhang, *Plasmonic Photocatalysis*, Nanoscience and Nanotechnology,
https://doi.org/10.1007/978-981-19-5188-6_8

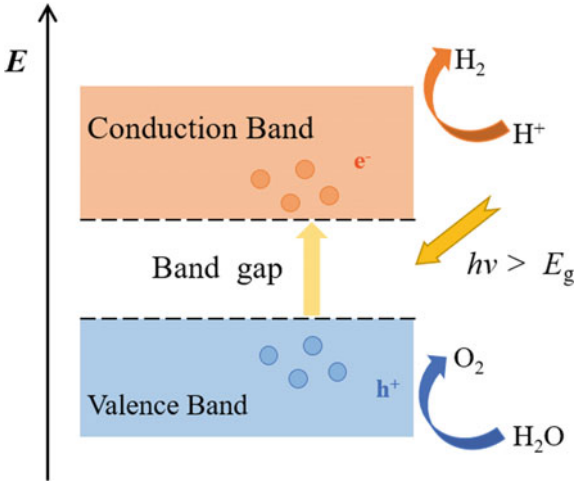

Fig. 8.1 The basic process of water splitting under semiconductor photocatalysis

water splitting, the material must be able to effectively obtain light, have the appropriate band position, quickly separate carriers, and show high stability in aqueous solution. Semiconductor oxide materials, such as TiO_2, Fe_2O_3, WO_3, and ZnO, have widely served as photocatalysts for inducing water-redox reactions. Despite their appropriate band gaps, for many semiconductors, such as WO_3 and Fe_2O_3, the band-edge positions are not suitable for overall water splitting (Fig. 8.2). Wide-bandgap semiconductors, such as TiO_2, ZrO_2, and ZnO, can generate carriers when the band gap is excited, but they are spectrally limited in UV light [14]. Moreover, the decomposition of water by carriers can be realized only when the thermodynamic conditions of carrier injection into water are favorable. Since the main process after bandgap excitation is carrier recombination, enhancing charge separation to prolong the carrier lifetime is the right way to enhance catalytic efficiency.

LSPR has also been used to improve the photocatalytic performance of semiconductors and enhance the efficiency of photocatalytic water splitting [13, 15]. As a photosensitizer, LSPR can transfer plasmon energy to adjacent semiconductors through hot-electron transfer and resonance-energy transfer [16]. Light scattering from plasmon nanostructures also contributes to enhanced photocatalysis due to extended optical pathways. Plasmon-assisted water-decomposition photocatalysts usually comprise metallic NPs and semiconductors [14]. When an n-type semiconductor is used, a Schottky junction is formed at the interface between the metal and semiconductor, resulting in enhanced charge separation and thus improving photocatalytic efficiency (Fig. 8.3a). In addition to the Schottky-junction effect, the strong light absorption of plasmons results in the formation of hot electrons and holes in the metal NPs. When the generated hot carrier is transferred from the metal to the semiconductor, it helps improve the photocatalytic efficiency (Fig. 8.3b). As the LSPR of metal NPs can be excited under visible-light irradiation, broad-bandgap semiconductors with visible-light sensitivity (such as TiO_2) can realize water decomposition under visible-light excitation. In addition to hot-electron transfer, resonance-energy

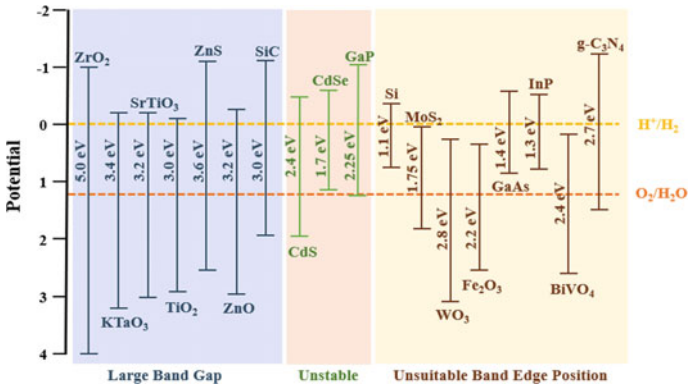

Fig. 8.2 Energy band diagram of the redox potential of a semiconductor photocatalyst relative to water splitting

transfer induced by plasmons can improve photocatalytic water-decomposition efficiency. Several nonradiative and radiative-energy transfer approaches have been proposed, the most important of which is the near-field-enhanced energy transfer. To ensure effective energy transfer, the LSPR energy of metal NPs must overlap with the bandgap energy of the semiconductors, and the valence-band electrons of semiconductors close to metal NPs are excited by the strong electric field induced by LSPR (Fig. 8.3c).

The effects of plasmon-enhanced water splitting were demonstrated with a photoanode of an Au nanostructure-ZnO nanorod array (Fig. 8.4). A kind of photoelectrode was prepared in the form of a ZnO nanorod array and modified with different quantities of gold nanospheres. Several strategies, such as hot-electron injection, EM-field generation, and heating effects, have been used to illustrate the relation between light response and the potential plasmon-induced effect. In situ X-ray absorption, spectroscopy analysis illustrates the evolution of the electronic structure with the local plasmon effect, and a theoretical simulation based on the finite-element method also illustrates the plasmon-induced effect [17].

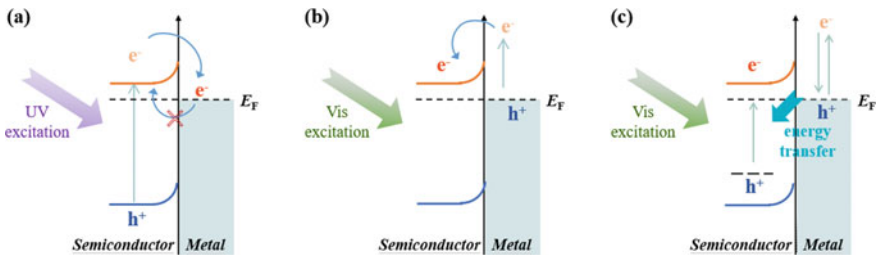

Fig. 8.3 Schematic of the semiconductor photocatalysis enhanced by LSPR. **a** Under ultraviolet excitation, **b** carrier and **c** energy transfer under visible-light excitation

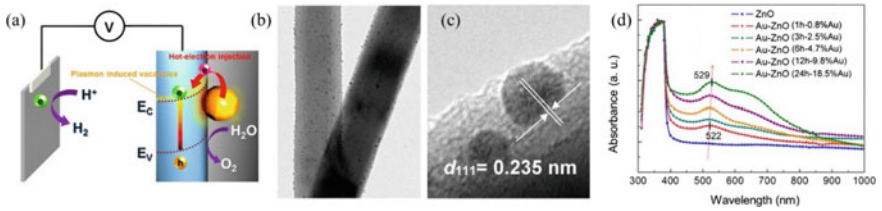

Fig. 8.4 Plasmon-induced water splitting reaction with Au–ZnO photoelectrode. **a** Schematic of plasmon-enhanced water splitting on the Au–ZnO photoelectrode; **b** TEM, **c** high-resolution TEM image, and **d** absorption spectra of Au–ZnO photoelectrodes [17]. Adapted with permission from Ref. [17]. Copyright 2012 American Chemical Society

Photocatalytic water splitting can be increased up to 66 times under visible-light irradiation with the assistance of the local plasmonic field effect [18]. The enhancement of the local field increases the formation rate of hot carriers on the surface of TiO_2, improving the efficiency of plasmonic field-effect-mediated photocatalytic reactions.

Cu-doped ZnO nanorods decorated with AuNPs have been used as an efficient semiconductor photocatalyst for water splitting under visible-light illumination [19]. Cu-doped ZnO nanorods can narrow the bandgap and change the wavelength of absorbance to red light. The absorbance of the visible region is enhanced, and the conversion of solar energy is improved. The bandgap of 3.09 eV was optimized when 3% Cu was doped into the system. Furthermore, the SPR effect produced by the decoration of 10 nm AuNPs on Cu-doped ZnO nanorods enhanced its light absorption and improved its photoelectronic chemical-water-splitting efficiency. The existence of AuNPs on the surfaces of nanorods also reduces the recombination of carriers and increases the photocurrent.

8.2 Seawater Desalination

With increased demand for fresh water, seawater desalination has attracted increased attention. Desalination and filtration of seawater or brackish water is an important channel for obtaining fresh water [20]. At present, many methods have been developed for seawater desalination and water purification [21–23]. For example, the reverse-osmosis method is based on filtration by a semi-permeable membrane to remove ions, molecules, and large particles; the electrodialysis method uses the movement of ions through an ion-exchange membrane under an applied potential difference to desalinate water; the use of input heat to evaporate water condensation, followed by purification or desalination of the thermal distillation; and the use of a hydrophobic membrane to allow water vapor to pass through and condense at low temperatures using membrane distillation. However, the use of electric energy, chemical energy, or fossil fuels for seawater desalination will negatively impact the

environment; therefore, development of a desalination system powered by renewable energy is a must.

Solar-thermal desalination can provide high-quality fresh water in the absence of a water and energy infrastructure, which is a potential low-cost and sustainable method. Water evaporation driven by solar energy is a simple and green way of producing fresh water and achieving water purification. In the past few years, the development of integrated solar-thermal-desalination systems has garnered great interest, especially solar-driven interface-evaporation ones, in which, three basic steps are followed to produce fresh watering: (I) converting solar radiation into heat (heating); (II) using the heat generated for steam production; and (III) condensing steam into water. However, evaporating a large amount of liquid using solar energy is quite low and requires complex and expensive optical concentrators.

Three crucial phases are assumed for solar-thermal desalination based on distillation: (I) conversion of light energy into heat energy; (II) generation of hot steam; and (III) conversion of steam into water by condensation. The plasmon properties of metal nanostructures not only improve the light-absorption efficiency but also increase local heating, which can be used to improve the efficiency of solar seawater desalination [24, 25]. To achieve efficient solar desalination, broadband and efficient light absorption are the key preliminary steps. Noble-metal plasmonic nanostructures have become the most widely studied materials in the field of solar-energy conversion because of their strong visible and infrared plasmonic responses and the obvious overlap of the solar spectrum [26, 27].

Halas et al. demonstrated the efficiency of admitting sunlight for generating steam using precious-metal NPs dispersed in water (Fig. 8.5) [28]. Studies have shown that 80% of the absorbed sunlight is converted into water vapor, while only 20% of the absorbed light is converted into heat in the surrounding liquid (Fig. 8.6) [28]. Research results reveal a series of new compact solar applications, such as distillation, desalination, disinfection, and sanitation in resource-poor areas. Visible light irradiates the NPs, and their surface can reach temperatures much higher than the boiling point of water under the effects of light and heat. The surface temperatures of the NPs are high, and the temperature of the surrounding liquid is low, forming a nonequilibrium state between the two. The formed vapor will wrap around the NP surfaces, and the thermal conductivity of the vapor will be lower than that of the liquid. Under continuous light, the volume of steam increases and is finally released at the liquid–gas interface. During this process, the production of steam is very strong, almost instantaneous. Under long-term light, the volume temperature of the liquid will gradually increase, eventually causing it to boil.

As a low-cost plasmon material, Al has attracted significant interest. However, the plasmon resonance frequency of Al is higher than that of gold or silver, resulting in an obvious plasmon response in the UV system. Zhu et al. have conducted significant research on solar water desalination [2], and they have prepared a wide-band and efficient Al-based plasmon absorber that effectively improves the efficiency of solar seawater desalination. They self-assembled nano Al into 3D porous films, including nano porous anodic Al oxide films, close-packed AlNPs, and a thin Al film. In this plasmon structure, Al is the only raw material, meaning low consumption and

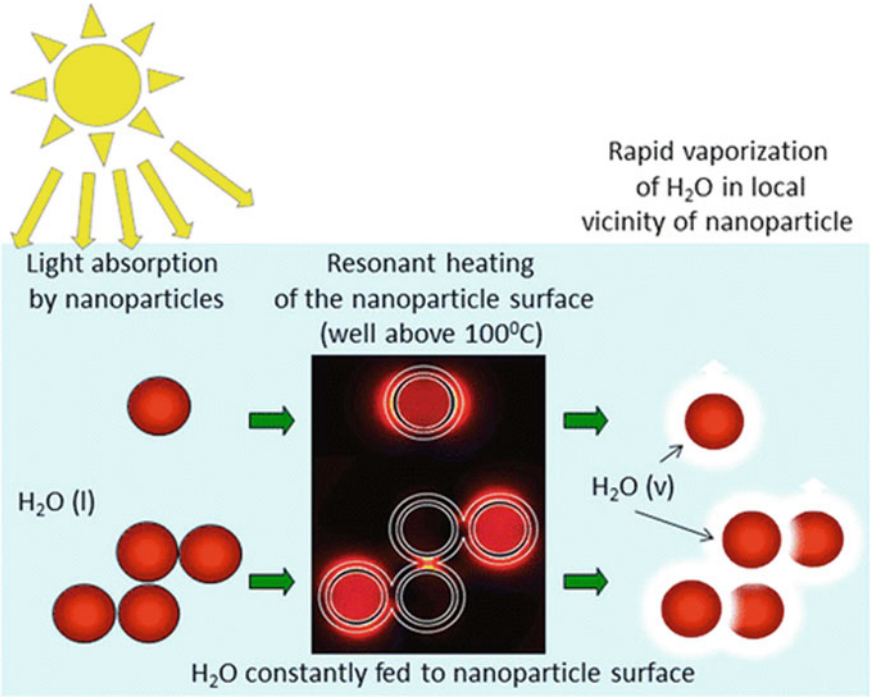

Fig. 8.5 Schematic of solar steam based on noble-metal NPs [28]. Adapted with permission from Ref. [28]. Copyright 2013 American Chemical Society

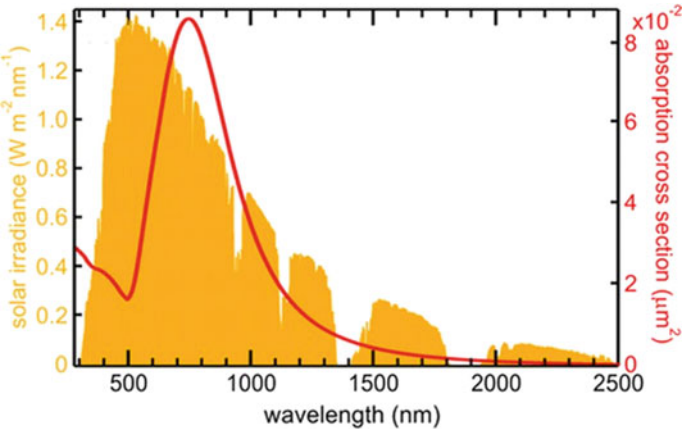

Fig. 8.6 The absorption cross-section of the gold nanoshell used to generate water vapor, which is adjusted to overlap with the solar spectral irradiance [28]. Adapted with permission from Ref. [28]. Copyright 2013 American Chemical Society

large-scale use. The Al-based plasmon solar absorber is black, making it the most effective broadband light absorber of the Al-based plasmonic nanostructures. The plasmon structure has many advantages and helps achieve efficient and effective solar desalination. It shows two physical effects essential for efficient solar desalination—namely, the mixing of local surface plasmons and nonradiative plasmon decay. LSPs can achieve high-efficiency broadband plasmon absorption. The intense nonradiative plasmon decay concentrates light on nanometer-sized volumes, resulting in local heating of the water and facilitating effective steam generation and desalination. Due to substrate porosity, the sample can float in water. AlNPs are in contact with the water surface, and a liquid–gas-phase change occurs near the air–water interface.

8.3 Steam Sterilization

Steam sterilization is widely used in public health and is the most reliable sterilization method [29]. However, traditional steam sterilization mainly relies on electricity, which is nonrenewable, not environmentally friendly, and cannot be consumed in high concentrations. In many underdeveloped countries, electricity is a scarce resource; hence, they cannot afford widespread electric sterilization. Sterilization cannot be popularized, which will provide opportunities for the outbreak of infectious diseases. Therefore, energy saving, environmental protection, and green sterilization technology with low-power consumption are urgent needs for the global population. Thus, solar-energy-based steam sterilization technology has attracted attention in recent years.

Plasmon nanostructures can effectively enhance the utilization rate of solar energy and the conversion efficiency of light energy, enhancing solar steam generation [30]. Exciting advances have been made in the nanoscale design of materials for improving light absorption, thermal management, and water supply. This technology is expected to be used for water purification, solar desalination, groundwater extraction, power generation, and other applications.

Wang et al. revealed the potential of AuNPs for solar steam sterilization [31]. Light-to-heat conversion shows great potential for the effective use of solar energy. AuNPs are an ideal photothermal-conversion material based on the surface plasmon resonance effect. AuNPs of different sizes were prepared via the seed-growth method (Figs. 8.7 and 8.8). By monitoring the temperature, vapor pressure, and mass loss of nanofluids, the effect of AuNPs on the light-to-heat conversion efficiency was studied. This study explored the influence of AuNP diameter on solar vapor light-to-heat conversion. The results show that under a xenon lamp, when the total surface area is constant, increasing the diameter can improve the light-to-heat conversion efficiency of AuNPs.

Zhu et al. revealed the dynamic advantages of interface solar steam generation over traditional sterilization technology [32]. The generation of solar steam at the interface can realize fast response, high efficiency, energy saving, and effective sterilization technology. This technology has high sterilization efficiency, with a degree

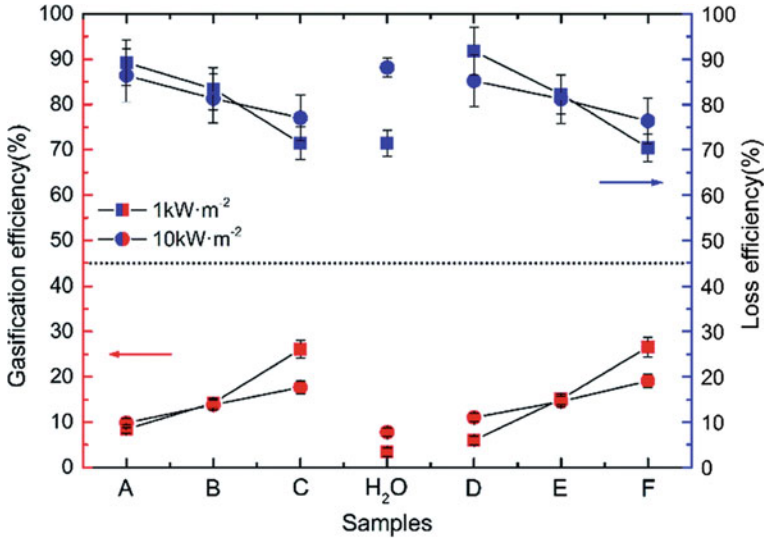

Fig. 8.7 Variation of the vaporization and loss efficiencies of pure water under changes to the AuNP diameter [31]. Adapted with permission from Ref. [32]. Copyright 2017 Royal Society of Chemistry

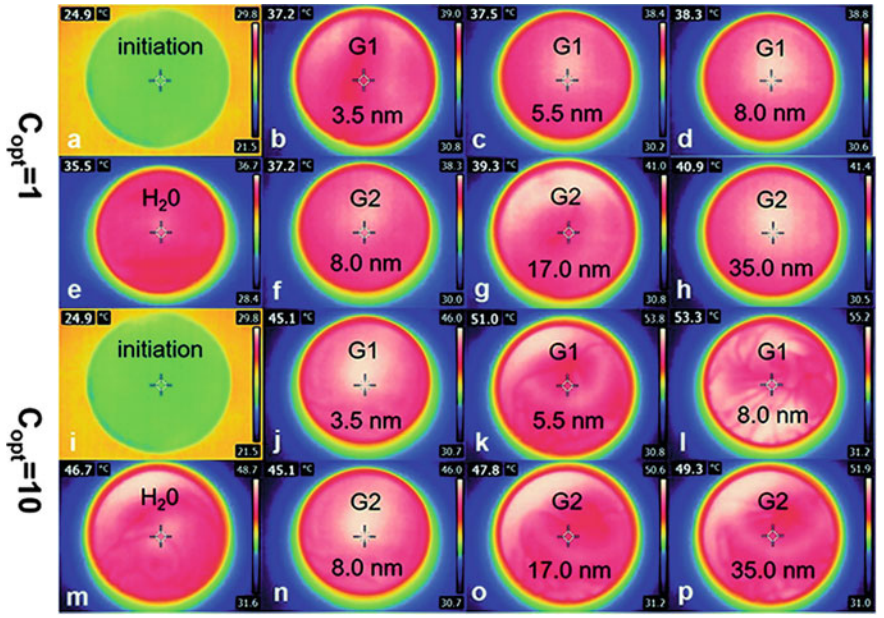

Fig. 8.8 Temperature distribution of pure water and AuNPs nanofluids with different diameters before and after sunlight irradiation [31]. Adapted with permission from Ref. [32]. Copyright 2017 Royal Society of Chemistry

exceeding the needs of the food and drug administration. Thus, solar sterilization is a promising option. Moreover, solar absorbers are made from low-cost and widely available biochar, making the entire sterilization device low-cost and widely available. Compared to solar volume heating, solar interfacial heating has many advantages for generating steam. In the heating, exposure, and cooling stages, traditional volumetric heating differs from solar-vapor dynamics based on interfacial heating. For volume heating, the entire bulk of the water is heated, while for interfacial heating, the absorbed solar energy is only concentrated at the interface of water and steam. In the heating and cooling stages, the generation of interface solar steam can achieve fast response and high-energy efficiency; in the exposure stage, the steady-state steam temperature can be increased.

References

1. Li X, Min X, Li J, Xu N, Zhu P, Zhu B, Zhu S, Zhu J (2018) Storage and recycling of interfacial solar steam enthalpy. Joule 2:2477–2484
2. Zhou L, Tan Y, Wang J, Xu W, Yuan Y, Cai W, Zhu S, Zhu J (2016) 3D self-assembly of aluminium nanoparticles for plasmon-enhanced solar desalination. Nat Photonics 10:393–398
3. Elimelech M, Phillip WA (2011) The future of seawater desalination: energy, technology, and the environment. Science 333:712–717
4. Neumann O, Urban A, Hogan N, Fang ZY, Pimpinelli A, Lal S, Nordlander P, Halas N (2013) Solar vapor generation enabled by nanoparticles. ACS Nano 246:42–49
5. Liu YM, Yu ST, Feng R, Bernard A, Liu Y, Zhang Y, Duan HZ, Shang W, Tao P, Song CY, Deng T (2015) A bioinspired, reusable, paper-based system for high-performance large-scale evaporation. Adv Mater 27:2768
6. Liu Q, Shi J, Xu Z, Zhang B, Liu H, Lin Y, Gao F, Li S, Li G (2020) InGaN nanorods decorated with au nanoparticles for enhanced water splitting based on surface plasmon resonance effects. Nanomaterials (Basel) 10
7. Guselnikova O, Trelin A, Miliutina E, Elashnikov R, Sajdl P, Postnikov P, Kolska Z, Svorcik V, Lyutakov O (2020) Plasmon-induced water splitting-through flexible hybrid 2D architecture up to hydrogen from seawater under NIR light. ACS Appl Mater Interfaces 12:28110–28119
8. Kawamura G, Matsuda A (2019) Synthesis of plasmonic photocatalysts for water splitting. Catalysts 9
9. Chen YC, Huang YS, Huang H, Su PJ, Perng TP, Chen LJ (2020) Photocatalytic enhancement of hydrogen production in water splitting under simulated solar light by band gap engineering and localized surface plasmon resonance of $Zn_xCd_{1-x}S$ nanowires decorated by Au nanoparticles. Nano Energy 67
10. Chen D, Liu Z, Guo Z, Yan W, Ruan M (2020) Decorating Cu_2O photocathode with noble-metal-free Al and NiS cocatalysts for efficient photoelectrochemical water splitting by light harvesting management and charge separation design. Chem Eng J 381
11. Zhang H, Lee JS (2019) Hybrid microwave annealing synthesizes highly crystalline nanostructures for (photo)electrocatalytic water splitting. Acc Chem Res 52:3132–3142
12. Wang M, Xu C, Li C, Jin Y (2019) Self-supporting Mof-derived CoNi@C–Au/TiO_2 nanotube array Z-scheme heterocatalysts for plasmon-enhanced high-efficiency full water splitting. J Mater Chem A 7:19704–19708
13. Zheng Z, Xie W, Huang B, Dai Y (2018) Plasmon-enhanced solar water splitting on metal-semiconductor photocatalysts. Chemistry 24:18322–18333
14. Lee JB, Choi S, Kim J, Nam YS (2017) Plasmonically-assisted nanoarchitectures for solar water splitting: obstacles and breakthroughs. Nano Today 16:61–81

15. Shi X, Ueno K, Oshikiri T, Sun Q, Sasaki K, Misawa H (2018) Enhanced water splitting under modal strong coupling conditions. Nat Nanotech 13:953–958
16. Chen YC, Hsu YK, Popescu R, Gerthsen D, Lin YG, Feldmann C (2018) Au@Nb@$H_xK_{1-x}NBO_3$ nanopeapods with near-infrared active plasmonic hot-electron injection for water splitting. Nat Commun 9:232
17. Chen HM, Chen CK, Chen CJ et al (2012) Plasmon inducing effects for enhanced photoelectrochemical water splitting: X-ray absorption approach to electronic structures. ACS Nano 6:7362–7372
18. Liu ZW, Hou WB, Pavaskar P, Aykol M, Cronin SB (2011) Plasmon resonant enhancement of photocatalytic water splitting under visible illumination. Nano Lett 11:1111–1116
19. Huynh HQ, Pham KN, Phan BT, Tran CK, Lee H, Dang VQ (2020) Enhancing visible-light-driven water splitting of ZnO nanorods by dual synergistic effects of plasmonic Au nanoparticles and Cu dopants. J Photochem Photobiol A 399:11
20. Cui R, Wei J, Du C, Sun S, Zhou C, Xue H, Yang S (2020) Engineering trace AuNPs on monodispersed carbonized organosilica microspheres drives highly efficient and low-cost solar water purification. J Mater Chem A 8:13311–13319
21. Xu N, Hu X, Xu W, Li X, Zhou L, Zhu S, Zhu J (2017) Mushrooms as efficient solar steam-generation devices. Adv Mater 29
22. Hu X, Xu W, Zhou L, Tan Y, Wang Y, Zhu S, Zhu J (2017) Tailoring graphene oxide-based aerogels for efficient solar steam generation under one sun. Adv Mater 29
23. Li X, Xu W, Tang M, Zhou L, Zhu B, Zhu S, Zhu J (2016) Graphene oxide-based efficient and scalable solar desalination under one sun with a confined 2D water path. Proc Natl Acad Sci U S A 113:13953–13958
24. Zhou L, Swearer DF, Zhang C, Robatjazi H, Zhao H, Henderson L, Dong L, Christopher P, Carter EA, Nordlander P (2018) Quantifying hot carrier and thermal contributions in plasmonic photocatalysis. Science 362:69–72
25. Brongersma ML, Halas NJ, Nordlander P (2015) Plasmon-induced hot carrier science and technology. Nat Nanotech 10:25–34
26. Chen Z, Chen M, Yan H, Zhou P, Chen X (2020) Enhanced solar thermal conversion performance of plasmonic gold dimer nanofluids. Appl Therm Eng 178
27. Wang Z, Horseman T, Straub AP, Yip NY, Li D, Elimelech M, Lin SJSA (2019) Pathways and challenges for efficient solar-thermal desalination. Sci Adv 5:eaax0763
28. Neumann O, Urban AS, Day J, Lal S, Nordlander P, Halas NJ (2013) Solar vapor generation enabled by nanoparticles. ACS Nano, 7:24-49
29. Jin X, Li Y, Li W, Zheng Y, Fan Z, Han X, Wang W, Lin T, Zhu Z (2019) Nanomaterial design for efficient solar-driven steam generation. ACS Appl Energy Mater 2:6112–6126
30. Wang X, He Y, Liu X, Shi L, Zhu J (2017) Investigation of photothermal heating enabled by plasmonic nanofluids for direct solar steam generation. Sol Energy 157:35–46
31. Guo AK, Fu Y, Wang G, Wang XB (2017) Diameter effect of gold nanoparticles on photothermal conversion for solar steam generation. RSC Adv 7:4815–4824
32. Li J, Du M, Lv G, Zhou L, Li X, Bertoluzzi L, Liu C, Zhu S, Zhu J (2018) Interfacial solar steam generation enables fast-responsive, energy-efficient, and low-cost off-grid sterilization. Adv Mater 30:e1805159

Chapter 9
Plasmon-Driven Catalysis of Nanomaterials Growth

Except for the plasmon-driven catalysis on nanoscale, molecules have been extensively studied, the LSPR effect of metal nanostructures is able to induce the micro/nanomaterials reactions. Nanomaterial growth and phase transformation can be precisely manipulated based on the dual effects of high spatial confinement and ultrashort time scale, offering a new approach to overcome the limitations of traditional methods. During the growth process, the morphologies and structural-material information are changed, while the electronic and optical properties are also changed under light irradiation. This section will focus on the growth of metal structures and polymer and crystal materials for a given mechanism: field-effect enhancement, hot electrons, or thermal effect.

9.1 Growth of Metal Structures

Noble-metal plasmonic nanostructures are regarded as a promising new class of photocatalysts for harvesting solar energy; they are essential for environmental protection [1], cancer therapy [2], and photovoltaics [3], and other fields. LSPR is based on the collective oscillations of the conduction-band electrons of noble-metal nanostructures, which can produce strong optical absorption and scattering in the subwavelength region. The plasmon-induced photocatalytic reaction is promoted by EM fields, thermal effect, and hot carriers. For example, under light irradiation, plasmonic nanostructures can enhance the polymerization, isomerization, and selective reactions due to the enhancement of the field effects on the surface of the metal nanostructure [4–8]. In addition, plasmonic thermal effect can not only accelerate reaction rates but also potentially achieve the formation of space-dependent products due to changes in nanoscale reaction rates [9–12]. Moreover, hot carriers from surface-plasmon decay are used to activate the bonding characteristics, resulting in chemical

© Tsinghua University Press 2022

Z. Zhang, *Plasmonic Photocatalysis*, Nanoscience and Nanotechnology,
https://doi.org/10.1007/978-981-19-5188-6_9

reactions, including hydrogen dissociation on metal nanostructures. Some mechanistic investigations based on noble-metal nanomaterials are expected to provide fundamental insights into the plasmon-mediated growth of metal structures.

As shown in Fig. 9.1, the growth of triangular Ag nanoprisms driven by plasmons is achieved by the field-effect enhancement, by which the rate of the redox reaction can be effectively accelerated and the growth of the metal can be realized by spatial regulation [13]. Moreover, Zhai et al. proposed the growth of plasmonic Au nanoprisms and explained the growth mechanism at the single-NP level [14]. Nanocrystal twins can significantly affect the growth kinetics by controlling the transport of hot electrons produced by surface plasmon to polyvinylpyrrolidone (PVP). PVP can both block ligands on the crystal surface and promote the accumulation of hot electrons on metal surfaces. The targeted deposition of Pt on the tips of Au nanorods (NRs) was achieved with the assistance of hot electrons (Fig. 9.2) [15]. Hot electrons act as redox agents to promote the reduction of chloroplatinic acid to Pt^0 and facilitate the epitaxial growth of Pt^0 on the tips of AuNRs. In addition, the uneven spatial distribution of the local field enables the deposition of Pt on AuNRs at specifically targeted locations, indicating the longitudinal growth of Pt. To explore the role of local fields in the transformation of plasmonic nanomaterials in photocatalytic reactions, individual Pd nanocubes adjacent to Au nanodiscs is employed as a model system, wherein the hydrogen-rich β phase can be transformed into the hydrogen-poor α phase (Fig. 9.3) [16]. The in situ and real-time plasmon-mediated phase transformation of PdNPs is achieved under optical excitation with sub-2 nm spatial resolution, where the dehydrogenation rate is improved by the strong plasmonic fields.

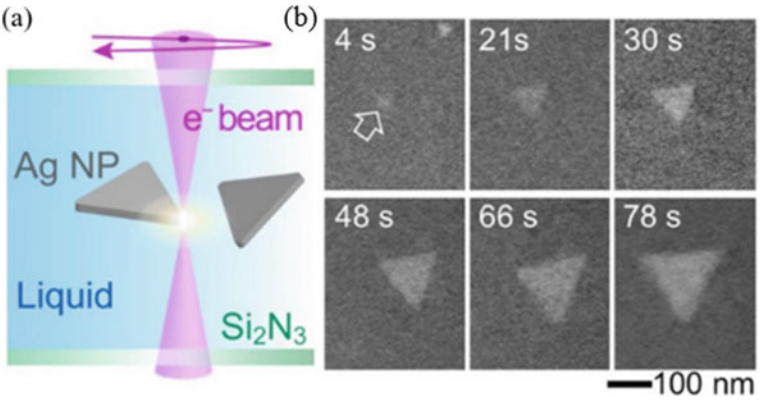

Fig. 9.1 Plasmon-driven growth of Ag nanoprisms. **a** Schematic of the growth of Ag nanoprisms driven by plasmons; **b** STEM images of AgNPs under different exposure times [13]. Adapted with permission from Ref. [13]. Copyright 2017 American Chemical Society

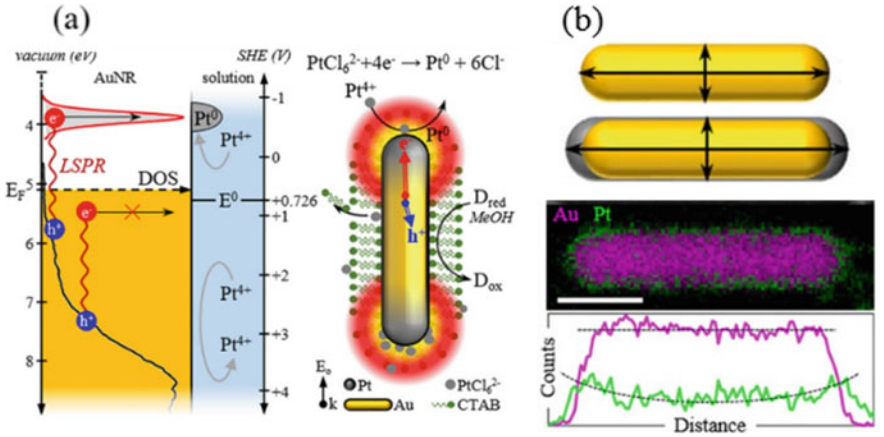

Fig. 9.2 Plasmon-driven growth of Pt on the tips of AuNRs. **a** The principle of a plasmon-driven reaction from Pt^{4+} to Pt^0 on the surface of AuNRs; **b** the schematic and elemental mapping of AuNRs coated with Pt [15]. Adapted with permission from Ref. [15]. Copyright 2018 American Chemical Society

9.2 Growth of Polymers

Plasmon-induced photocatalytic reactions caused by hot carriers, thermal effects, and local field effects have aroused great interest in applications of self-assembly [17], photodetection [18], photocatalysis [19, 20], and photovoltaic [21–23] technologies and so on. Hot carriers produced by surface-plasmon decay lead to a series of chemical reactions on the surface of metal nanostructures or semiconductors through charge transfer [24]. Plasmonic hot-electrons-mediated polymerization promotes the site-selectivity and direction of polymer growth, which depends on the precise position and polarization of metal nanostructures [25]. Except for hot-electron-driven growth of polymer, thermal effect-mediated polymerization catalytic reactions are used to develop the nanoscale features of the plasmon [26]. Also, local plasmonic field effect is another important tool for the growth of polymer [4]. The investigation of polymer growth is beneficial for the development of polymerization and nanofabrication technologies and their application to polymer optoelectronic devices.

Plasmon-induced polymer growth under low-power laser excitation with assistance from AuNPs is shown in Fig. 9.4 [25]. The growth of polymers around single-plasmonic NPs can be selectively controlled. Not only the thickness and composition of the polymer coating can be precisely controlled, but also the location and direction of the polymer growth are regulated. Such a growth of polymer is due to the generation of hot electrons from the decay of surface plasmon, which can be affected by the near-field distribution and laser polarization. This facile nanoscale polymerization growth not only offers a promising approach for fabricating multifunctional devices but also extends the applications of polymer growth at the nanoscale level.

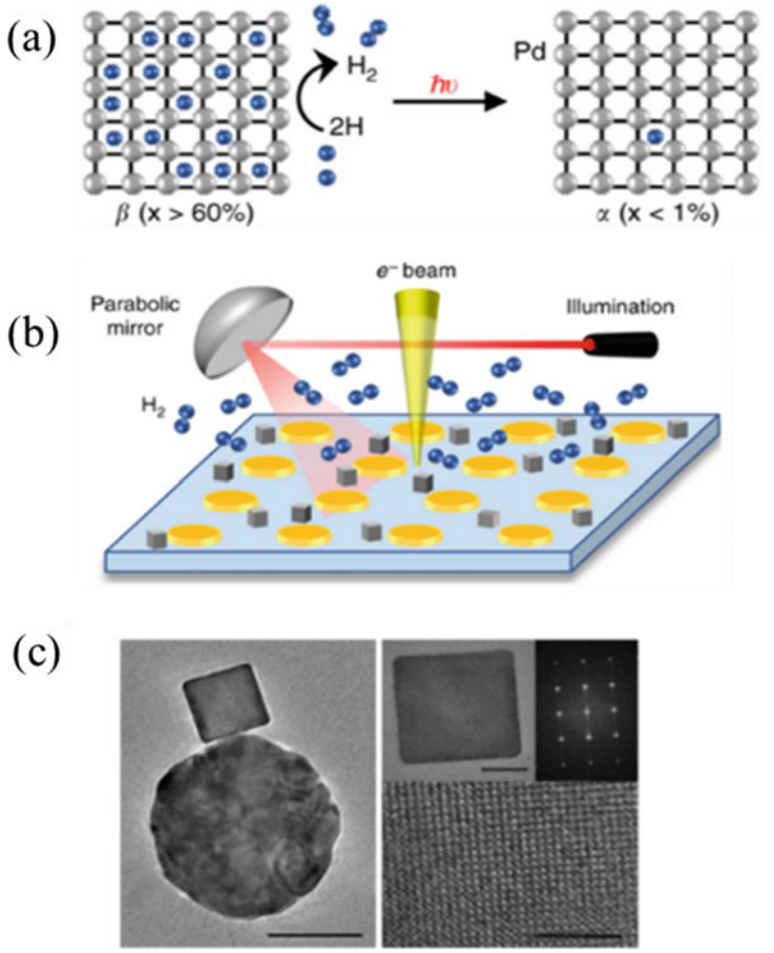

Fig. 9.3 Plasmon-driven dehydrogenation of Pd nanocube. **a** Schematic of plasmon-driven transformation of Pd nanocubes; **b** schematic of the plasmon-driven dehydrogenation experiment of Pd nanocubes; **c** TEM images of the Pd nanocube and Au nanodisc [16]. Adapted with permission from Ref. [16]. Copyright 2018 Springer Nature

Kaitlin et al. reported bulk catalysis reactions of polymers using the photothermal effect of plasmonic AuNPs [27]. As shown in Fig. 9.5, Au NPs have been shown to generate billion-fold rate enhancement of urethane polymerization under light irradiation at 532 nm. The surface temperatures of particles were sufficient to initiate the polymerization without using conventional catalysts, such as dibutyltin dilaurate. The photothermal effect of AuNPs can effectively induce bond formation between isocyanates and alcohols, and cure bulk-scale polyurethane films at unprecedented

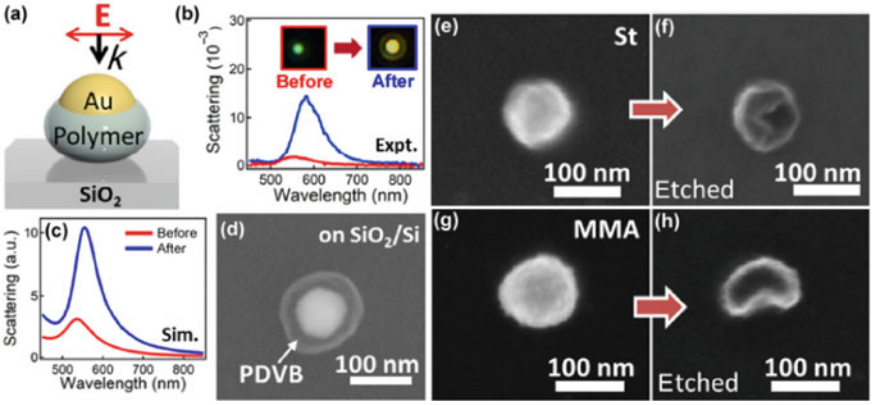

Fig. 9.4 Plasmonic hot-electron-induced growth of polymer. **a** Schematic of the plasmon-driven growth of a polymer on a SiO_2/Si wafer; **b** scattering spectra of Au nanostructures before and after laser irradiation; the inset images correspond to dark-field images; **c** the simulated scattering spectra of AuNPs; **d**–**h** SEM images of AuNPs with **d** PDVB, **e** St and **g** MMA, and **f** and **h** SEM images of etched AuNPs from (**e**) and (**g**), respectively [25]. Adapted with permission from Ref. [25]. Copyright 2018 Springer Nature

reaction rates. This work provides a new and powerful approach for increasing the rate of thermal effect-induced catalytic reactions for large-scale growth of polymer.

SU-8 is usually polymerized from a photoinitiator exposed to a specific UV wavelength excitation. Ueno et al. have exploited the field-effect enhancements of a photoresist SU-8 coating with incoherent light sources (Fig. 9.6) [4]. In their study, Au nanoblock arrays were specially customized to obtain the localized near-field and enhanced intensity. In addition, after irradiation with incoherent light sources, photoresist two-photon polymerization around the NPs was found in the high-plasmonic local field, indicating that TPA triggered a photochemical reaction in the absence of laser light sources.

9.3 Growth of Crystals

Plasmonic nanostructures can collect solar energy over the entire visible spectrum and provide effective photothermal conversion. They have been developed as a new solution to the energy crisis [28]. The enhanced EM fields around nanostructures are formed by interactions between oscillating electrons and photons under SPP excitation. The stored energy of the plasmonic local field drives the generation of hot-electron–hole pairs by Landau damping. Then, these pairs eventually transfer energy to the lattice by elastic electron–electron scattering and electron–phonon coupling, leading to a higher lattice temperature. Field-effect enhancement, hot electrons, and thermal effect are effective methods for controlling chemical reactions

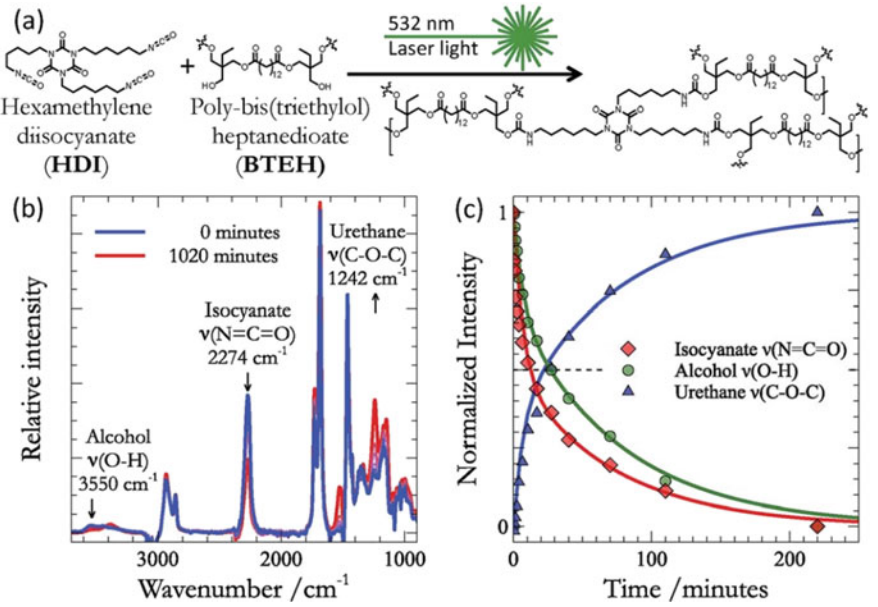

Fig. 9.5 Plasmonic thermal effect-induced growth of polymer. **a** Mechanism of polymer growth of polyurethane formation from HDI and BTEH; **b** infrared spectroscopy measurement; **c** the kinetic process for the conversion from isocyanates and alcohols to urethane [27]. Adapted with permission from Ref. [28]. Copyright 2015 Royal Society of Chemistry

catalyzed by plasmons with metal-nanostructure assistance. Unlike the catalytic reactions of molecules, surface plasmons can also promote the conversion of inorganic micro/nanomaterials, creating a new field of plasmon catalysis and demonstrating potential applications in photocatalytic fields [29].

Fujiwara et al. reported an effective way to precisely process and arrange nanomaterials at the targeted location of the plasmonic electric field (Fig. 9.7) [30]. Based on a hydrothermal synthesis reaction, ZnO nanomaterials were locally and selectively fabricated with the assistance of a plasmonic nanoantenna to reveal the role of LSPR in achieving ZnO growth with an Au nanostructure. By selectively controlling the LSPR of an Au nanoantenna, the formation of localized ZnO can be realized at the precise position of the plasmonic nanoantenna because of the nanoscale limitation of heat generation.

We have demonstrated plasmon-mediated chemical transformation from a polycrystalline nanomaterial to a single-crystalline one, where the luminescence performance is improved and the crystal structure is obviously changed (Fig. 9.8) [31]. The transformation efficiency can be precisely regulated by changing the laser wavelength, power, or density of AuNPs. In addition, with the help of self-assembled plasmonic NIs, a high-purity single crystal can be obtained, and the transformation rate can be controlled by varying the sizes and gaps of the NIs (Fig. 9.9) [32]. Such

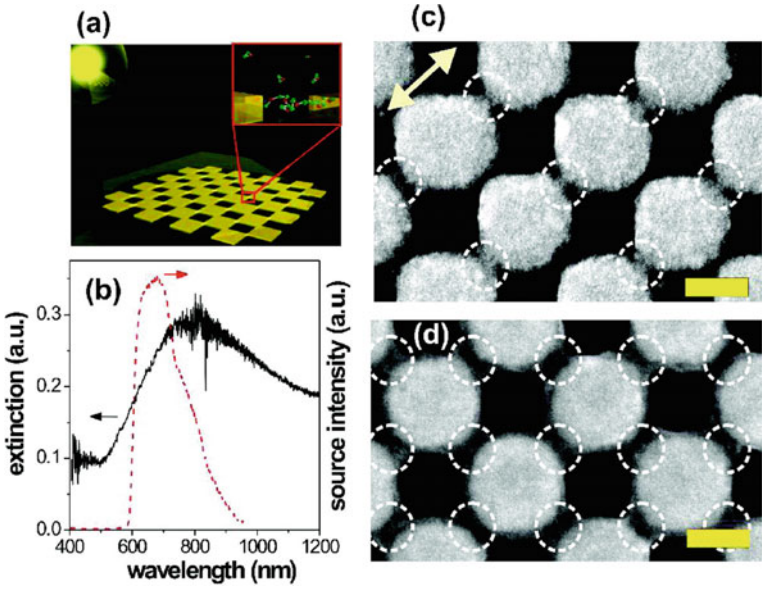

Fig. 9.6 Plasmonic field-effect enhancement induced growth of polymer. **a** Schematic of the checkerboard pattern of Au nanoblocks coated with SU-8; the inset illustrates the polymerization of the SU-8 present in the nanogap; **b** extinction spectra of the checkerboard pattern and the incoherent light source; **c** SEM image of the structure exposure by a polarized source along the direction of the arrow; **d** SEM image of the structure exposure by the unpolarized source [4]. Adapted with permission from Ref. [27]. Copyright 2008 American Chemical Society

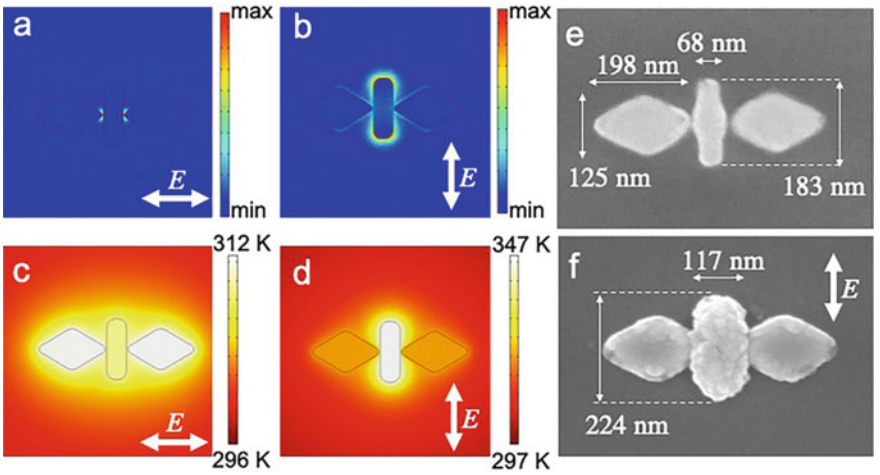

Fig. 9.7 Plasmon-driven growth of a ZnO nanobutterfly structure. **a** and **b** The calculated localized field and **c** and **d** temperature distributions of the structure under different incident-light-polarization directions; **e** and **f** SEM images of the structure before and after laser irradiation, respectively [30]. Adapted with permission from Ref. [31]. Copyright 2020 American Chemical Society

a plasmon-driven crystalline transformation is achieved even at very low temperatures, which is impossible using traditional methods. This simple and universal approach to plasmon-driven crystal transformation shows powerful aspects of the thermal and catalytic effects, resulting in a simple and fast in situ method for realizing single-crystal products. This study can solve the bottleneck problem of traditional methods and expand the applications of surface plasmons to a wider range of fields. Furthermore, the relative contributions of thermal effects and hot electrons in plasmon-mediated crystal transformation were investigated [33]. The transformation rate and corresponding product significantly differed in the presence of hot electrons. Hot electrons primarily promote the oxidation reaction and generate reactive oxygen species that participate in the crystal transformation. Therefore, thermal effect plays an important role in the plasmon-mediated crystal transformation with synergistic effects of hot electrons. This research offers an understanding of the special role of hot electrons and thermal effects in plasmon catalysis, which is essential for the utilization of highly localized thermal effects and the design of energy-saving plasmonic photocatalysts.

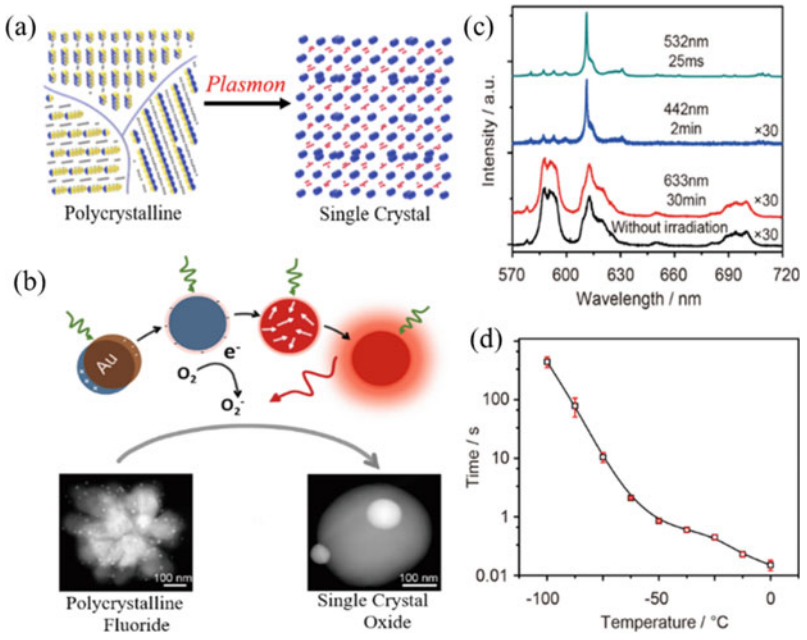

Fig. 9.8 Plasmon-driven growth of polycrystalline to a single crystal with AuNPs. **a** Schematic of plasmon-mediated crystal transformation from polycrystalline to a single crystal; **b** the schematic of principles for crystal transformation, and STEM images of polycrystalline reactant and single-crystal product; **c** wavelength-dependent crystal transformation; **d** the time of crystal transformation at low temperatures [31]. Adapted with permission from Ref. [32]. Copyright 2019 John Wiley and Sons

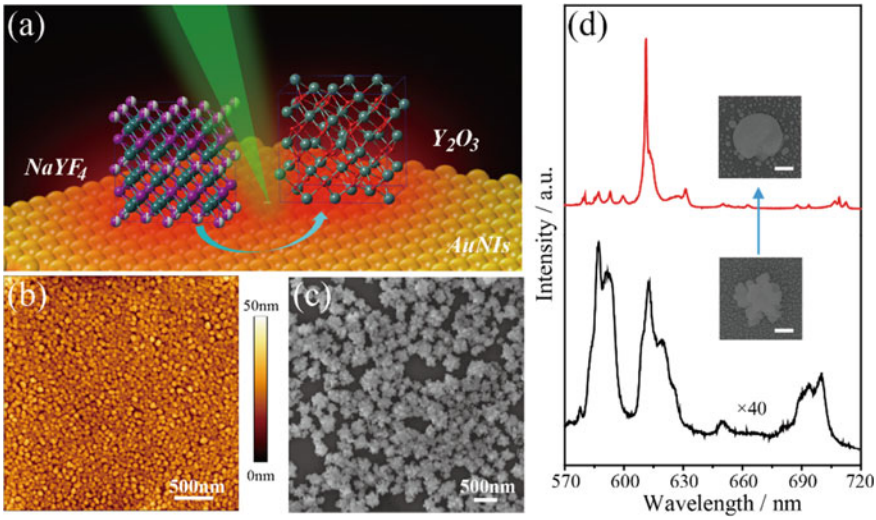

Fig. 9.9 Plasmon-driven growth of polycrystalline to a single crystal with AuNIs. **a** Schematic of plasmon-mediated crystal transformation with the assistance of plasmonic AuNIs; **b** AFM image of the AuNIs; **c** SEM image of $NaYF_4$ sub-microcrystal; **d** in-situ luminescence spectra of sub-microcrystal before and after laser irradiation, and insert shows the SEM images of reactant and product, respectively [32]. Adapted with permission from Ref. [33]. Copyright 2020 Royal Society of Chemistry

References

1. Zhou L, Tan Y, Wang J, Xu W, Yuan Y, Cai W, Zhu S, Zhu J (2016) 3D self-assembly of aluminium nanoparticles for plasmon-enhanced solar desalination. Nat Photonics 10:393–398
2. Liu K, Liu K, Liu J, Ren Q, Zhao Z, Wu X, Li D, Yuan F, Ye K, Li B (2020) Copper chalcogenide materials as photothermal agents for cancer treatment. Nanoscale 12:2902–2913
3. Wang S, Ding T (2019) Photothermal-assisted optical stretching of gold nanoparticles. ACS Nano 13:32–37
4. Ueno K, Juodkazis S, Shibuya T, Yokota Y, Mizeikis V, Sasaki K, Misawa H (2008) Nanoparticle plasmon-assisted two-photon polymerization induced by incoherent excitation source. J Am Chem Soc 130:6928–6929
5. Hubert C, Rumyantseva A, Lerondel G, Grand J, Kostcheev S, Billot L, Vial A, Bachelot R, Royer P, Chang SH, Gray SK, Wiederrecht GP, Schatz GC (2005) Near-field photochemical imaging of noble metal nanostructures. Nano Lett 5:615–619
6. Volpe G, Noack M, Acimovic SS, Reinhardt C, Quidant R (2012) Near-field mapping of plasmonic antennas by multiphoton absorption in poly(methyl methacrylate). Nano Lett 12:4864–4868
7. Ho C-S, Garcia-Etxarri A, Zhao Y, Dionne J (2017) Enhancing enantioselective absorption using dielectric nanospheres. ACS Photonics 4:197–203
8. Zhao Y, Saleh AAE, Dionne JA (2016) Enantioselective optical trapping of chiral nanoparticles with plasmonic tweezers. ACS Photonics 3:304–309
9. Cao L, Barsic DN, Guichard AR, Brongersma ML (2007) Plasmon-assisted local temperature control to pattern individual semiconductor nanowires and carbon nanotubes. Nano Lett 7:3523–3527

10. Halas NJ, Neumann O, Urban A, Hogan N, Fang Z, Pimpinelli A, Lal S, Nordlander P (2013) Solar vapor generation enabled by nanoparticles. Abs Pap Am Chem Soc 246
11. Hung WH, Aykol M, Valley D, Hou W, Cronin SB (2010) Plasmon resonant enhancement of carbon monoxide catalysis. Nano Lett 10:1314–1318
12. Adleman JR, Boyd DA, Goodwin DG, Psaltis D (2009) Heterogenous catalysis mediated by plasmon heating. Nano Lett 9:4417–4423
13. Sutter P, Li Y, Argyropoulos C, Sutter E (2017) In situ electron microscopy of plasmon-mediated nanocrystal synthesis. J Am Chem Soc 139:6771–6776
14. Zhai Y, Duchene JS, Wang YC, Qiu J, Johnston-Peck AC, You B, Guo W, Diciaccio B, Qian K, Zhao EW, Ooi F, Hu D, Su D, Stach EA, Zhu Z, Wei WD (2016) Polyvinylpyrrolidone-induced anisotropic growth of gold nanoprisms in plasmon-driven synthesis. Nat Mater 15:889–895
15. Forcherio GT, Baker DR, Boltersdorf J, Leff AC, McClure JP, Grew KN, Lundgren CA (2018) Targeted deposition of platinum onto gold nanorods by plasmonic hot electrons. J Phys Chem C 122:28901–28909
16. Vadai M, Angell DK, Hayee F, Sytwu K, Dionne JA (2018) In-situ observation of plasmon-controlled photocatalytic dehydrogenation of individual palladium nanoparticles. Nat Commun 9:4658
17. Cortes E, Xie W, Cambiasso J, Jermyn AS, Sundararaman R, Narang P, Schlueker S, Maier SA (2017) Plasmonic hot electron transport drives nano-localized chemistry. Nat Commun 8:14880
18. Knight MW, Sobhani H, Nordlander P, Halas NJ (2011) Photodetection with active optical antennas. Science 332:702–704
19. Kim M, Lin M, Son J, Xu H, Nam J-M (2017) Hot-electron-mediated photochemical reactions: principles, recent advances, and challenges. Adv Opt Mater 5
20. Sun M, Xu H (2012) A novel application of plasmonics: plasmon-driven surface-catalyzed reactions. Small 8:2777–2786
21. Clavero C (2014) Plasmon-induced hot-electron generation at nanoparticle/metal-oxide interfaces for photovoltaic and photocatalytic devices. Nat Photonics 8:95–103
22. Mukherjee S, Libisch F, Large N, Neumann O, Brown LV, Cheng J, Lassiter JB, Carter EA, Nordlander P, Halas NJ (2013) Hot electrons do the impossible: plasmon-induced dissociation of H_2 on Au. Nano Lett 13:240–247
23. Christopher P, Xin H, Marimuthu A, Linic S (2012) Singular characteristics and unique chemical bond activation mechanisms of photocatalytic reactions on plasmonic nanostructures. Nat Mater 11:1044–1050
24. Brongersma ML, Halas NJ, Nordlander P (2015) Plasmon-induced hot carrier science and technology. Nat Nanotechnol 10:25–34
25. Wang Y, Wang S, Zhang S, Scherman OA, Baumberg JJ, Ding T, Xu H (2018) Plasmon-directed polymerization: regulating polymer growth with light. Nano Res 11:6384–6390
26. Walker JM, Gou LF, Bhattacharyya S, Lindahl SE, Zaleski JM (2011) Photothermal plasmonic triggering of Au nanoparticle surface radical polymerization. Chem Mater 23:5275–5281
27. Haas KM, Lear BJ (2015) Billion-fold rate enhancement of urethane polymerization via the photothermal effect of plasmonic gold nanoparticles. Chem Sci 6:6462–6467
28. Gao C (2016) Controlled synthesis of plasmonic noble metal nanoparticles. Abs Pap Am Chem Soc 252
29. Caglayan H, Bulu I, Ozbay E (2008) Focusing surface plasmons via changing the incident angle. J Appl Phys 103:053105
30. Fujiwara H, Suzuki T, Pin C, Sasaki K (2020) Localized ZnO growth on a gold nanoantenna by plasmon-assisted hydrothermal synthesis. Nano Lett 20:389–394

31. Zhang C, Lu J, Jin N, Dong L, Fu Z, Zhang Z, Zheng H (2019) Plasmon-driven rapid in situ formation of luminescence single crystal nanoparticle. Small 15:e1901286
32. Kong T, Zhang C, Gan X, Xiao F, Li J, Fu Z, Zhang Z, Zheng H (2020) Fast transformation of a rare-earth doped luminescent sub-microcrystal via plasmonic nanoislands. J Mater Chem C 8:4338–4342
33. Zhang C, Kong T, Fu Z, Zhang Z, Zheng H (2020) Hot electron and thermal effects in plasmonic catalysis of nanocrystal transformation. Nanoscale 12:8768–8774